ELECTRONICS

Editorial

TO readers of this issue of the "Electronics" journal with pleasure I can suggest to pay attention to three invited papers: "Practical Implications of Low Voltage Ride Through Requirements on Windturbine Power Conversion", author D. Raca, "Model Based Design of an Efficient CORDIC Algorithm Implementation", authors V. Zerbe and M. Backhaus, and "CAE Application and Certification for Industrial and Educational Customers: The Case of University-Industry Cooperation between EPLAN and RFH", author D. Lukač.

Ph.D. Dejan Raca describes in his paper the practical challenges and implications of low-voltage ride through (LVRT) requirements on design of windturbine (WT) power conversion system. Integration into power grids depends on electric power conversion topology.

Prof. Volker Zerbe and Michael Backhaus describe the model-based design concept of the compass design. Different hardware solutions of the CORDIC algorithm are analyzed. The model was stepwise refined and implemented on FPGA chip using Quartus II software.

Duško Lukač, in his paper presents examples of the application of the currently most used CAE software for electrical engineering and project planning EPLAN Electric P8. This paper has provided the applicational and conceptual insights in the most used CAE software for electrical engineering and project planning in the European industry, motives, conceptualization and design of the successful university-industry cooperation in the area of the Third-Party Certification by using the open source LMS application.

In the paper "An Analytical Model of Inversion Layer Quantization and Gate Oxide Quantum Mechanical Tunneling in Nano-p-MOSFETs" by A. Chaudhry and J. N. Roy is developed and described an analytical model of energy quantization parameters for n-MOSFET and p-MOSFET. Based on these derived parameters, the inversion charge capacitance and the total gate capacitance, including the quantum mechanical effects, have been obtained.

Remaining papers are presented on the 9th Scientific-Professional Symposium INFOTEH®-JAHORINA 2010 that was held on 17-19 March 2010. On the Symposium it was presented 218 regular papers and 20 student works. There were over 300 registered Symposium participants. The papers for this issue of the "Electronics" journal were selected by Chairman of the Symposium, Professor emeritus Slobodan Milojković.

Ph.D. Branko Dokić, full professor
Editor-in-Chief

Practical Implications of Low Voltage Ride Through Requirements on Windturbine Power Conversion

Dejan Raca

Abstract—**Practical challenges and implications of low voltage ride through (LVRT) requirements on design of windturbine (WT) power conversion system are discussed in this paper. Main focus and main challenges lie in retrofitting existing turbines that are not LVRT compliant and in designing new doubly fed systems bearing LVRT in mind. This is contrasted to full conversion (FC) which is best suited for this application. Certification process is briefly reviewed for completeness.**

Index Terms—**Low voltage ride through (LVRT), wind energy converter (WEC), windturbine (WT), power converter, certification.**

I. INTRODUCTION

THE ratio between renewable energy sources to conventional sources is steadily increasing in many electric energy systems. This leads to introduction of more stringent rules to connection of these facilities to the grid. Wind energy conversion is the most mature and the most widespread of renewable technologies at the moment, and therefore receives the most attention from regulatory bodies as well as from the manufacturers and end users. In order to integrate wind farms into the grid, they are requested to follow directives from a dispatch center and participate in frequency control rather than to produce as much power as dictated by available wind [1]. Reactive power and voltage control requirements are also becoming more stringent, as well as fault tolerance requirements like low voltage ride through (LVRT).

All grid code requirements are defined for point of connection to the grid and in some cases can be satisfied with additional equipment like static compensators. A more economic approach is sought through making individual WTs dispatchable within a wind farm. Steady tightening of LVRT requirements makes wind farm level solutions absolutely impractical and must be handled on an individual-WT basis. Interdependency between power conversion technology and LVRT requirements is the most pronounced and that is why it is selected as a focal point of this paper.

Nowadays, power rating of individual WT is ranging 2MW up to 6MW. At these power rating and with tendency to increase effectiveness and efficiency, all recent developments are based on variable speed technology. It is well known that wind energy curve for a given blade design depends on the third power of wind speed and a power coefficient which is dependent on blade tip speed and wind speed ratio [2]. Resulting wind power curve is highly nonlinear with four distinct regions for variable speed design. The first region is below cut-in speed when WT is out of production. The second region is operation with constant pitch angle which corresponds to optimal rotor efficiency. The third region is nominal power region, and the last one is excessive winds speed region where WT has to be taken off line. Constant speed turbines can efficiently exploit wind only at the corner point between regions two and three. In all other operating points rotor efficiency is significantly deteriorated if at all possible. This is why additional complexity related to variable speed and variable pitch designs is widely accepted. All the key auxiliary systems, like pitch, have also to be considered when designing an LVRT compliant WT, but in this paper main focus will remain on core power conversion.

An overview of available WT power conversion topologies is given in section II and it includes constant speed turbines whose retrofitting to fulfill LVRT requirements is mandated by some grid codes, like Spanish P.O. 12.3 [3]. General requirements for LVRT and certification procedures are briefly discussed in sections III and IV respectively. Section V is dedicated to a description of retrofitting solutions, while section VI discusses challenges related to new designs of DFIG systems for LVRT compliant design. Section VII briefly reviews advantages of full conversion systems with respect to LVRT.

II. POWER CONVERSION TECHNOLOGY FOR WTs

The purpose of this section is to review the available power conversion technologies without a tendency to follow any established classification. Differentiation between constant and variable speed topologies is based on the most usual combinations and does not mean that different combinations are not possible.

A. Nearly Constant Speed WECs

Constant speed turbines are also known as stall turbines as they exploit aerodynamic effect called stall. Stall automatically sets in because shaft speed is constant and thus limits turbine aerodynamic efficiency at high wind speeds. This means that fixed blades can be used for rotor construction. Combined with directly connected squirrel cage induction generators (SCIG) this comprises the most inexpensive WT technology, Fig. 1.

SCIG technology typically includes a soft starter to limit connection transients and is bypassed during steady state operation. Power factor is maintained using banks of shunt capacitors. Limitation of the single wind-speed operation can be mitigated using double speed generators.

Stall-controlled turbines alone are not limited to operate at only one speed. If paired with wound rotor induction generator (WRIG) and variable rotor resistance control (RCC – rotor current control) these turbines can be utilized over a speed range of approximately 10%, Fig. 2. Rotor resistance adjustments correspond to slip variations of 0.6 – 10%. These turbines would still come equipped with soft starters and switched shunt capacitors. RCC is typically implemented as rotating equipment.

B. Variable Speed WECs

The enabling technology for variable speed WTs is a electro-mechanical drive-train which enables connection to fixed frequency grid. As stated above, even stall turbines can operate in wide speed range. The main difference is that variable pitch turbines extend speed range for nominal power operation (the third range) from a single point to a range of speeds.

Configuration of electro-mechanical drive-train in Fig. 3 is based on doubly-fed induction generator (DFIG). WRIG used in this application are equipped with slip-rings. DFIG configuration is considered relatively inexpensive due to a lower, typically 1/3, rating of frequency converter to the rating
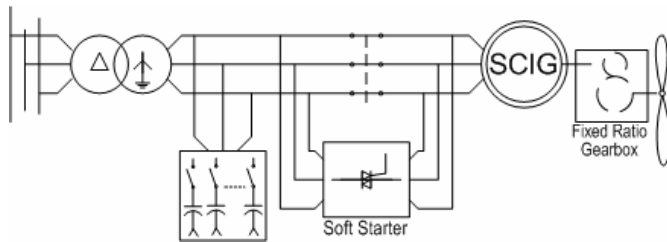

Fig. 1. Directly Connected Squirel Cage Induction Generators.

Fig. 2. Wound Rotor Induction Generator with Variable Rotor Resistance.
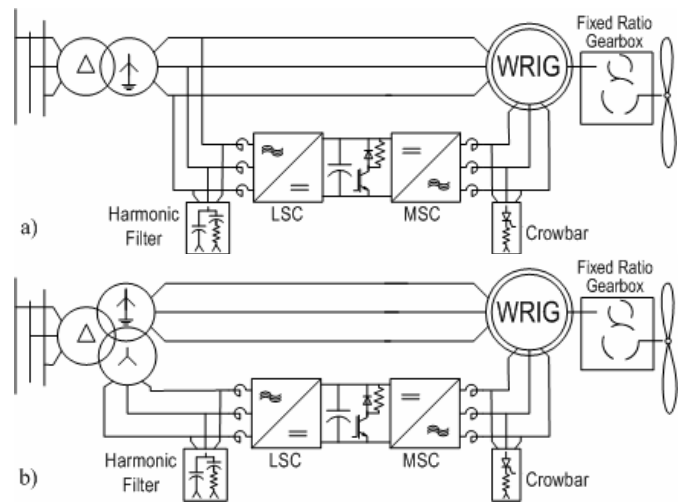

Fig. 3. Doubly Fed Induction Generator Topologies.

of the generator. This is possible due to the fact that induced emf on the rotor windings is function of not only winding transfer ratio but also slip frequency. Rotor voltage under locked-rotor condition (slip = 1) is usually on the order of 2000Vrms line-to-line while typical frequency converter voltage is 480Vrms or 690Vrms. Under normal operating conditions slip frequency varies by not more than 10-15Hz. Voltage compliance between the frequency converter and rotor becomes an issue under fault conditions and therefore a crowbar circuit must be present to isolate the converter from the machine.

The frequency converter must be capable of four quadrant operation to support both subsynchoronous and supersynchronous operation. In subsynchronous mode generator speed is slower than synchronous and the power must be supplied to the rotor circuit through frequency converter. Net generation is difference between power out of the stator and the one into the converter. Supersynchronous operation is when the rotor speed is higher than synchronous and the frequency converter also draws power from the rotor, and the total generated power sum of the power from stator windings and the converter.

Reactive power control is linear and utilizes frequency converter. Line side converter (LSC) can be used to directly inject or draw reactive current from the grid or machine side converter (MSC) can be used to over/under excite the machine.

Implementation in Fig. 3 b is used if frequency converter voltage needs to be lower than stator voltage. This may be a limiting factor in LVRT retrofitting of older turbines of such a design.

Full-scale power conversion (Full Conversion = FC) topologies are shown in Fig. 4. The name comes from the fact that full rated power is transferred through frequency converter from generator to grid. The generator can be any electric machine. SCIG, wound field synchronous generators (WFSG), and permanent magnet synchronous generators (PMSG) can be found in practical turbines.
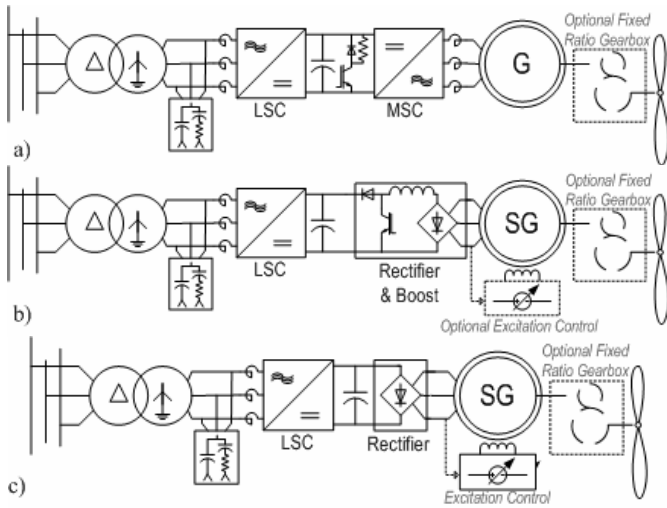
Fig. 4. Full-Scale Conversion topologies.
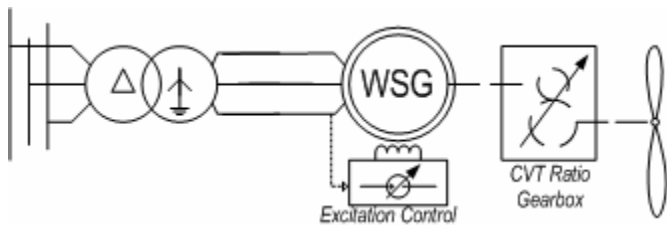
Fig. 5. Directly Connected Synchrous Generators.

The generator is completely decoupled from the grid in this configuration. Power flow is therefore unidirectional and two quadrant power converters can be applied (Fig. 4 b and c), except with SCIG where MSC is used to properly magnetize the machine (Fig. 4 a). WFSG require additional circuitry to control field current, but the rating of these devices is very small due to integrated exciter winding and rotating rectifier on the rotor. An adjustable field is desirable to either eliminate boost stage in DC bus circuit or to optimize efficiency by adjusting excitation with respect to load. High harmonic content of diode rectifier currents may impose additional requirements on generator design and diminish benefits of elimination of the MSC. MSC can also be used for field weakening operation of PMSG if this is desired to extend operating speed range or maximize efficiency.

Voltage compliance question can be raised with respect to use of PMSG and possible overspeed operation. It turns out that the voltage under these conditions does not exceed normal safety margin and a crowbar is not required.

Reactive power control is solely based on LSC which has to be sized accordingly.

The last variable speed topology is based on continuously variable transfer ratio gearbox which enables constant speed operation of a directly connected WFSG. Only WFSG can be used as the excitation control is the only possibility to regulate reactive power. There is no frequency converter in this configuration. All the complexity is moved to a mechanical gearbox.

III. GENERAL REQUIREMENTS FOR LVRT

Grid codes define requirements for the point of common coupling. The most basic of the requirements is that the turbine must remain connected to the grid during voltage sags. A number of particular system level requirements can be derived from this simplest general requirement mandated by a grid code. Some turbine systems that are typically omitted in papers on LVRT are critical for operation of the turbine. Some of those are pitch subsystem and system controller. These critical subsystems must be protected by an uninterruptible power supply (ups). An alternative approach is to connect all auxiliary loads downstream from ups.

The power rating of critical WT auxiliary loads is such that a UPS is a feasible and simple solution. The energy rating of the UPS must consider voltage sag durations which is discussed next.

A. Voltage Sag Anvelope

Every grid code will contain a definition of voltage sag based on remaining voltage in affected phase and its duration. A number of these curves from different grid codes and available LVRT turbines are shown in Fig. 6. Worst-case curve connecting maximum sag durations for given remaining voltage is also shown in Fig. 6 and denoted 'world-wide'. 'Retrofit' curve from the same picture corresponds to a commercially-available retrofitting solution discussed in section V-B. The turbine may trip if the duration of the voltage sag exceeds the duration specified for the corresponding remaining voltage.

The same voltage sag envelope is typically used for both balanced and unbalanced sags. In case of unbalanced sags, the remaining voltage is the lowest percentage value between all line-to-neutral and line-to-line voltages. This may be significantly lower than remaining positive sequence voltage, e.g. positive sequence voltage for 0V remaining line-to-line fault is 50%.

B. Power Curves

Power curves, if defined in a grid code, are as significant for LVRT definition as the voltage anvelope and much harder
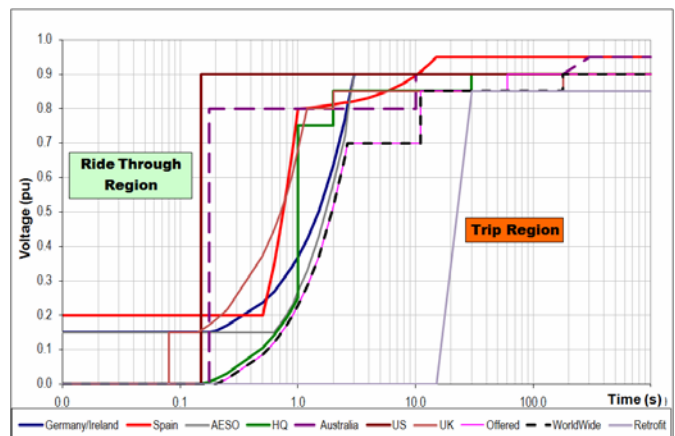

Fig. 6. Summary of LVRT Envelopes.

to satisfy than the basic requirement that the turbine must stay on line.

The significant phases in the voltage sag are sag inception transients, 'steady state' LVRT run, voltage recovery transient, and active power recovery period. These phases of voltage sags are indicated in Fig. 7. Different requirements for power curves should be defined for each of these four stages.

It is impossible to generalize power curve requirements as they vary a lot from an instance to another. For example [3] requires that injection of capacitive current during sag is proportional to active power draw from the grid, while [4] requires that capacitive current is scaled in opposite proportion to remaining voltage during sag.

Figure 7 shows ideal power curves in bold black lines and some arbitrary tolerances and non-ideal response curves. In general, power must not be drawn from the grid, voltage must be supported by capacitive current injection, and realities of real system response must be recognized and acceptable relaxed margins defined.

C. Implications

The grid codes are supposed to prescribe requirements which are best suited for the grid and equivalent to requirements imposed to existing conventional generation based on synchronous generators. The first criterion may be correct, but the second is questionable.

Examination of LVRT durations in some grid codes shows what appears to be unrealistically long time for real faults in transmission system and unrealistically deep for faults in distribution systems. Speed of reaction in reactive power control is unrealistically fast for synchronous generator
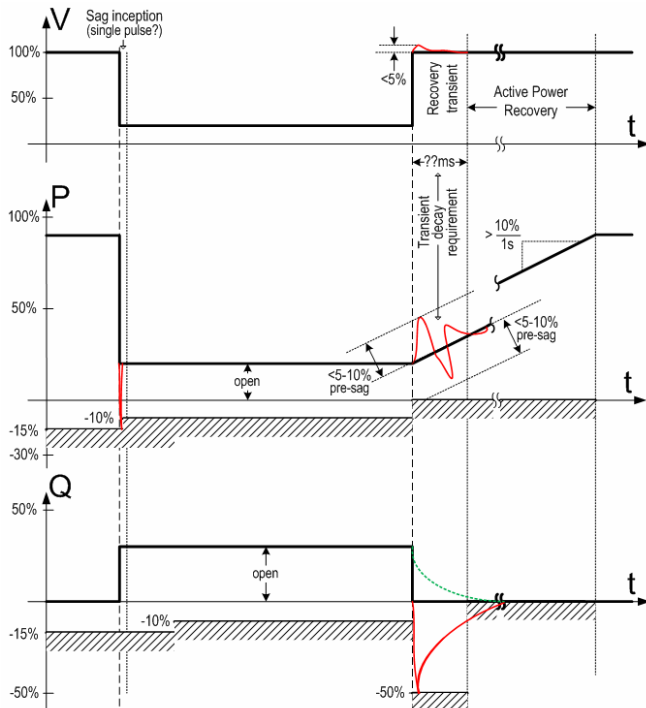
systems depending on excitation system and rotor time constants.

The bottom-line implication is that only systems which rely on frequency converters are capable of meeting these requirements.

IV. VALIDATION AND CERTIFICATION

Grid codes may be too brief in describing LVRT requirements. Since LVRT certification is typically required and regulated, the certification protocols and procedures can provide additional insight and even extend prescribed requirements. The basis for LVRT validation and certification in the field is so called sag generator – equipment for simulation of grid faults. The principal design of a sag generator, its insertion into the circuit, and power measurement details are specified in IEC 61400-21 [5] and cited or copied over into national grid codes.

A Sag generator is nothing else but a voltage divider which is inserted into medium voltage feed to an individual WT, Fig. 8. Photographs of an example sag generator are given in Fig. 9.

Per [5], the sag generator must be configured such that the short circuit current does not cause significant disturbance for the upstream windpark installation and that the short circuit power is at least three times rated power of the test turbine (1). This is adjusted by Z1 in Fig. 8, while Z2 adjusts the remaining voltage level. Desired voltage during sag is defined for no-load condition and tested with test sag prior to starting WT which then affects the actual voltage during normal operation and sag. Tolerances for the sag voltage as well as timing are also defined in [5]. Voltage tolerance prior and during sag is ±5%. It is increased to ±10% upon voltage recovery. Timing of sag inception and voltage recovery may be delayed by 20ms.

$$S_{sc} \geq 3S_r; \; X/R > 3. \tag{1}$$

Voltage sag types per remaining voltage profile are shown in Fig. 10. Typically only one sag profile is applied during certification process. In author's practical experience it would be either single sag or double sag with lower then higher


Fig. 7. Example Power Curves.
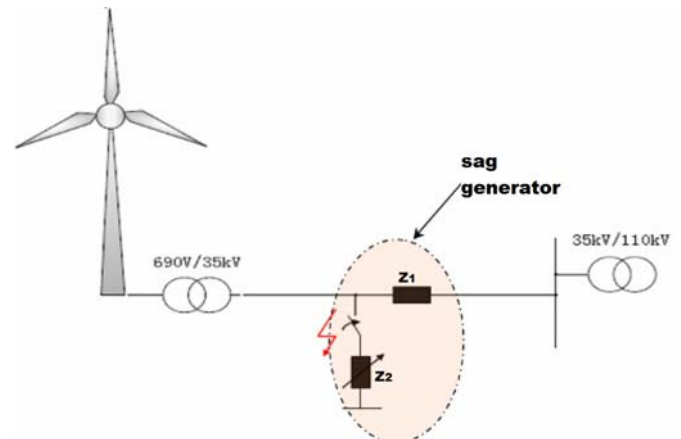
Fig. 8. Sag generator insertion into medium voltage feed.

remaining voltage. A double sag is obviously designed to test system reaction to faults on high voltage lines that do not clear before automatic reclosure is attempted.

The certification process consists of a number of test points. High-wind and low-wind conditions (i.e. high and low production) are required to be tested per [5]. High production is defined as higher than 90% rated and low is between 10% and 30% of rated power. The system has to be tested for

Fig. 9. Photographs of a sag generator.

Single

Step Sag – H/L

Step Sag – L/H

Double Sag
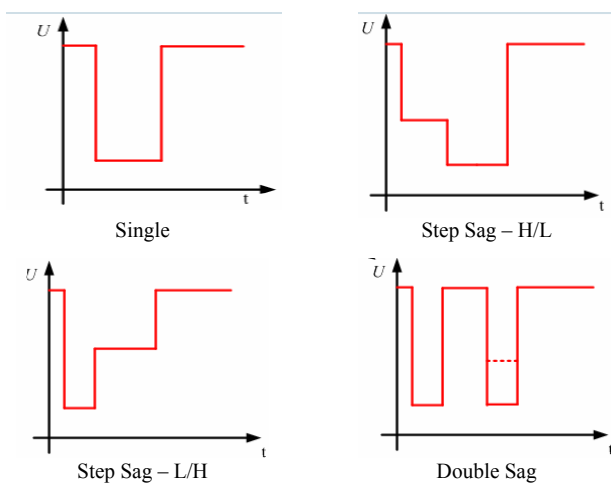
Fig. 10. Test voltage sag types.

balanced and unbalanced sags. In some cases only the deepest sags are considered, while some certification protocols require testing for a number of different sag depths and durations along appropriate voltage anvelope in Fig. 6.

The unbalanced sag that is applied during certification is line-to-line on medium voltage side. This corresponds to the most common transmission level fault which is line-to-ground and transformation through Delta-to-Wye transformer [6]. This is again seen as single phase-to-ground sag on low voltage side of WT transformer.

In addition to technical certification requirements there are a number of procedural requirements that must be followed. For example, every test point must be repeated twice. If one of the attempts fails it must be followed by two successive successful runs. Two failures may completely annul all the successful testing thus far. Needless to say, no adjustments to the system, including a parameter change, are allowed during certification.

V. RETROFITTING SOLUTIONS FOR IG TURBINES

An approach to retrofitting existing windfarms for LVRT that may seem attractive is to add shunt connected static compensators (STATCOM) to support voltage for the whole windfarm. This solution has been successfully applied for industrial applications and has been applied for some windfarms. However there are some limitations related to this approach.

STATCOM systems are sluggish in their response time due to the nature of their operation. Maximum voltage build-up is limited to 50% to 60% and even this requires a weak connection of the protected circuit to the grid. It is also more difficult to validate statcom based solutions. Individual WT retrofits are therefore preferred.

A. Series Compensators

Series compensators or dynamic voltage restorers are obvious candidates for LVRT support of WTs (Fig. 11) and are successfully implemented in practice. Their main advantage is at the same time their main disadvantage. Series compensator inverters must run at all times to pass current through series inserted transformer. This gives a chance to continuously run a voltage regulator which would automatically react to voltage sag, without a need to run a special sag detection algorithm. The reaction time is very fast and continuous. Drawback of this is that the transformer must be sized for full rated power, while the compensator inverter must be rated in proportion to desired voltage build up, e.g. 70% for operation down to 20% rated. All this corresponds to increased losses as well.

Back-to-back inverters are used (although not explicitly shown in Fig 11) to support reactive current and power flow demands during LVRT. The active power delivery to the grid is limited by remaining voltage and current rating of the equipment, while the generator output is limited only by available wind power per requirement that the retrofit
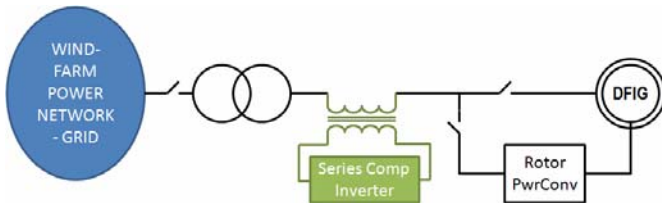
Fig. 11. Insertion of a series compensator.

solutions shall not require any modification in the existing WT controls. Therefore excess power must be dissipated within the restorer.

Modified control strategy is proposed in [7] to further improve system response and minimize converter rating. The approach is not to restore the voltage but to demagnetize IG in proportion to remaining voltage. However, this approach does not lend itself to a retrofitting application, as the protection circuits and critical auxiliary loads would have to be modified.

B. Transient Rated Full Conversion (TRFC)

A cost- and efficiency-optimized solution for LVRT retrofitting of WTs is shown in Fig. 12 and Fig. 13. It consists of a back-to-back power converter which is transient rated, mainly meaning that active cooling is not required. The Static Switch (SS) is the main power component which is rated for steady state power. The SS enables quick reconfiguration of the system from its original topology, most commonly SCIG as in Fig. 12 a, into temporary FC turbine.
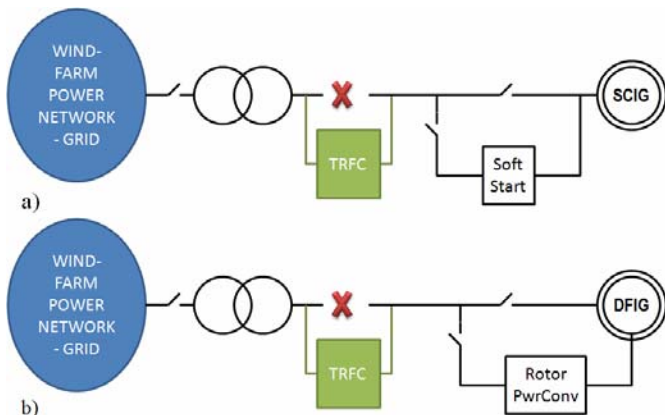

Fig. 12. Retrofitting a WT with a TRFC system.
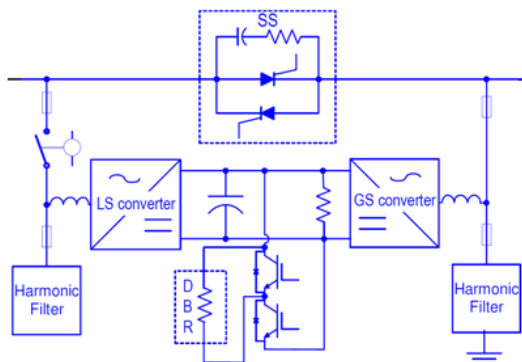
Fig. 13. Single line diagram of a TRFC.

During normal operation, power converter is in stand-by mode. Only control circuitry, harmonic filters, and DC bus are energized while whole power is transferred through the SS. Efficiency of the TRFC is extremely high as it utilizes rectifier grade thyristors. High efficiency also means simple cooling of the SS, which is very important as preferred location for installation of these systems is tower base.

Once voltage sag is detected the SS opens and the converter starts actively regulating voltage on the generator terminals and active and reactive power at grid side. Again, active power is limited by remaining voltage and shall not be limited on the generator side, so excess has to be dissipate in a hefty dynamic break resistor (DBR), Fig. 13.

Reaction speed of TRFC obviously depends on sag detection speed and commutation of SS in the first place. Fast sag detection algorithms can utilize natural reaction of a generator, like it was in test cases presented in Fig. 15 and Fig. 16, or instantaneous sequence component voltage measurements. Special care must be taken to the extraction of sequence components if the latter approach is used.

Forced commutation of SS is required for application of TRFC with DFIG turbines. Forced commutation can be accomplished by using both LSC and MSC to extinguish SS currents, Fig. 14. Forced commutation times that are fraction of a millisecond long are realistic.

Example LVRT runs in Fig. 15 and Fig. 16 are obtained on SCIG turbines where forced commutation was not used as it proved to be unnecessary. Initial transients in generator currents are used to detect sags. Resynchronization to the grid and reclosure of the SS is virtually seamless, although it may be delayed by up to several hundred milliseconds to avoid miss-detection of voltage recovery, and to ensure smooth transition. Active power delivery can be almost immediately restored upon voltage recovery as the generator and the turbine do not change their operating mode. There is no difference in performance between balanced and unbalanced sags as the generator always sees balanced voltage.

The TRFC is inserted upstream from all the loads and
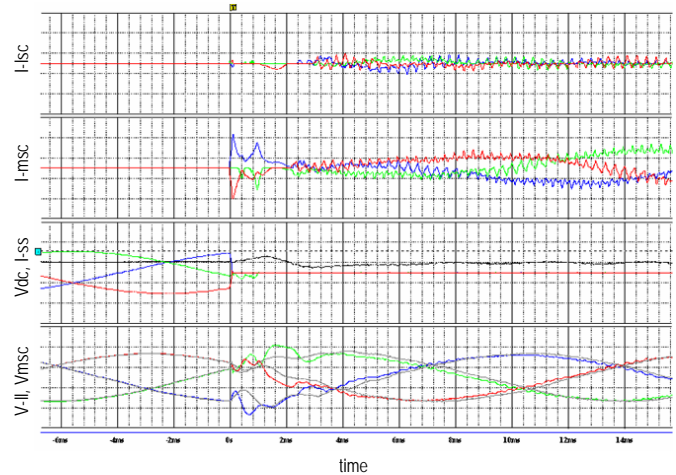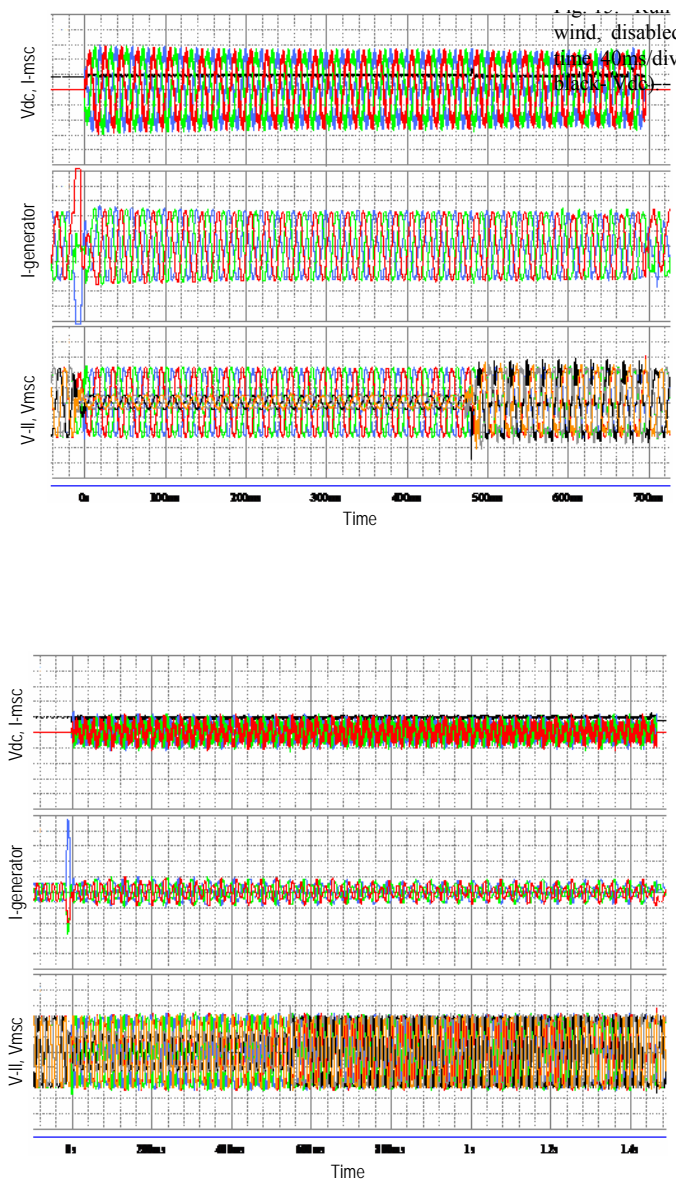
production of WT and therefore provides steady power supply for critical and non-critical auxiliaries. As a result retrofitted turbines can run through much longer voltage sags than required by typical grid codes. The only limitation to the sag duration is energy capacity of the DBR and thermal capacity of transient cold plates inside the converter.

Converter operation is always stable due to the fact that complete power generation passes through the converter during LVRT. There is always enough energy to maintain DC bus voltage. Zero volts ride through is also possible with only small changes in LSC control code.

The only drawbacks of the TRFC are its cost and small, but still-present efficiency penalty.

VI. LVRT COMPLIANT DFIG TURBINES

LVRT compliance can be achieved with DFIG turbines without significant overrating of frequency converter and expensive additional equipment. Key components in LVRT compliant DFIG design is to design it on system level and to adopt a crowbar design which enables extinction of high transient crowbar currents, Fig. 17 b and c. Standard crowbar design in Fig. 17 a cannot be used for LVRT as it requires that rotor currents naturally die out. Design in Fig. 17 b exploits fact that frozen flux causes rotor current pulsations at rated frequency for balanced and twice rated frequency for unbalanced sags. These higher frequency current components will eventually cause zero crossing and lead to natural commutation of crowbar thyristors. Design in Fig. 17 c basically duplicates design of DBR which is suboptimal solution.

Basic idea for frequency converter operation in LVRT compliant DFIG turbines is to continue normal operation as long as possible. Appropriate actions are taken only if necessary to protect and restore normal operation of the converter. This is why nuisance sag detections are acceptable in this system. On the one hand, this makes sag detection less of a challenge. On the other hand, sag detection must be based on line voltage measurements and cannot be based on machine response to sag. Voltage recovery still must be reliable as it was the case in retrofitting systems.

Some of the most interesting and most challenging aspects of LVRT DFIG design are discussed in following subsections.

A. Voltage Collapse and Voltage Compliance Issues

Existence of subsynchronous operating mode makes LVRT challenging due to possibility of collapsing DC bus voltage. If the MSC draws energy from the DC bus and LSC is not capable of drawing this energy from the grid, then the DC bus voltage inevitably will drop. On the other hand, disabling MSC would prevent the DC bus voltage collapse for some limited time, and at the cost of lost control over generator and inability to meet power curve requirements. Zero voltage ride through under subsynchronous operation would definitely create conditions for DC bus voltage collapse.

On the other hand, lack of voltage compliance in DFIG design makes crowbar circuits necessary. Frozen flux at the sag inception is stationary while the rotor rotates at speed
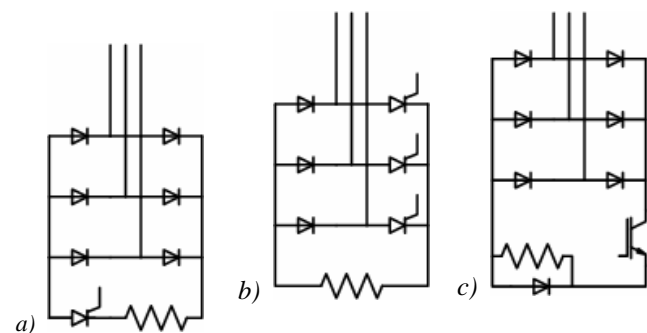

Fig. 17. Crowbar power circuits.

which is close to synchronous speed. This generates high voltage and tends to push the converter outside the safe operating area (SOA).

The voltage compliance issue is even more pronounced in unbalanced sags, where reflected negative sequence voltage has frequency of twice the rated frequency and reflects with twice the transfer ratio. Even for shallower (and therefore less unbalanced sags) where crowbar triggering is avoidable, these reflected negative sequence voltages cause control issues. The MSC voltage command could be reaching voltage limit, Fig. 18, which makes it impossible to suppress negative sequence currents. The negative sequence currents do not have to be suppressed as they do not have adverse effects per [5]. This is contrary to many scientific papers and patents which are based on suppression of these current components or compensation of the unbalance. The standard converter design for DFIG application does not have enough DC bus voltage margin to apply these algorithms. Also, voltage compensation is based on voltage drops on upstream impedance which is typically 6% for WT transformer. Complexity of those methods is disproportional to very limited benefits.

A superior approach to deal with unbalanced sags is to control instantaneous power to stabilize DC bus voltage, or even to simply ignore higher frequency components and automatically avoid steady state control error which may result from the voltage compliance issue, Fig. 18.

B. System Level Approach

Auxiliary loads of DFIG WT must be supplied through their own UPS systems since there is no possibility to restore voltage seen by them. The voltage inevitably sags for all systems. This is especially important if zero voltage ride through is desired.

Abrupt changes in generator load cannot be always avoided as some sags will cause crowbar to trigger. This may lead to turbine overspeed, and must be prevented by fast pitch reaction. Fast pitching may affect tower movement and has to be carefully tuned. Since fast pitching is not optional, it may as well be used to relieve converter torque control action.
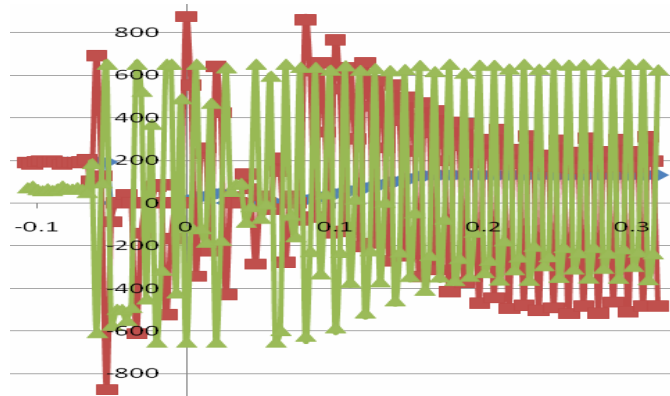
Fig. 18. Example of voltage compliance issue caused be reflected negative sequence component (red- current feedback; blue- current reference; green- voltage command).

Power recovery after voltage restores must not be too quick as this cannot be followed by regular pitch and tower movement control. This is why a slow steady ramp is desired.

C. Power Curves

One of the biggest challenges in DFIG design for LVRT is to match power curve requirements discussed in section III B. This is sharp contrast to the retrofit systems which automatically satisfy the most stringent power curves if the sag detection is fast enough and the whole system is deployed on time. In DFIG turbines it is not so hard to make the turbine stay connected to the grid, but it is much harder to accomplish sufficient command tracking to produce power curves like the ones shown in Fig. 19.

The required condition to accomplish power controls from Fig. 19 is to avoid triggering the crowbar. Simulated LVRT relying solely on crowbar is shown in Fig. 20. Here very high peaks of instantaneous active and reactive power are seen along with negative average reactive power draw during LVRT run and very high reactive power draw at voltage recovery. Subsynchronous operation would result in active power draw in addition.
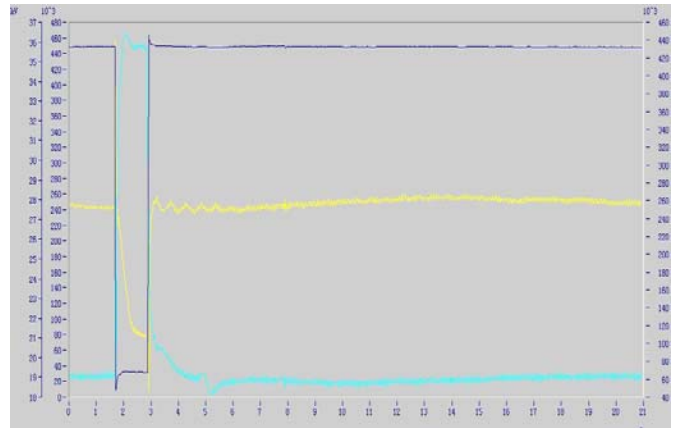
Fig. 19. Example measured power curves – 50% balanced sag, low wind (dark blue- voltage anvelope; light blue- reactive pwr; yellow- active pwr).
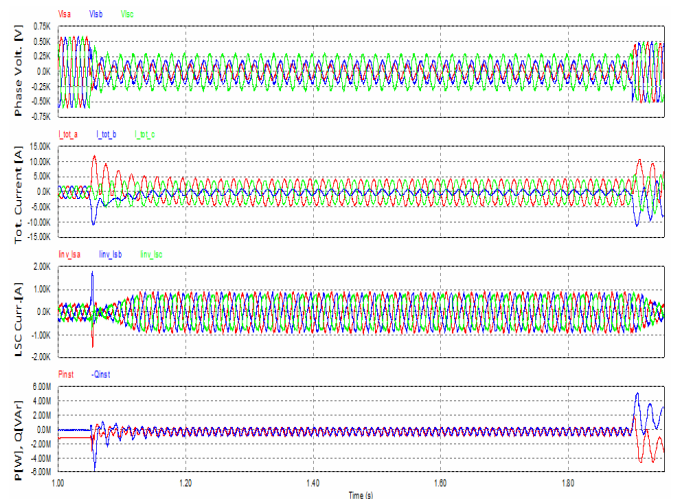
Fig. 20. Simulated LVRT with exclusive use of crowbar – unbalanced, full load.

One approach to minimize crowbar triggering during sags is to maximize effectiveness of DBR circuit. In many cases it is acceptable to trigger crowbar for very deep sags like in Fig. 21. Crowbar must trigger immediately upon sag inception to ensure reactive power production instead of consumption. This is opposing argument to maximizing effectiveness of DBR circuit. The crowbar must turn off within time allowance for inception transients, e.g. 150ms in [3]. Recovery transient is much less severe and can be limited by DBR only in Fig. 21.

VII. FULL CONVERSION

FC turbines are always configured as TRFC during LVRT run, such that all the benefits mentioned in section V, subsection B apply here as well. In addition, there are no transients related to switching operating modes like there is in TRFC. Only transients in FC LVRT come from control system reaction to step change of the voltage which is disturbance for current regulators. The step response of the converter in FC can be improved by advanced control techniques since there is no voltage compliance nor DC bus voltage collapse issues in this case.

Some system-level interaction between frequency converter controls and pitch is desirable to minimize DBR energy ratings. Sag detection would only be used for this and adjustment of power curves per grid code requirements and therefore does not need to be extremely fast or sensitive.

Unlike TRFC, auxiliary power during normal operation and LVRT has to come from grid as generator frequency and voltage vary. This means that separate UPS must be provided just like in DFIG turbines.

VIII. CONCLUSIONS

Meeting LVRT requirements is a must for significant wind power installations integrated into power grids. How this is accomplished and to which extent heavily depends on electric power conversion topology. SCIG is not compliant without expensive retrofit systems which are defeating the purpose of building WT based on this technology. DFIG is the most challenging with respect to LVRT and the amount of effort and tradeoffs can hardly justify continuing to use this technology for newest designs. Full conversion lends itself as future WT technology mostly because of LVRT.
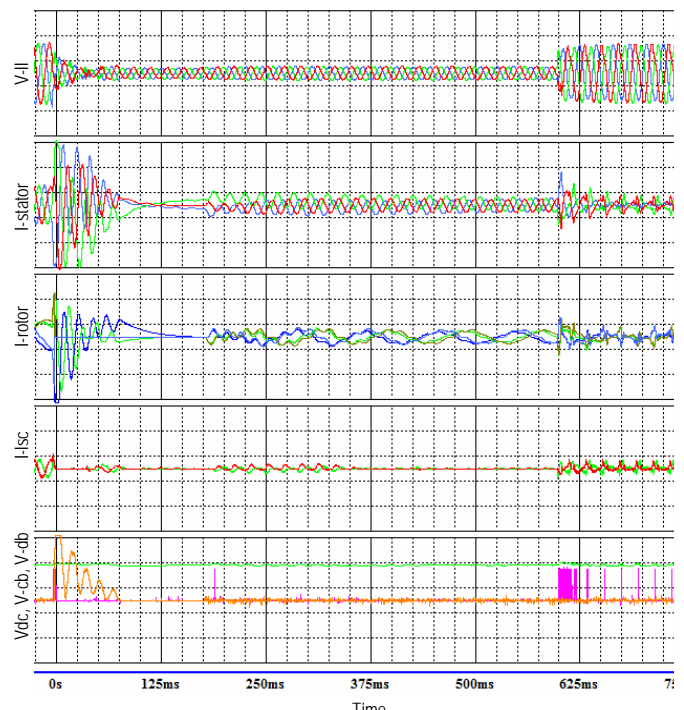
Fig. 21. Run through a balanced sag down to 20% remaining voltage – high wind. Crowbar triggers at sag inception, than clears (Full scales for each signal ±2kA/kV; time 40ms/div; red- Ixa or Vxab, green- Ixb or Vxbc, blue- Ixc or Vxca, black- Vdc).

REFERENCES

[1] [1] I. Garin, A. Munduate, S. Alepuz, and J. Bordonau; 'Low and Medium Voltage Wind Energy Conversion Systems: Generator Overview and Grid Connection Requirements,' CIRED 2007, Vienna, 21-24 May 2007

[2] [2] J.G. Slootweg, H. Polinder, W.L. Kling, "Dynamic Modelling of a Wind Turbine with Direct Drive Synchronous Generator and Back to back Voltage Source Converter and its Controls", Proc. European Wind Energy Conference and Exhibition, Copenhagen, 2001, pp. 1014-1017.

[3] [3] 'P.O.12.3 Requirements Regarding Wind Power Facility Response To Grid Voltage Dips Proposal Sent To Ministry,' BOE, Num. 254, Oct. 2006, pp. 37017-37019.

[4] [4] 'Technical rule for connecting Wind Farm to power network,' Draft Version – unpublished

[5] [5] IEC61400-21: Wind turbines – Part 21: Measurement and assessment of power quality characteristics of grid connected wind turbines, IEC, Geneve, Switzerland, 2008

[6] [6] L. Zhang and M.H.J. Bollen, 'Characteristic of Voltage Dips (Sags) in Power Systems,' IEEE Trans. on Power Delivery, Vol. 15, No. 2, April 2000

[7] [7] P.S. Flannery and G. Venkataramanan, 'A Fault Tolerant Doubly Fed Induction Generator Wind Turbine Using a Parallel Grid Side Rectifier and Series Grid Side Converter,' IEEE Transactions on Power Electronics, Vol. 23, No. 3, May 2008

Model Based Design of an Efficient CORDIC Algorithm Implementation

Volker Zerbe and Michael Backhaus

Abstract—**Navigational tasks require the efficient computation of trigonometric functions. For the development of an electronic compass the arc tangent is to be computed for example. The electronic compass is model based design. Hardware solutions are of special interest. The CORDIC algorithm stands in the focus for the computation of trigonometric functions. It is based on *shift* and *add* operations and permits an efficient implementation in FPGA`s. The paper describes the model based design concept of the compass design. It is explained how the CORDIC algorithm works. Thereby first software solutions are compared: Approximation using the Taylor series versus the CORDIC Java implementation. Different hardware solutions of the CORDIC algorithm are analyzed. A Pipeline CORDIC processor is introduced and embedded into the electronic compass. The developed system is validated using an example.**

Index Terms—**Model based design, compass, CORDIC, FPGA.**

I. INTRODUCTION

THE goal of the design task is to develop an optimal overall system under the boundary conditions of limited resources. At the same time the costs are to be minimized and the time to market is to be reduced. The question is: How can, for example, different architectures be analyzed and optimized, in order to reach this goal. First an executable system model has to be provided, before performance assessments can be accomplished. The modelling of the overall system begins on abstract level. A structured approach is essential together with the stepwise refinement of the model. The complex design problem must be divided thereby in a regulatory way into manageable subproblems, so that their complexity permits a treatment. It is important to note that the validity of the solution of a subproblem is given always only in the context of the solution of the entire design problem. This means, the solution of a subproblem does not contribute automatically to the solution of the overall problem. The solution of a subproblem is evaluated always on their contribution for the solution of the superordinate design problem. With this kind of modelling of the system with its subsystems and components over all abstraction levels,

internal system details on higher modelling levels are hidden. They emerge only in the leaves of the hierarchical model tree. The execution of the model, the simulation, now permits the analysis of the system for limited, available resources and system requirements.

For the design of complex, heterogeneous, integrated, networked systems different computation models in the architecture have to be integrated. A computation model is a mathematical formalism which defines a set of permissible operations for one computation and of implementation details abstracts. Thus, concurrencies, data flows, reactive and continuous systems, synchronisation and communication aspects can be described adequately. Each subsystem or each component of the whole to be modelled system should able to use every computation model.

Of special importance is the integration of the top down and the bottom up design for the modelling of systems. The top down methodology permits the modelling in an abstract way. The draft can be made clear and manageable. The given design space by the stepwise refined component decomposition is done until the desired degree of detail of the system is reached. With the bottom up methodology, subsystems and components are modelled and combined into an overall system. So experiences from past system developments can be brought into the design. Hence it follows that both techniques for practice must be combined. This combination of top down and bottom up is well known as the meet in the middle strategy [2]. Anyway, the main strategy should be the top down approach. In this case as much as possible alternatives can be examined and optimal decisions be made. Performance parameters can be refined stepwise or can be represented as an annotation in the system modell through the bottom up methodology. These parameters are helpfull to accomplish performance assessments of the system.

II. MODEL BASED DESIGN

At present time complex, embedded, networked systems are developed purely requirement oriented (requirement based). System requirements are gathered to provide paper specifications from different sources. On this basis many distributed developer teams develop a detailed design for the subsystems and components. After reaching an accepted design the validation and the test of the overall system is to be

V. Zerbe is with the University of Applied Sciences Erfurt, Department of Computer Engineering/Embedded Systems, Germany (e-mail: volker.zerbe@fh-erfurt.de).

M. Backhaus is with the Ilmenau University of Technology, Department of System and Software Engineering, Germany (e-mail: michael.backhaus@tu-ilmenau.de).

done. Therefore errors during the design process will be discovered often very late. The design based on executable models (model based design) has the potential to increase the productivity of the system design process substantially. This design strategy is model driven and begins already in the early design phases with the development of an executable specification. This executable specification is directly linked with the system requirements. In the center of the overall model based design process stands the to be modeled complex system, the executable model. It is refined sequentially, stepwise. By the linkage of the executable model with the system requirements inconsistencies in the system requirements can be found very timely found by simulation. During the overall design process it can be examined whether the requirements correspond to the design and which effects will be caused by the suggested change in the system requirements [4]. The model based design has the following conspicuous characteristics in relation to the requirement based design, (in extracts):

- The investigation of the dynamic behavior of the system becomes already possible in the early phases of the design process.
- Based on simulatable alternatives and associated trade off analyses design decisions can be made.
- Only one model is used on different design levels.
- Nonfunctional requirements can also be modelled and validated.

III. MLDESIGNER

MLDesigner [10] is a tool for the design of complex systems on mission and system level. This approach integrates architecture, function and application scenarios in only one development environment on a very abstract level. MLDesigner is a multi domain simulator and supports the modelling in discrete event (DE), synchronous data flow (SDF), continuous time (CT), finite state machine (FSM) and other computation models. Different computation models can be combined in order to model a system [12]. Furthermore a system model can be represented with its components in an arbitrary depth of detail. On this basis system performance evaluations can be accomplished. A comparison and an evaluation of different tools for the design on system level was made in [11].

IV. THE ELECTRONIC COMPASS MODEL

An electronic compass is able to continuously indicate [6] the azimuth angle. Two magnetic field sensors, KMZ51 by Philips, generate voltages V_x and V_y from which the azimuth can be determined then.

$$\alpha = \arctan \frac{H_{ey}}{H_{ex}} = \arctan \frac{V_y}{V_x} \qquad (1)$$

H_{ex} and H_{ey} are vectors in the earth field, see Fig. 1.
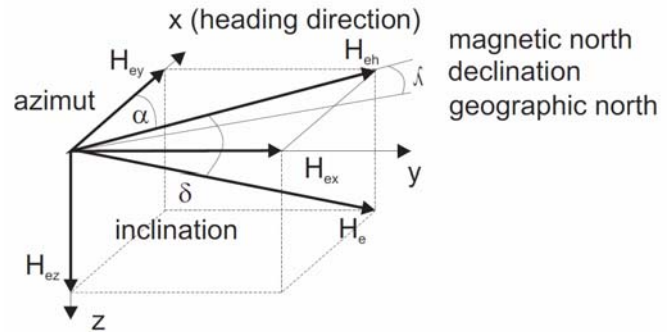
Fig. 1. Earth field vectors.

This picture shows three dimensional the earth field vectors. The $x − y$ plane lies parallel to the earth surface. The azimuth has to be computed. The angle δ, the inclination, is the tilting angle of the magnetic field lines. This angle is different for different positions on the earth (at the north pole differently than in Ilmenau or at the equator). The declination, λ, between magnetic and the true geographic north amounts to approximately 11,5 degrees.

An executable model for an electronic compass was developed with the help of the system design tool MLDesigner. The to be modeled system is a data flow oriented system [1]. One source (magnetic field sensor) produces continuously tokens ($x − y$ voltage data) which are consumed by the following nodes (amplifier, converter, processor, display). Basis for the modeling is the SDF computation model. The goal is the development of an optimal overall system. Fig. 2 shows the overall system of an electronic compass. The model can be formally verified. For example for SDF graphs the following applies:

Definition 1 (Deadlock): Is a computed Schedule not more continuable, since no more node can fire, then a deadlock is present. Cycle free graphs are deadlock free.

The top level compass model is therefore deadlock free in the sense of a SDF graph.

The module sensor supplies corrected (offset, sensitivity, orthogonality, temperature compensation) sensor outputs (voltage data). An operational amplifier circuit, modeled in the module *amplify*, is amplifying the weak sensor output signal. These voltage data are analogue digital converted in the module *A/D Conv*. Here for example different parameters for converters are adjustable. The computation of the arc tangent is modeled as a main function in the module *CORDIC processor*. Pure software solutions are examined based on the Taylor series and the CORDIC implementation. Further the
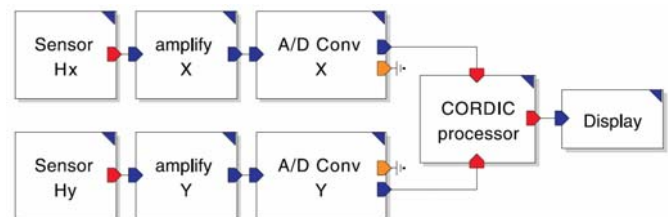
Fig. 2. Top-Level MLDesigner Compass Model.

focus is directed on a FPGA (field programming gate array) implementation. The module *display* is a data sink. Only tokens are consumed. The azimuth angle α is written as output data.

A. The CORDIC Algorithm

The CORDIC algorithm was introduced 1959 for the first time by Jack Volder [5]. CORDIC is the abbreviation for coordinate rotating digital computer. Starting point for the development of the CORDIC was the desire to handover the continuous computation of navigation algorithms to digital systems. The world of the digital signal processing is dominated by microprocessors. On one side they are low priced and extremely flexible, on the other side they are often not really fast enough for heavy DSP (digital signal processing) tasks. Available reconfigurable hardware makes it possible to achieve a higher speed in computation compared to the traditional software approach. Unfortunately for microprocessor based systems, optimized algorithms are not well implementable in hardware. Nevertheless, there exists a multiplicity of hardware efficient solutions. Among them there is also a class of iterative solutions for trigonometric functions. John Walther [7] extended the CORDIC theory. Thus using the CORDIC computation of hyperbolic, exponential and logarithmic functions are also possible. Kota [8] has accomplished error and load analyses.

All computations of trigonometric functions are based on vector rotations. The vector E_0 is rotated around the angle θ, see Fig. 3. The vector E_n results.

$$x_0 = \cos\theta_0 r_i \qquad\qquad y_0 = \sin\theta_0 r_i$$
$$x_{i+1} = \cos(\theta_0 + \theta)r_i \qquad y_{i+1} = \sin(\theta_0 + \theta)r_i$$

The general rotation transformation in matrix form results to

$$\begin{bmatrix} x_n \\ y_n \end{bmatrix} = \begin{bmatrix} \cos\theta & -\sin\theta \\ \cos\theta & \sin\theta \end{bmatrix} \cdot \begin{bmatrix} x_0 \\ y_0 \end{bmatrix} \qquad (2)$$

or in a different way of writing:

$$\begin{bmatrix} x_n \\ y_n \end{bmatrix} = \frac{1}{\sqrt{1+\tan^2\theta}} \begin{bmatrix} 1 & -\tan\theta \\ \tan\theta & 1 \end{bmatrix} \cdot \begin{bmatrix} x_0 \\ y_0 \end{bmatrix}.$$

The rotation around the angle θ is realized by a sequence of rotations around the angular α_i.

$$\theta = \sum_{i=0}^{n-1} d_i \cdot \alpha_i \quad \text{mit } d_i \in \{-1,1\} \qquad (3)$$

The angle θ is approximated by an alternating approach. A too far rotation is compensated by a change of sign. To control the direction of the rotation an auxiliary variable z_i is introduced.

$$z_0 = \theta \quad z_{i+1} = z_i - d_i \cdot \alpha_i \quad d_i = \begin{cases} 1 & z \geq 0 \\ -1 & z_z < 0 \end{cases}$$

In order to simplify the rotation equation [9], the rotations are replaced by pseudo rotations, see Fig. 4. Thus the length of the rotating vector changes by a well known angle with a constant factor.

$$r_{i+1} = r_i \cdot \sqrt{1 + \tan^2\alpha_i} \qquad (4)$$

Let $\tan\alpha_i = 2^{-i}, \quad i = 0...n-1$.

Thus the following new, simplified rotation equations result:

$$\begin{bmatrix} x_{i+1} \\ y_{i+1} \end{bmatrix} = \begin{bmatrix} 1 & -d_i \cdot 2^{-i} \\ d_i \cdot 2^{-i} & 1 \end{bmatrix} \cdot \begin{bmatrix} x_i \\ y_i \end{bmatrix} \qquad (5)$$

$$z_{i+1} = z_i - d_i \cdot \arctan\left(2^{-i}\right) \qquad (6)$$

For the computation of the different functions the CORDIC can operate in two modes. These are the rotation and the vector mode. For the computation of the arc tangent the vector mode is used. The given vector is always rotated so that the absolute value of its *y* component is reduced. The rotation angle is signed accumulated thereby. After processing all iteration steps, the following equations results:

$$x_n = \left(\prod \sqrt{1 + 2^{-2i}}\right)\sqrt{x_0^2 + y_0^2}$$
$$y_n = 0 \qquad (7)$$
$$z_n = z_0 + \arctan\frac{y_0}{x_0}$$

Choose $z_0 = 0$, so z_n is equal to the desired azimuth.

B. Algorithm Analysis

In the module CORDIC processor, see Fig. 2, the arc tangent is modeled. First an approximation, using the Taylor series, is compared with the CORDIC algorithm. Both algorithms were implemented directly in the MLDesigner model using the programming language C.

  1) **Approximation using the Taylor series**

    Taylor series expansions sometimes show a slow convergence and a numeric instability and require many multiplications additionally. The description complexity is nevertheless low, see the following Java code.


Fig. 3. Vector transformation.
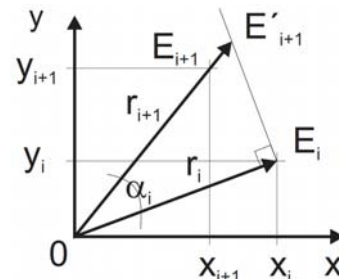
Fig. 4. Pseudo rotation.

```
public static double taylor_atan2(double y,
double x, double math, int n){
  double z=y/x;
  double result=0;
  double numerator=z;
  double denominator=1;
  z*=z;
  for(int i=0; i<n; i++){
  result+=enumerator/denominator;
  numerator*=-z;
  denominator+=2;}
return Math.toDegrees(ergebnis);
}
```

2) **CORDIC Java implementation**

In comparison with the approximation using the Taylor series the CORDIC needs only simple shift and add operations as well as a LookUpTable operation. The description complexity is comparable with that of the Taylor implementation.

```
public static double cordic_atan2(double y,
double x, int n){
  double newX;
  double z = 0;
  double half=1;
  int d=1;
  for(int i=0; i<=n; i++){
  if(y>=0) d=-1; //direction of rotation
  else d=1;
  newX=x-d*half*y;
  y=y+d*half*x;
  x=newX;
  z=z-d*angles[i]; //precalculated angles
  half/=2;}
  return z;}
}
```

The simulation of both modeled algorithms produces the following results, which are exemplary summarized in a table. First the number of iterations was investigated, which leads to an accuracy of $\leq 0.001°$ concerning the reference angle.

x	y	ref. angle	CORDIC (iterations)	Taylor (iterations)
0.92	0.39	22.97272	12	5
0.72	0.69	43.78112	14	64

If the number of iterations is set to 16 for both algorithms, then the accuracy of the results varies very strongly. In particular the Taylor algorithm shows clear weaknesses regarding the accuracy, see table below.

x	y	ref. angle	CORDIC (error)	Taylor (error)
0.92	0.39	22.97272	0.0134	0.0000
0.72	0.69	43.78112	0.0115	0.2286

The CORDIC obtains a high accuracy of the computed result for a constant number of iterations in the entire coordinate system. Introducing the pseudo rotations and the represented simplifications the CORDIC is limited to only two

shift, three *add/sub* operations and one *LookUpTable* operation. That way the system is also efficient implementable in hardware.

In the sense of the model based design the CORDIC processor, see Fig. 2, is now modelled in a third variant with MLDesigner using logic elements/finite state machines (FSM). The specified CORDIC is validated in the context of the compass model by simulation. This validated specification is the basis for an implementation on a Cylone II EP2C35 FPGA, or in other words, the validated MLDesigner model is input for the Quartus II Web edition, the FPGA development environment of the company Altera.

V. IMPLEMENTATION

For the implementation in hardware different design variants are possible. These designs differ regarding the execution time, hardware costs (number of logic cells) and the principle suitability for the implementation on a FPGA.

1) **Bit parallel iterative CORDIC processor**

Each of the three to be solved functions x_n, y_n and z_n are directly implemented in hardware, see Fig. 5. The shown processor represents an iterative CORDIC structure.

The function for the determination of the direction of rotation d_i determines itself in the rotation mode through $sign(z_i)$ and in the vector mode through $sign(y_i)$. At the beginning of the processing the initial values x_0, y_0 and z_0 are loaded into the registers. This is done via the upstream multiplexers. In one iteration step the values are loaded from the registers into the adders/subtracters and the shift registers. The results of the computations are then loaded again into the individual registers via the multiplexers. The angles for the computation of z_i are stored in successive addresses in a ROM. So one sufficient incremental access is enough. After processing of the last iterations the result of the respective variables can be read directly at the outputs (the adders/subtracters). In this design the arithmetic and the shift operations are implemented with data word length. This implementation does not lead to an efficient solution. The signals are passing a high number of FPGA cells. This leads to a slow design with a high number of logic cells.

2) **Bit serial iterative CORDIC processor**

A more compact method arises as a result of the use of bit serial arithmetic. A substantially higher clock than in the bit parallel variant is reached. This design consists of three bit serial adders/subtracters, three shift registers as well as one serial ROM. Thus it needs a minimum of hardware costs. The shift registers are in the length wise identical to the word length. For the initialization the data are loaded into the shift registers via the multiplexers. Each iteration
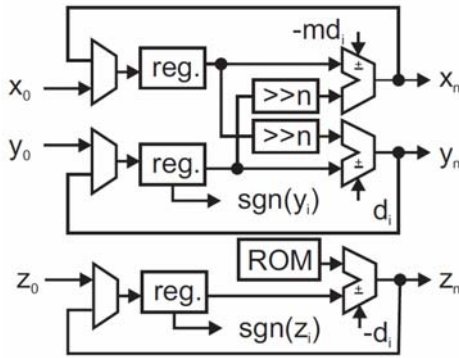
Fig. 5. Bit parallel iterative CORDIC processor.

needs exactly w clock cycles (w is the word length). The whole word is loaded into the adders/subtracters and afterwards it is pushed again into the shift registers. At the beginning of every step the sign of the variables is read and passed on to the adders/subtracters. After the last iteration the words are pushed to the outputs, at the same time a new word can be initially loaded again already. The advantage of this design is in the simple and minimal hardware. This permits to work with a very high clock frequency, which is necessary for the high number of clock cycles.

3) **Bit parallel combinatorial CORDIC processor**

Beside the iterative design variants, where n iterations for the computation are needed, there are also other possibilities to implement the CORDIC. One of these possibilities, described in [13], is the so called *unrolled CORDIC processor*. The idea thereby is to implement the hardware for every individual iteration step. This design variant is shown in Fig. 6.

This structure has some advantages. Because each iteration uses their own elements, always the same operations are executed. So the shift registers are not required and can be hard wired, because the same
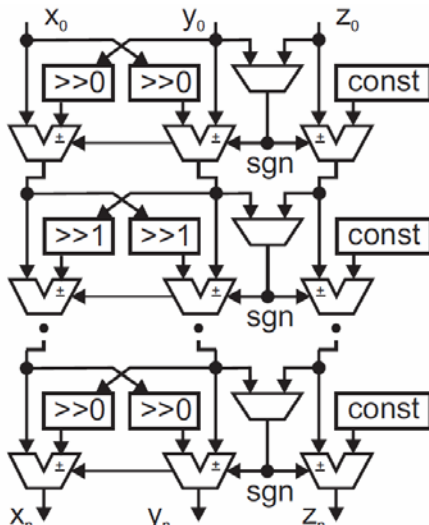

Fig. 6. Bit parallel combinatorial CORDIC processor.

number of shift operations always achieved. The same is valid for the angles. They are a constant for each iteration step. That means, there is no need to use memory and the values are likewise hard wired. So there is no need of registers at all. The structure reduces the number of adders/subtracters. But that purely combinatorial structure has also its disadvantages. The processing time is accordingly high due to the multiplicity of the elements. However this structure is faster than those of the iterative variants, because the time for initialization and setup and hold of the registers is completely omitted.

4) **Pipeline structure**

The preceding structure is simply implementable as pipeline structure. Between the *add* and *sub* blocks pipeline registers are connected. So for a pipeline architecture only a few additional hardware costs are needed. The advantage is that with a filled pipeline after each clock a result can be read on the outputs.

Particularly the variants of bit serial iterative CORDIC processor and the pipeline structure were examined. Both MLDesigner models are transformed into the Quartus II model. The chip analyses show the following results:

	Bit serial iterative	Pipeline structure
Logic elements all	1469	2526
Logic elements CORDIC	887	1934
number register all	640	1477
number register CORDIC	121	958

In the compass implementation for the computation of the arc tangent the pipeline structure was used. The clock diagram, see Fig. 7, shows for every clock the data at the input of a pipeline step. The steps 1, 2 and 5. are represented.

On the basis of the CORDIC pipeline structure the complete compass was implemented on a FPGA. The top level compass des ign is shown in Fig. 8.

The system is simulated/validated in the tool chain: MLDesigner, Quartus II Web edition and tested as a real system. As a test scenario a rotated house of the St. Nicholas is used, see Fig. 9. A real scenario could be a navigational task in a robot system [3].

When pacing down the house of the St. Nick the compass continuously supplies the expected azimuth angles per clock, see Fig. 10. The implementation runs with 50 MHz and the individual blocks from figure 8 have the following number of
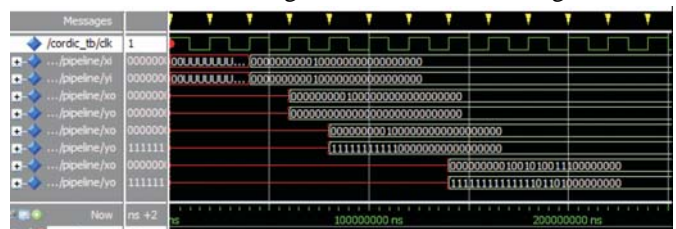

Fig. 7. Waveform.
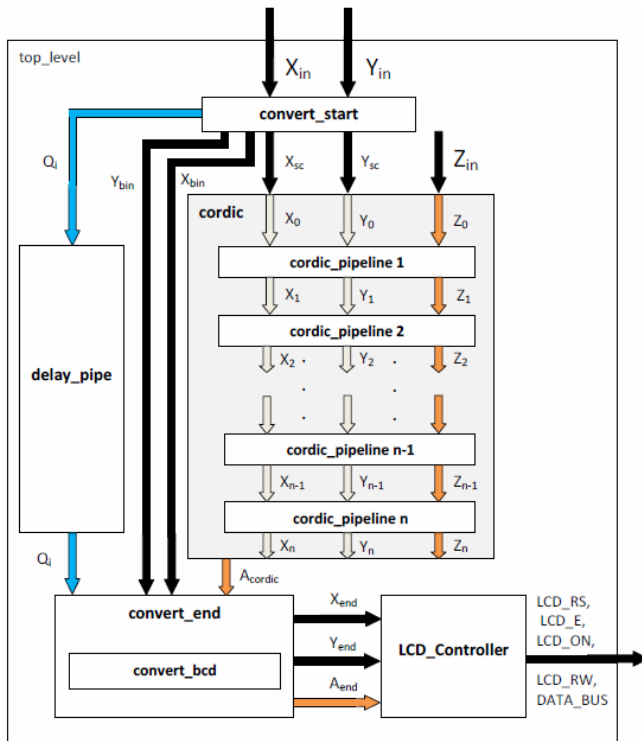
Fig. 8. Top-Level compass design.

Fig. 10. Angle output for the house of St. Nick.

the special focus stands thereby the CORDIC algorithm. The model was stepwise refined and implemented by Quartus II on a FPGA. It was shown that the model based design using a tool chain allows extensive analyses and generates a fast, clear implementation.

Fig. 9. House of St. Nicholas.

clock cycles:

- convert_start   3 clocks
- cordic_pipeline 16 clocks
- convert_end   2 clocks
- convert_bcd   6 clocks

VI. CONCLUSION

An electronic compass has been developed consequently model based. First an abstract system model was built using MLDesigner. So already in the early design phases performance analyses for system could be accomplished. In

REFERENCES

[1] E. A. Lee, D. G. Messerschmidt, Static Scheduling of Synchronous Data Flow Programs for Digital Signal Processing. IEEE Trans. Comput. Vol C-36, no 1 pp. 24-35, Jan. 1987.

[2] K. D. Mueller Glaser, Systems Engineering in Microsystems Design. IFIP Workshop on Modelling of Microsystems. Stirling Scotland, 1997.

[3] M. Milushev, N. Krantov, V. Zerbe, Scalable Modular Control Architecture for Walking Machines. ICEST 2007, Ochrid, Macedonia, 24-27 June 2007, pp. 901-903.

[4] F. Lohse, V. Zerbe, Model based Performance Estimation in ZigBee based Wireless Sensornetworks. 27th MIEL 2010, IEEE International Conference on Microelectronics, Nis, Serbia, 16-19 Mai 2010, accepted.

[5] J. E. Volder, The cordic trigonometric technique. IRE Transactionon Electronic Computers, EC-8, pp 330-334, 1959.

[6] B. Andjelkovic, V. Litovski, V. Zerbe, A Mission Level Design Language Based on AleC++. MIEL 2006 - 25thIEEE International Conference on Microelectronics, Nis, Serbia, May 14-17 2006, pp 659-662.

[7] J. S. Walther, A unified algorithm for elementary functions.Spring Joint Computer Conf., 1971, pp. 379-385.

[8] K. Kota, J. R. Cavallaro, Numerical Accuracy and Hardware Tradeoffs for CORDIC Arithmetic for Special-Purpose Processors. IEEE Transactions on Computers, Vol. 42, NO. 7, 1993, pp. 769-779.

[9] B. Parhami, Computer Arithmetic: Algorithms and Hardware Designs. Oxford University Press, USA, 1999.

[10] http://www.mldesigner.

[11] A. de A. Agarwal, C.-D. Iskander, R. Shankar, G. Hamza-Lup. System-Level Modeling Environment: MLDesigner. SysCon 2008, IEEE International Sys-tems Conference, Montreal, Canada, April 7-10 2008.

[12] I. Paunovic, V. Zerbe. Modeling and Simulation of Digital Systems in different Domains. 3rd SSSS- Small Systems Simulation Symposium, Nis, Serbia, February 12-14 2010, p. 17-23.

[13] R. Andraka. A survey of cordic algorithms for fpga based computers. 6th ACM/SIGDA International Symposium on Field Programmable Gate Arrays, 1998, New York, USA, p. 191-200.

CAE Application and Certification for Industrial and Educational Customers
The Case of University-Industry Cooperation between EPLAN and RFH

Duško Lukač

Abstract—The paper presents examples of the application of the currently most used CAE software for electrical engineering and project planning EPLAN Electric P8 as well as novel international certification model, of the so called Eplan Certified Engineer (ECE) and EPLAN Certified Student, based on cooperation between Rheinische Fachhochschule Köln gGmbH – University of Applied Sciences in cooperation with EPLAN Software and Service company, a market leader in development and training in electro CAE. It argues that the successful interface management, communication plan and the costumer oriented technical-didactical model of the concept has been essential for the viability and success of the courses. It concludes that cooperation between the industry and university enhances the university's and firm's reputation with consumers and environmental competitors and has had positive financial effects for the both parties. It concludes that on the whole, these joint certification programs have a convenient side effect, like to be the successful way for the development of high-quality training opportunities for the students.

Index Terms—Standardization, CAE, CAD, EPLAN Certified Engineer (ECE), Third-party CAE/CAD Certification, Reverse Engineering, Inplace Editing.

I. INTRODUCTION

EPLAN Electric P8 is CAE database driven software for designing of electrical engineering systems. It uses freely selectable graphical/object orientation & variant technology and offers diverse functions like interfacing article reports, revision management etc. It is most used CAE application in the industry and applied by most import and industrial companies like companies out of automotive segment (Volkswagen, BMW, Mercedes and Ford etc.) or other known international industrial companies. It becomes as a quasi-standard in the CAE application. Institutions of higher education, industry, non-governmental and governmental organizations each achieve economic, scientific, and strategic advantages from collaboration [1]. Their incentives for collaboration are epistemic, didactical and also political, with the reflection of the marketing needs [2]. Obstacles to cooperation and collaboration contain industry limits, appropriation of study, communication difficulties, and also national [3] and organizational cultural differences. Sometimes also industry and institutions of higher education often have dissimilar time horizons [4]. There are different possibilities to strength collaborations as for instance to use a legal framework and intermediaries. With this in mind, Rheinische Fachhochschule Köln gGmbH (RFH) – University of Applied Sciences has started the first conversations with the representatives of the EPLAN Software and Services (EPLAN) company in July 2006. The RFH is the biggest and oldest German private university. EPLAN is a worldwide leading CAE software developer in the area of electrical engineering, mechatronics and process and investment planning. The company has a contract with more than 60000 licensees worldwide. Gradually the high-level talks have been initiated and the cooperation intention has been developed and underlined with signification of the letter of intent. The letter of intent has defined the first time horizons, the main subjects of the collaboration as well as the framework and the content of the collaboration. After several reciprocal visits of the RFH and EPLAN by the representatives of the company and university cooperation has been established in October 2008. The cooperation concerns the realization of the so-called ECE (Eplan Certified Engieeer) assessments, whereby the RFH take on the role of the Third Party Certifier.

II. BACKGROUND AND MOTIVES OF COOPERATION

The ECE assessment as a quality standard assessment, servers to evaluate the quality of the theoretical and practical knowledge of the examinees who are using the EPLAN product Electric P8, which is in the meantime the standard-software used in the German and European industry, particularly in the German automotive industry and companies like Volkswagen, Mercedes or BMW [5]. As is known, automotive industry in Germany is one of the major employers in the country, with a well-built workforce of over

D. Lukač is with the Rheinische Fachhochschule Köln gGmbH – University of Applied Sciences, Department of Mechatronics, Vogelsanger Strasse 295, 50825 Köln, Germany (phone: +49-221-5468759; fax: +49-221-5468755; e-mail: lukac@rfh-koeln.de).

866,000 working in the manufacturing and trade. Additionally, Germany has the largest share of passenger automobile production in Europe with more than 29% market share [6]. Consequently the multi-purpose impact of automotive industry is huge. The idea for the establishment of the CAE quality standard assessment has been initiated by the German automotive industry in 2005, for the most part by the Volkswagen, which has in this regard addressed EPLAN Company. The reason of the establishment of the quality standards in CAE application has originated, because many supplier's companies which are working for automotive industry, have not made available high-grade qualitative electric engineering wiring diagrams and electro project engineering plans made with the software Electric P8. These led to higher costs because of the time-consuming reviewing of faulty plans. For the long-term directives and norms used for the establishment of the sustainable quality standards an independent quality assurance institution (RFH) has been integrated in the concept. As an independent institution, RFH has undertaken the task of the development of the regulation and contents leading to sustainable quality CAE standards as well as the development of the assessment procedure. It includes also the allocation of the all resources needed for the realization of the effective assessment. It must be independent from the exam location, because the assessment is to be offered to the customers in Germany and worldwide.

III. COOPERATION BENEFITS, ELEMENTS OF COURSE DESIGN AND KEY SUCCESS FACTORS

In times of increasing competition the success of an enterprise depends decisively on productiveness and qualification. Not only the choice of the suitable, achievement-raising software is important for the success, but also the professional handling of the system documents the company's competence face to face with customers. Thus it surprises nobody that the subject "Certification" has won in importance. Enterprises profit more and more from the use of the uniform defined high-class standards, to set themselves apart from the competition and to guarantee the investment security for their products and services. As an EPLAN certificated supplier, the firm stands professionally in their market segment and documents with it the uniform high-class standard, extensive specialist knowledge and competence. Companies indicate to their customers that high-class aspects stand in the center of their enterprise activity. Thus the companies do achieve a clear competitive advantage compared with the not-certificated suppliers [7]. Due to the fact, that a „certificate" is individual-related matter, the idea has originated that the company receives the status as "EPLAN certificated supplier" then, if at least one company's employee has successfully passed the ECE-assessment. Thus the company keeps this status, as long as these employees (owners of the ECE certificate) remain to stay employed in the company. On account of this idea the different benefit aspects came well along, which arise from the user's view, company's

point of view, from the point of view of the EPLAN company and the RFH Unviersity. These will be subsequently explained in gretaer detail below. Customer value of ECE certification
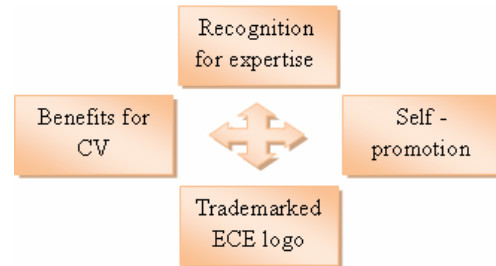
Fig. 1. Customer's benefits of ECE certification.

can be specified as in the Fig. 1.

The owners of the certificate receive recognition for their expertise from their employer. The curriculum vitae of the certificate-owner shows a point, the recruiter considers beneficial. Owners of the certificate receive an ECE logo which they can freely use even for the business purposes, as an advertising for the own business. The ECE logo is legally protected by the EPLAN company and may not be misused.

Fig. 2. Eplan Certified Engineer logo ©.

The ECE logo is presented in Fig. 2.

The profile of owner of the certificate can also be published on the web page of the EPLAN company. For that case RFH University forwards the data of the candidates they passed the ECE exam to the EPLAN company, assumed the customer agrees in co-ordinance with the data security regulations, that his/she's data may be forwarded and published. On this way, everybody can publicly see who the owners of the ECE certificate are [8]. The ECE certificate is issued by RFH University. Furthermore but, behind the certificate issued by the RFH University, owners of the ECE certificate upon request can receive a further high-quality certificate document from EPLAN company. Moreover there are benefits for the EPLAN company and the RFH University which arise from the ECE certification. Firm's value of ECE certification can
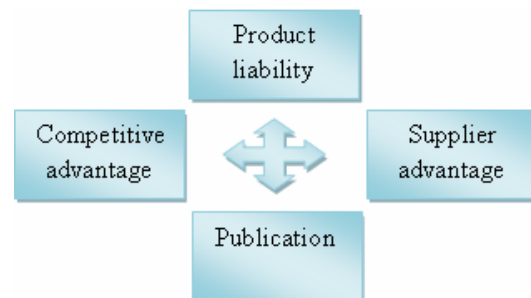

Fig. 3. Company's benefits of ECE certification.

be specified as in the following:

With the certification the firms have a juridical security in the product liability, because of the comprehensible proof of the service quality, offered with the Electric P8 product. On the one side the firms have advantages in the market segment compared with not-certificated competitor and on the other side certification represents a demonstrable high-class standard in the supplier's circle.

Also the enterprise profile is published on the web page EPLAN analogical to the publication of the user's data. Certification benefits for RFH University can be specified as in the Fig. 4. For the RFH University there are many benefits arising through the Third Party Certification. According to agreement the RFH receives a free advertisement done by the EPLAN company. During the every product training offered in by the EPLAN company, trainers are instructed to inform the customers about the ECE certification at RFH. Having in mind that EPLAN has 59 subsidiaries worldwide and there from 16 in Germany, the advertising effect is very high. Furthermore EPLAN is regularly advertising also in the professional journals and trade magazines, in internet and other advertising channels. ECE certification is also offered to the students and employees of the RFH university to the reduced price of currently 150 € excl. VAT. It is a benefit for all RFH students and employees, not only because of the reduced price but also because this certification is unique at German universities. The good reputation of the university becomes therefore achieved. At least university gains a substantial financial benefits because the regular customers have to pay 300 € excl. VAT for the 90-120 min on-line assessment. The overhead costs are less, because assessments is carried out with the open source software and needs to be updated every 2 years, with the issuing of the new EPLAN Electric P8 product. The re-certification of the certificate owners is therefore necessary every 2 years. This leads to increasing of the customer pool and consequently to the sustainability of the financial benefit for the university, because for every new certification procedure the costs become due. The ECE certification becomes since 2009 international. The benefits of the internationalization are huge. RFH has a free and improved market access in the EU and worldwide due to possible cooperation with the potential supports of the ECE assessment, which can be licensed. Also the financial advantages increase, without additional resource input. The assessment is offered for the international

Fig. 4. University's benefits of ECE certification.

customers in German and English language and in these languages exams are available. EPLAN's value of ECE
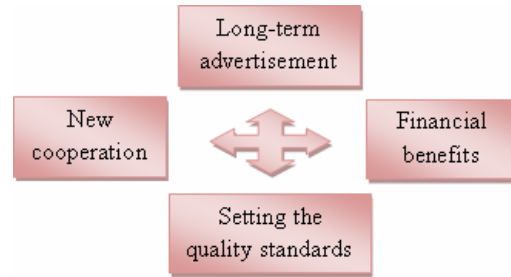

Fig. 5. EPLAN's benefits of ECE certification.

certification can be specified as in the following:

The EPLAN company issues unique standards in creation of the quality standards in the domain of electric engineering and project engineering. The ECE certification can be treated as a stamp of quality for the professional application in electrical CAD. Also the company is achieving the financial benefits because it offers special tailored preparatory courses for the ECE exam. Furthermore, it develops good relationships to the university and can expect the new beneficial cooperation in other areas. EPLAN Electric P8 software is according to agreement between RFH and EPLAN company, also installed and used at RFH University. Thus company gains advantages in long-term from the advertising done at university, because the students learn the advantages of the product, learn to apply it in working environment and can convince the future chiefs of the product advantages. To ensure the successful cooperation, the procedures about the sharing of information have been defined between RFH and EPLAN. It includes the regularly update of the assessment according to the new releases of the Electric P8 software to ensure the actuality and therefore high quality of the assessment. The technical interfaces have been defined, which are including the planning of the examination dates and exam locations for the practical part of the ECE certification. According to the basics of the project management and therein defined communication matrix, key accounts have been defined on both sides, so that the communication flows smoothly. One example for it is that the RFH and the EPLAN are simultaneously informed about the filling the online-application for the assessment with all relevant data, about the assessment date, location etc. Regularly meetings are organized, as well as the evaluations of the feed-backs given by the customers. Mutual respect is of course one of the main keys to success of every collaboration.

IV. CERTIFICATION AND ONLINE-ASSESSMENT PROCEDURE BY USING THE OPEN SOURCE LMS ILIAS

The word "certificating" originates from the Latin "certum facere" and means „to make something certain" or to "guarantee". To certificate somebody signifies that an independent, neutral third party assesses whether with a product, a service or by a person, the given criteria are

fulfilled. If that is the case, neutral third party confirms publicly the certification with a certificate. The application procedure is presented in the Fig. 6.

Generally everyone who is interesting be assessed may take part if he/she can furnish a proof in dealing with the product EPLAN Electric P8. The proof can be furnished e.g. with the visiting of the EPLAN courses, or with application and use the product in the company. Alternatively examinees have the possibility to visit the preparation courses at the EPLAN company [9]. Application to assessment is carried out online and is accessible via URL: www.eplan.rfh-koeln.de. All necessary information about the exam dates, location etc. are

to be found at this website. The assessment consists of the practical and the theoretical part. Practical part occurs on location selected during the application. For the practical part, RFH nominates licensed examiner who has the tasks to observe the task. All results are to be forwarded to the RFH which has the final authority to decide whether the assessment is passed or not.

ILIAS is worldwide used application, with the large spectrum of the features. The ECE assessment website is accessible via URL: www.ece.rfh-koeln.de. Fig. 8 shows the log-in mask.

The log-in data are automatically generated and delivered to the customer over email for the case that the assessment fees are paid. The application website is a SSL secured site in accordance with the data privacy regulations and terms, which are valid for the Federal Republic of Germany.

Fig. 6. Modalities of ECE certification.

Fig. 7. ECE assessment registration.

V. APPLICATION EXAMPLES

So called direct editing function lets the user edit texts (e.g. device tags, function text or part numbers) with an effortless click of the mouse in the circuit diagram. Without having to edit the device dialog box, all information can be
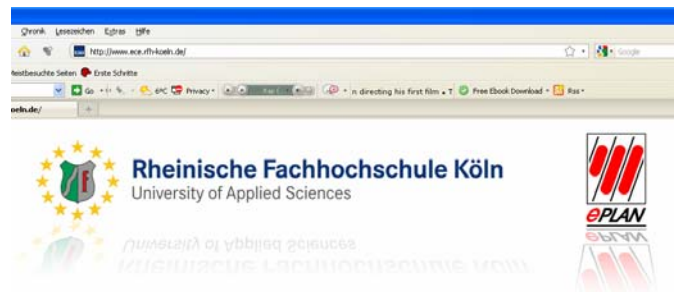
Fig. 8. ECE assessment log-in.
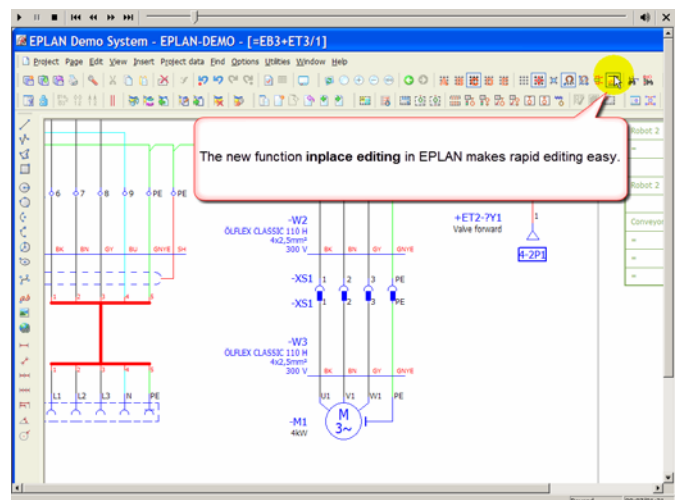
Fig. 9. Inplace editing function.
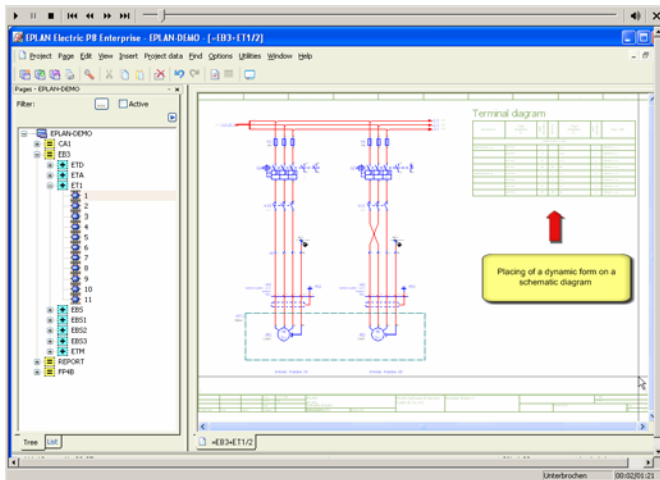
Fig. 10. Dynamic reports functions.

spontaneously edited in the circuit diagram directly where it is displayed. Following figure presents the inplace editing function.

Dynamic reports functions are assigned to schematic views and individual reports are combined on one report page.

PLC multifunctional terminals allow the flexible use of the Input and Output terminals of the PLC enabling the use of the same terminal for different function. In the example in Fig. 11 and 12, for the case of the substitution of the thermo-elements which are connected with PLC system over 2-wire technique, with potentiometers which are connected with PLC system over 4-wire technique it is possible, without to change lay-out to carry out new numbering of the terminals also by using the numbering scheme of the different manufacturer.

So, in the picture above is presented numbering scheme by PILZ and the picture below by Siemens.

VI. CONCLUSION

This paper has provided the applicational and conceptual insights in the most used CAE software for electrical engineering and project planning in the European industry, motives, conceptualization and design of the successful university-industry cooperation in the area of the Third Party Certification by using the open source LMS application. The evaluation of the key success factors for such cooperation has indicated, that the optimal technical solution adjusted to the customer needs, deliberate interface management between the university and company, as well as the mutual respect are decisive for the long-term success of the cooperation. Note: Further information can any time be requested from the author. Please use authors electronic mail address for the request.

Fig. 11. PLC connected thermo-elements in 2-wire technique.
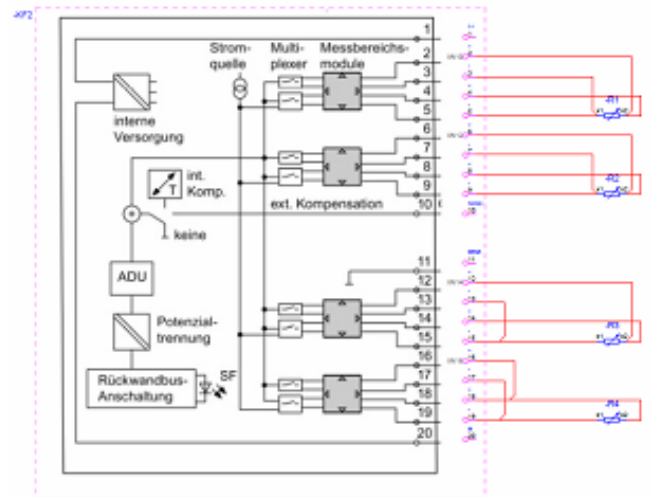
Fig. 12. PLC connected potetiometers in 4-wire technique.

REFERENCES

[1] Valentin,M and Maria, E (2000) "University-Industry Cooperation: A Framework of Benefits and Obstacles", Industry & Higher Education, v14 n3 p165-72 Jun 2000

[2] Kotler, Peter: Marketing Management, Analysis, Planning, Implementation and Control. - 8th ed. - Sydney: Prentice Hall, 1994

[3] Feng-Shang Wu (1994) "The Cultural Impact of University-Industry Research Cooperation: the American Experiences," Sino-South Africa Bilateral Symposium, Taipei, Taiwan.

[4] Schein, EH (1996) Organizational Culture and Leadership (Jossey-Bass Psychology Series), Jossey-Bass; 2 edition (December 5, 1996)

[5] Sendler, U. Das PLM-Kompendium - Referenzbuch des Produkt-Lebenszyklus-Managements,EPLAN Software & Service,Springer Berlin Heidelberg,August 2009, pp.163-174

[6] OICA (2002), Daten zur Automobilwirtschaft (Data to the automobile economy), Avaliable <http://www.oica.net/, February 2010, 11:55h

[7] Montgomery,C.A., and M. E. Porter, eds. Strategy: Seeking and Securing Competitive Advantage. Boston, Mass.: Harvard Business School Press, 1991.

[8] Eplan, EPLAN Certified Engineers, Available: http://www.eplan.de/services/training/zertifizierung/eplan-certified-engineer.html?L=1%20-%2096 k, February 2010.

[9] Eplan, EPLAN Electric P8 ECE Vorbereitungstraining (preparatory course), Available: http://www.eplan.de/services/training/direktbuchung.html?no_cache=1&L=1%20-%2096k&seminarId=110340&region=, February 2010.

[10] ILIAS "ILIAS 4 e-Learning" Available: http://www.ilias.de/docu/, February 2010.

A Model of the Molecular Rectifying Diode Type Aviram-Ratner

Dalibor Sekulić and Miloš Živanov

Abstract—**Due to the huge power consumption and expensive fabrication methods required, down scaling silicon devices to sub-100 nm dimensions is becoming very unattractive. On the other hand, it is easier to build electronic circuits using molecules since they are small and their properties can be tuned. The molecular rectifying diodes are made of two metallic electrodes connected by a molecule, which contains acceptor and donor subunits, separated by insulating bridge. Both subunits are modeled as quantum dots with discrete energy levels, isolated from each other by potential barrier and weakly coupled to both electrodes through tunnel junctions. Analytic formula for the current is found in the case of the Aviram-Ratner ansatz of rectification and current-voltage characteristic is obtained. It is shown that rectification current depends on the position of the acceptor's LUMO and donor's HOMO levels with respect to the Fermi energy of the electrodes before bias is applied, and their shift due to the bias voltage.**

Index Terms—**Molecular diode, Current-voltage characteristic, LUMO, HOMO, Fermi energy.**

I. INTRODUCTION

MOLECULAR electronics involves using molecules as replacements for conventional devices and interconnects. Conventionally, electronics has scaled as per Moore's law viz. there has been a doubling of devices per chip every 18-24 months. However, there are potential roadblocks in the near future arising from both monetary and physical constraints. A current fabrication line costs $2.5 billion to construct, and the cost is projected to rise above $200 billion by year 2015 – a main reason why many semiconductor firms prefer to go "fabless".

The fast paced developments in the field of semiconductor technology in the recent past have proved without doubt that the efforts to miniaturize the transistors will reach the physical limits earlier than anticipated due to the laws of quantum mechanics and limitations of fabrication methods [1]. Scaling down silicon devices to sub 100 nm and packing millions of them in a chip will not be an attractive idea as these systems consume huge power and will become very expensive to fabricate. Therefore, we need to look beyond silicon to make ultra-high density electronic systems and it is important that

D. Sekulić and M. Živanov are with the Faculty of Technical Sciences, University of Novi Sad, Novi Sad, Serbia (e-mail: dalsek@yahoo.com and zivanov@uns.ac.rs).

alternate methods such as using molecules to make devices at the nanoscale are explored and exploited [2].

Silicon devices operate based on the movement of a large number of electrons n bulk matter while molecular devices take advantage of the quantum mechanical effects taking place at the nanometer scale. The building blocks of molecular electronics are single or small packets of molecules. While efforts are on to replace the conventional wires and semiconductor devices with molecules, what would be desirable is to build molecular architectures with addressable electronic properties [3]. The main advantage of molecular electronics is the lower cost, compatibility with flexible substrates and simpler packaging when compared to the conventional inorganic electronics.

Since molecules are small, their functionality can be tuned because of their special properties. Either synthesis or self-assembly processes can be used to manipulate the molecules. The most important molecular backbones are: 1) polyphenylene-based chains and 2) carbon nanotubes. Unlike in the case of silicon technology, the bottom-upapproach of manipulating molecules is expected to be not only cheap but also will result in higher speeds of information processing with less power. Making electronic rectifiers using molecules was first proposed by Aviram and Ratner [4]. There are two types of molecular diodes: rectifying diodes and resonant tunneling diodes which can both be used in realizing monomolecular digital logic circuits [5]. In addition, we also need molecular wires [6] to connect the molecular devices into a complex circuit with specific applications [2].

II. MOLECULAR RECTIFYING DIODE

A diode or a rectifier, which conducts only in one direction, is the building block of any three terminal semiconductor electronic devices such as a bipolar transistor or a field effect transistor. Diode based logic circuits using AND/OR gates are well known for building logic families by using the rectifying diodes at the input and connecting a resistor between the supply or the ground. A molecular diode too contains two terminals and functions like a semiconductor pn junction and has electronic states which can be clearly distinguished between highly conductive state (ON) and less conductive state (OFF).

The seminal work of Aviram and Ratner in 1974 led to several experimental attempts to build molecular diodes

Aviram and Ratner have suggested that electron donating constituents make conjugated molecular groups having a large electron density (N-type) and electron withdrawing constituents make conjugated molecular groups poor in electron density (P-type). According to them, a noncentrosymmetric molecule having appropriate donor and acceptor moieties linked with an σ-bridge and connected with suitable electrodes will conduct current only in one direction-acting as a rectifier. They showed that in this D-σ-A molecule, the lowest unoccupied molecular orbital (LUMO) and highest occupied molecular orbital (HOMO) can be aligned in such a way that electronic conduction is possible only in one direction making it function like a molecular diode. Asymmetric current-voltage characteristics for an σ- bridged system were first reported in 1990 [7].

The structure of the mono-molecular diode is shown in Fig. 1. This diode is based on a molecular conducting wire consisting of two identical sections (S1, S2) separated by an insulating group R. Section S1 is doped by at least one electron donating group (X e.g. -NH2, -OH, -CH3, -CH2CH3) and section S2 is doped by at least one electron withdrawing group (Y e.g. -NO2, -CN, -CHO). The insulating group R (such as -CH2 -, -CH2CH2-) can be incorporated into the molecular wire by bonding a saturated aliphatic group (no pi-orbitals). To adjust the voltage drop across R, multiple donor/acceptor sites can be incorporated. The single molecule ends are connected to the contact electrodes e.g. gold.
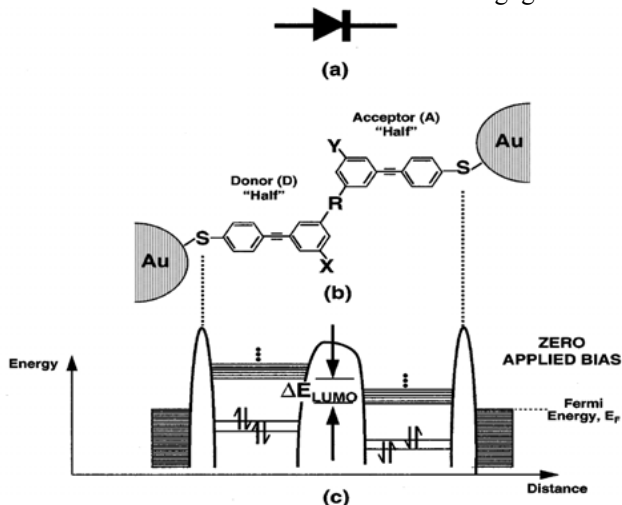

Fig. 1. Equilibrium state of the molecular rectifier.

The band diagram of the mono-molecular diode under zero-bias conditions is shown in Fig. 1. We notice that there are three potential barriers: one corresponding to the insulating group (middle barrier) and two corresponding to the contact between the molecule and the electrode (left and right barriers). These potential barriers provide the required isolation between various parts of the structure. The occupied energy levels in the metal contacts and the Fermi energy level EF are also shown. On the left of the central barrier all the pi-type energy levels (HOMO as well as LUMO) are elevated due to the presence of the electron donating group X and similarly on the right of the central barrier the energy levels

are lowered due to the presence of the electron withdrawing group Y. This causes a built-in potential to develop across the barrier represented by the energy difference ΔELUMO. For current to flow electrons must overcome the potential barrier from electron acceptor doped section (S2) to electron donor doped section (S1) and this forms the basis for the formation of the mono-molecular rectifying diode. The energy band diagram under forward bias conditions (left hand contact at higher potential than the right hand contact) is shown in Fig. 2.a. Here, electrons are induced to flow by tunneling through the three potential barriers from right to left causing a forward current flow from left to right.

The band diagram under reverse bias conditions (left hand contact at lower potential than the right hand contact) is shown in Fig. 2.b. As a result, electrons from the left contact would try to flow towards the right contact which is at a higher potential. However, conduction is not possible because the there is still an energy difference between the Fermi energy EF of the left contact and the LUMO energy of the electron donor doped section. It is assumed that both the applied forward and reverse bias potentials are identical. For a higher reverse bias, however, it is possible for the Fermi energy EF of the left contact to come in resonance with the LUMO energy of the electron donor doped section causing a large current to flow in reverse direction and this is akin to the breakdown condition in a diode.
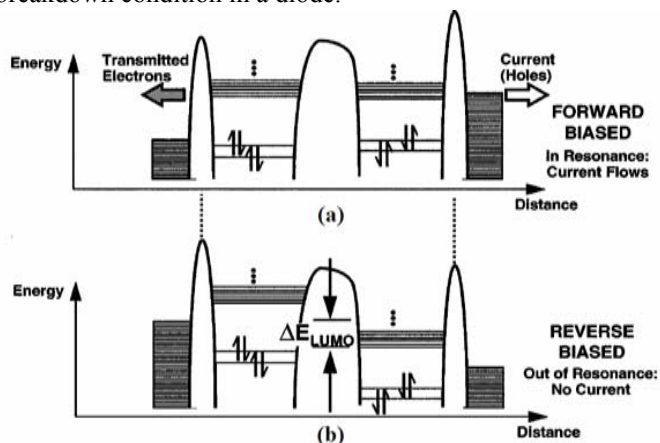
Fig. 2. Rectifier operation under (a) Forward bias (b) Reverse bias.

III. CURRENT FORMULA

Here we assume that the electronic states of particular segments of the molecule (donor and acceptor parts) are perfectly isolated from each other (no hybridization) due to insulating spacer (bridge). Since only HOMO and LUMO levels are the most important in the transport description, we focus our attention on the mentioned energy levels only. General formula for the current flowing through the device can be written as follows:

$$I(V) = I_0 \int_{-\infty}^{\infty} d\varepsilon' \int_{-\infty}^{\infty} d\varepsilon \, f(\varepsilon, \mu_1) \zeta(\varepsilon - \varepsilon_L^A)[1 - f(\varepsilon', \mu_2)]\zeta(\varepsilon' - \varepsilon_H^D)$$

$$- I_0 \int_{-\infty}^{\infty} d\varepsilon' \int_{-\infty}^{\infty} d\varepsilon \, f(\varepsilon, \mu_2) \zeta(\varepsilon - \varepsilon_L^D)[1 - f(\varepsilon', \mu_1)]\zeta(\varepsilon' - \varepsilon_H^A). \tag{1}$$

In the above double-integration procedure: $f(\varepsilon,\mu_{1/2})$ is the equilibrium Fermi distribution function:

$$f(\varepsilon, \mu_{1/2}) = \left(1 + e^{\frac{\varepsilon - \mu_{1/2}}{k_B T}}\right)^{-1}, \qquad (2)$$

and $\zeta(\varepsilon\text{-}\varepsilon^{A/D})$ is the so-called broadening function of molecular energy level, which is assumed to be of Lorentzian shape:

$$\zeta(\varepsilon - \varepsilon^{A/D}) = \frac{1}{2\pi} \frac{\Gamma_{1/2}}{(\varepsilon - \varepsilon^{A/D})^2 + \frac{1}{4}\Gamma_{1/2}^2}. \qquad (3)$$

The strength of the coupling between the molecule and the metallic electrodes (due to the thiol linkages) is described by widths parameters Γ_1 and Γ_2, which are assumed to be energy and voltage independent [8]. Both electrodes are treated as semi-infinite reservoirs of free electrons at thermal equilibrium, which are characterized through the electrochemical potentials: $\mu_{1/2} = E_F \pm eV/2$.

Furthermore, the magnitude of the current flowing through the device is proportional to a prefactor I_0, which takes into account the transfer rate between acceptor and donor subunits (multiplied by an elementary electronic charge e):

$$I_0 = \frac{e}{\tau_s} e^{-\beta R_{DA}}. \qquad (4)$$

Here: β is a structure-dependent attenuation factor, R_{DA} is the distance between donor and acceptor species (the length of a bridge) and τ_S is donor-acceptor tunneling time. Such time τ_S is approximately equal to experimentally-determined time involved in bridge vibrations and generally can be temperature-dependent. When donor and acceptor subsystems are weakly coupled with the help of σ-bonded bridge, the electron transfer takes place directly from donor to acceptor via tunneling process (also referred to as superexchange mechanism) and exhibits exponential decay as a function of distance [9].

Instead of superexchange theory, it is also possible to describe intervalence donoracceptor tunneling process with the help of Marcus theory [10]. In this case of a classical description of the transfer rate, the expression for prefactor I_0 is given by [11]:

$$I_0 = e\frac{k_B T}{h} e^{-\frac{\Delta G^*}{k_B T}}, \qquad (5)$$

where: k_B is Boltzmann constant, T is absolute temperature and ΔG^* is the activation free energy associated with donor-acceptor electron transfer reaction. However, both approaches indicate that the reduction of the current is caused mainly by some exponential factor.

IV. An Example

The possibility of utilization of DNA molecules as the building elements for molecular electronics has been largely discussed in recent years and many controversial reports of the conducting behavior of DNA exist in the current literature. According to different experimental studies and theoretical models, the DNA molecule can be an insulator, wide-gap semiconductor, semimetal, or conductor.

Now we proceed to apply presented formalism to the case of proposed model of molecular diode (shown in Fig.3). The scheme of an electric circuit where an adenine-thymine (methyl-adenine methyl-thymine) DNA base pair is chemically bound to the Au (111) model contacts is shown in Figure 3. The terminal hydrogen atoms of the base pair were removed or have been replaced by sulfur atoms as displayed in Figure 3 to compare directly our results with the data for the benzene-1, 4-dithiolate (BDT) molecule. BDT was one of the first structures proposed as the molecular wire for which both experimental and theoretical [12] current-voltage dependencies are known. The substitution of terminal hydrogen atoms is also useful to facilitate bonding of the A–T base pair to the gold surface because it is known that the sulfur atoms create strong covalent bonds with the Au (111) surface in the tetrahedral position, where the distance to the nearest gold atoms is 2.53 Å [13].

Fig. 3. Scheme of the DNA base pair attached to the Au (111) contacts.

In general, the electronic structure of molecular systems can be calculated by various techniques, including: empirical, semiempirical, ab initio or density functional approaches, which are based on different degrees of approximation. Hence, energy levels for both subsystems are (given in eV): $\varepsilon_H^D = -11.2$, $\varepsilon_L^D = -8.6$, $\varepsilon_H^A = -12.4$ and $\varepsilon_L^A = -10.6$. Since the voltage is dropped entirely at the tunnel barriers, the energies of the molecular states depend on the applied bias through the relations: $\varepsilon_A = \varepsilon - eV/2$, $\varepsilon_D = \varepsilon + eV/2$. For saturated hydrocarbon chains β=0.9 Å^{-1} [14], the length of the bridge is R_{DA}=1.99Å and molecular vibration period for that bridge is of order of $\tau_S \sim 10^{-12}$s [15]. Fermi energy of the electrodes is usually located somewhere in between the HOMO-LUMO gap [16], and in this work it is arbitrarily chosen to be equal to E_F=-10.9eV. To simulate bad contacts with the electrodes (as a typical situation in experiments) we take the parameters responsible for that coupling as: $\Gamma_1 = \Gamma_2$=0.02 eV.

Fig. 4. shows the current-voltage (I-V) and conductance-voltage (G-V) characteristics for molecular diode proposed in

this section (depicted in Fig. 3.) at temperature T = 290 K. Such type of molecular junction rectifies current in the forward direction (positively biased) relatively to that the reverse direction (negatively biased). Asymmetry of the I-V dependence is due to asymmetry in the structure of the molecule itself. Substituting all the parameters indicated in the previous paragraph, an estimation of the current in the usual units is: $I_0 \approx 6$ nA. In order to obtain the same result from Marcus theory we should assume that: $\Delta G^* = 0.16$ eV. Character of the I-V curve and the evaluation of the peak value of the current are similar to some experimental results [12].
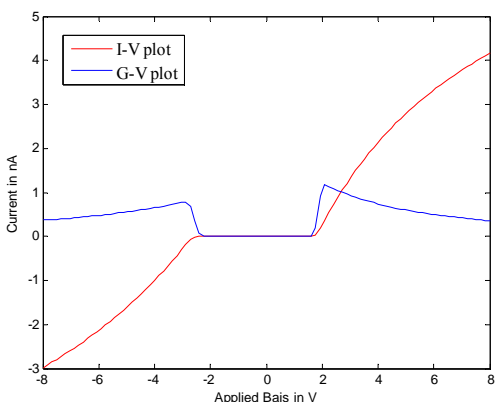
Fig. 4. The I-V and G-V characteristics for analyzed model of molecular rectifiinng diode type Aviram-Ratner.

V. CONCLUSION

Presented model qualitatively reproduces the rectifier behavior of complex molecular devices. The magnitude of the predicted current is comparable with experimental data in the conditions that we match all the parameters. So rectification is attributed to asymmetry of a molecule with an acceptor-bridge-donor structure (A-σ-D), where mechanism of diode-like behavior results from the Aviram-Ratner ansatz. However, this model seems to be useful as a simple theoretical tool in designing molecular devices of the donor-bridge-acceptor type, which demonstrate rectifying features. One of crucial problems stems from the task of finding Fermi energy of the electrodes (while experimental control of this level is realizable through the choice of metal, which play the role of the electrode).

Moreover, the tunneling of an electron through the acceptor-bridge-donor junction is treated as a sequential process, in which the molecular species are successively charged and discharged. In fact, after the initial tunneling step an electron can have enough time to redistribute charge along the molecule (i.e. to polarize this molecule). Such phenomenon can have an influence on the shifts of molecular energy levels, and transfer-induced dipole momentum can affect transport characteristics. However, here we do not include this effect into our formalism, completely ignoring such phenomena like Coulomb blockade. In the frames of this work we also neglected all the effects of electron correlations as well as inelastic scattering.

It should be also noted that several experiments on symmetric

molecules have shown rectification, while others have found very little or no rectification. Such effect is justified by asymmetric electrode coupling, which can result in an asymmetric potential drop along the length of the molecule. If the potential profile is asymmetric, molecular energy level through which an electron is propagated can line up differently in positive and negative bias, resulting in rectification. Rectifying features of molecular systems can also be explained as a consequence of conformational changes due to: thermal effects, inelastic tunneling or application of electric field.

REFERENCES

[1] G. D. Goldhaber, M. S. Montemerlo, J. C. Love, G. J. Opiteck and J. C. Ellenbogen, "Overview of nanoelectronic devices", Proc IEEE, pp. 521-540, 1997.

[2] J. M. Tour, M. Kozaki and J. M. Seminario, "Molecular Scale Electronics: A Synthetic/Computational Approach to Digital Computing", J Am Chem Soc, pp. 8486-8493, 1998.

[3] J. R. Heath and M. A. Ratner, "Molecular electronics", Phys Tod, pp. 43-49, 2003.

[4] A. Aviram and M. A. Ratner, "Molecular Rectfiers", Chem Phys Lett, pp. 277-283, 1974.

[5] D. Sekulic and M. Sataric, "Molecular Diodes and Diode Logic Molecular Gates", INFOTEH-Jahorina, Vol. 8, Ref. E-I-3, pp. 356-360, March 2009.

[6] R. J. Magyar, S. Tretiak, Y. Gao, H. L. Wang and A. P. Shreve, "A joint theoretical and experimental study of phenylene-acetylene molecular wires", Chem Phys Lett, pp. 149-156, 2005.

[7] N. J. Geddes, J. R. Sambles, D. J. Jarvis, W. G. Parker and D. J. Sandman, "Fabrication and investigation of asymmetric current-voltage characteristics of a metal langmuir-blodgett monolayer metal structure", Appl Phys Lett, pp. 1916-1918, 1990.

[8] T. Kostyrko, B. Bułka, "Current fluctuations of polymeric chains", Phys. Rev. B, Vol. 67, 2555-2561, 2003.

[9] W. B. Davis, W. A. Svec, M. A. Ratner and M. R. Wasielewski, "Molecular-wire behaviour in p-phenylenevinylene oligomers", Nature, Vol. 396, pp. 60-63, 1998.

[10] R. A. Marcus, Chem. Phys. Lett., Vol. 133, pp. 471, 1987.

[11] K. V. Mikkelsen, M. A. Ratner, "Molecular Electronics", Chem. Rev, Vol. 81, pp. 113, 1987.

[12] M. Di Ventra, S. T. Pantelides and N. D. Lang, "First-Principles Calculation of Transport Properties of a Molecular Device", Phys. Rev. Lett., Vol. 84, pp. 979-982, 2000.

[13] A.I. Yanson, G. Rubio Bollinger, H.E. van den Brom, N. Agraït and J.M. van Ruitenbeek, "Formation and manipulation of a metallic wire of single gold atoms", Nature, Vol. 395, pp. 783, 1998.

[14] H. Oevering, M. N. Paddon-Row, M. Heppener, A. M. Oliver, E. Cotsaris, J. W. Verhoeven and N. S. Hush, "Long-range photoinduced through-bond electron transfer and radiative recombination via rigid nonconjugated bridges: distance and solvent dependence", J. Am. Chem. Soc., Vol. 109, pp. 3258-3269, 1987.

[15] M. Olson, Y. Mao, T. Windus, M. Kemp, M. Ratner, N. Léon and V. Mujica," A Conformational Study of the Influence of Vibrations on Conduction in Molecular Wires", J. Phys. Chem. B, Vol. 102, pp. 941-947, 1998.

[16] P. S. Damle, A. W. Ghosh and S. Datta, "Molecular Electronics: Theory and Device Prospects", Phys. Rev. B, Vol. 64, pp. 6-14, 2001.

[17] R. M. Metzger, "Electrical Rectification by a Molecule: The Advent of Unimolecular Electronic Devices", Acc. Chem. Res., Vol. 32, pp. 950-957, 1999.

A New Real Differentiator with Low-Pass Filter in Control Loop

Čedomir Milosavljević, Branislava Peruničić, and Boban Veselić

Abstract—**The paper offers a new real differentiator realized as a closed loop system with a low-pass filter (LPF) within the control loop. The cascade of the LPF, with a considerable time constant, and an integrator is treated as the controlled object. The controller is of derivative (D) type with a limiter and a high gain. The closed loop time constant of the obtained real differentiator is small. The limiter and the LPF significantly attenuate noises. Simulation comparison between the proposed differentiator and the known differentiators reveals certain advantages of the proposed solution under appropriate conditions.**

Index Terms—**Derivative estimator, Real differentiator, Sliding mode based differentiator.**

I. INTRODUCTION

ESTIMATION of a real signal derivative is a well known and widely studied technical problem [1]-[9]. There are many approaches for a signal derivative estimation. The two main methods may be pointed out:

　1. Model-based method;
　2. Model-free method.

In the first method, the model of the process that generates the signal whose derivative is required is known. Typical model-free differentiators are (*i*) Euler's differentiator, (*ii*) real differentiator and (*iii*) sliding mode based differentiator [1]-[7].

As well known, Euler's differentiator is given by relation

$$\tilde{\dot{f}}(t) = T^{-1}[f(kT) - f((k-1)T)] . \tag{1}$$

If $T \to 0$, $\tilde{\dot{f}} \to \dot{f}$ by definition.

Unfortunately, if the input signal is noisy, the obtained differentiator's output will be contaminated as well. The amplitude of the input noise's derivative will be amplified if $T < 1$. Consequently Euler's differentiator is not recommended for a wide industrial application.

Consider an illustrative example [2] with an input signal

$$f(t) = \sin(\pi t), t \in [0,2], T = 0.005\text{s}. \tag{2}$$

Fig. 1 shows the differentiation outputs of (*a*) noise-free input and (*b*) input contaminated with an uniform random noise having an amplitude of 0.004. It is obvious from the Fig. 1*b* that the Euler's differentiator cannot be used when the input is significantly contaminated by noises.

A real differentiator, defined by its transfer function as

$$\tilde{f}(s)/f(s) = s/(1+\tau s) , \tag{3}$$

where τ - is a time constant, is recommended for industrial applications. This differentiator has a low pass filter (LPF) $(1/(1+\tau s))$. Its role is to attenuate high-frequency noises. Theoretically, in the noise-free case an accurate estimation can be obtained by choosing a small τ, Fig. 1*a*. However, in real systems with noisy inputs the constant τ must have a higher value which increases the phase lag. These contradictory requirements can be handled only by a adopting a compromise between the allowed level of the noise amplitude in the output signal and the phase lag.
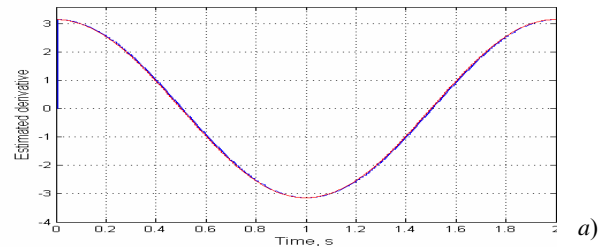
Fig. 1.a. Derivative of signal (2): a) noise-free case.
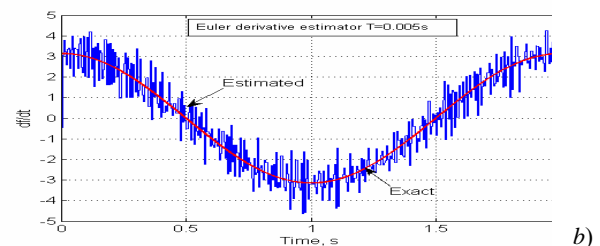
Fig. 1.b. Derivative of signal (2): b) Euler's differentiator noise case.

　Č. Milosavljević is with the Faculty of Electrical Engineering, University of East Sarajevo, East Sarajevo, Bosnia and Herzegovina. cedomir.milosavljevic@elfak.ni.ac.rs.

　B. Peruničić is with the Faculty of Electrical Engineering, University of Sarajevo, Sarajevo, Bosnia and Herzegovina. brana_p@hotmail.com.

　B. Veselić is with the Faculty of Electronic Engineering, University of Niš, Niš, Serbia. boban.veselic@elfak.ni.ac.rs.
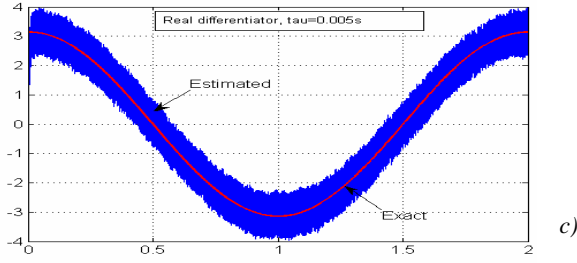
Fig. 1.c. Derivative of signal (2): a) noise-free case; b) Euler's differentiator noise case; c) Conventional real differenctiator noise case. T=τ=0.005s.

The real differentiator (3) is designed as an active control structure, Fig. 2. Derivative estimation of signal (2) using real differentiator with τ=0.005s, in the noise contaminated case, is given in Fig. 1c.
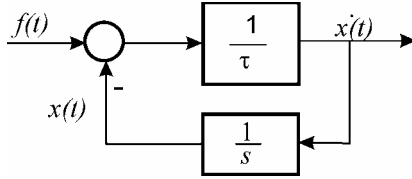
Fig. 2. Conventional real differentiator.

A particular problem arises when the input signal has low amplitude and/or a high noise/signal ratio. Then the estimated derivative cannot even be recognized.

As an example, let the input signal, $f(t) = 0.008\sin(\pi t)$, $t \in [0,2]$, be contaminated with the same noise as above. The output in this case is given in Fig. 3.
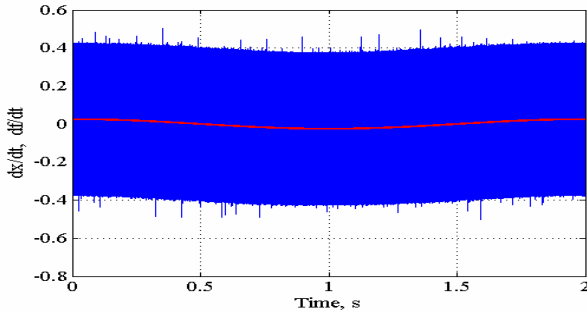
Fig. 3. Derivative estimation of signal $f(t) = 0.008\sin(\pi t)$, noisy-case, τ=0.005 s.

It is clear that these derivative estimators cannot be used for wide range of applications. Pre-filtering or post-filtering significantly increases the phase lag so the estimated error will increase, also.

There are several solutions for the model-free derivative estimation. The focal part of this paper is sliding mode differentiators [1]-[7] explained in the Section 2. In the third section, a new real differentiator is proposed. It is realized as a conventional control loop. The controller is of the D-type and it has a high gain and saturation. An LPF between the controller and the output is introduced. Significant advantages of the proposed solution under certain conditions over differentiators [1] and [2] are demonstrated using simulations.

In the reminder of the paper the used noise parameters are identical to ones given above.

II. SLIDING MODE BASED DIFFERENTIATORS

Very high expectations have been set in application of sliding mode to obtain signal derivatives. The typical structure of these differentiators is given in Fig. 4. Their high-frequency switching nature requires introduction of an output LPF. Unfortunately, a LPF increases phase lag as well as estimation error.
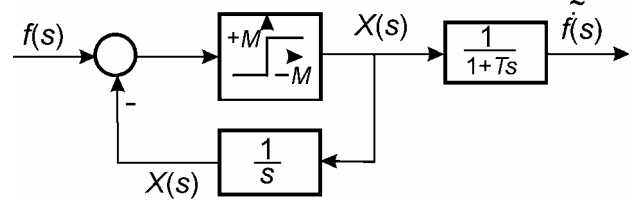

Fig. 4. Conventional sliding mode based differentiator.

Two sliding mode-based differentiators are of particular interest in this paper. The Levant's exact differentiation [1] is based on the second-order sliding mode approach. The differentiator proposed by Xu et all. [2], applies the closed loop filtering and uses the first-order sliding mode and the reaching law principle [10]. The next two subsections give essentials of these differentiators.

A. Levant's exact differentiator

Levant's differentiator, Fig. 5, is described by the following relations:

$$\dot{x}(t) = u(t), \tag{4a}$$

$$u = u_1 - \lambda \mid x(t) - f(t) \mid^{1/2} \operatorname{sgn}(x(t) - f(t)), \tag{4b}$$

$$\dot{u}_1 = -\alpha \operatorname{sgn}(x(t) - f(t)), \tag{4c}$$

where (4a) is differential equation of the "controlled object" – an integrator, and relations (4b) and (4c) describe second-order sliding mode controller. $f(t)$ is the input signal, whose derivative is estimated by control $u(t) = \dot{x}(t)$. α, λ>0 are gains whose values depend on the Lipchitz constant of the input signal $f(t)$. The main drawbacks of Levant's differentiator are the dependence of its parameters values of the input signal. To overcome this shortcoming an adaptive algorithm has been proposed in [4]. Another drawback is an overshoot at the beginning of the estimation.

As an example, Fig. 6 gives the output of the Levant's differentiator for the signal

$$f(t) = 5t + \sin(t) \rightarrow \dot{f}(t) = 5 + \cos(t); \lambda = 6; \alpha = 8, \tag{5}$$

where the parameters have been adopted from the original paper [1]. Runge-Kutta method with integration step of 10^{-4} s has been selected for the simulation.
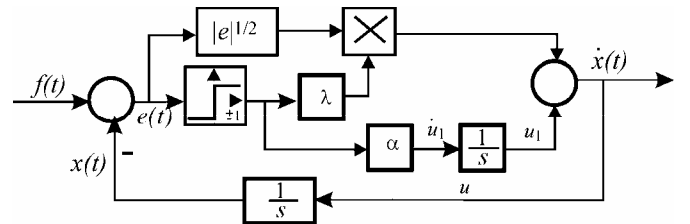
Fig. 5. Levant's exact differentiator.

Signal true differential and estimation obtained by Levant's differentiator for the noise-free case is given in Fig. 6a. The Fig 6b shows the estimation error. Its amplitude of 0.75 10⁻³ may be taken as an excellent result. The noises in Fig. 6b are consequence of quantization resolution of 1,1921e-007 they appear because a D/A converter is introduced in the simulation. However, Fig. 6c shows Levant's differentiator signal in the noise case. The noise in output signal is increased up to 0.4 (see Fig. 11a also). In such case, as was recommended in [1], it is necessary to use an additional LPF.
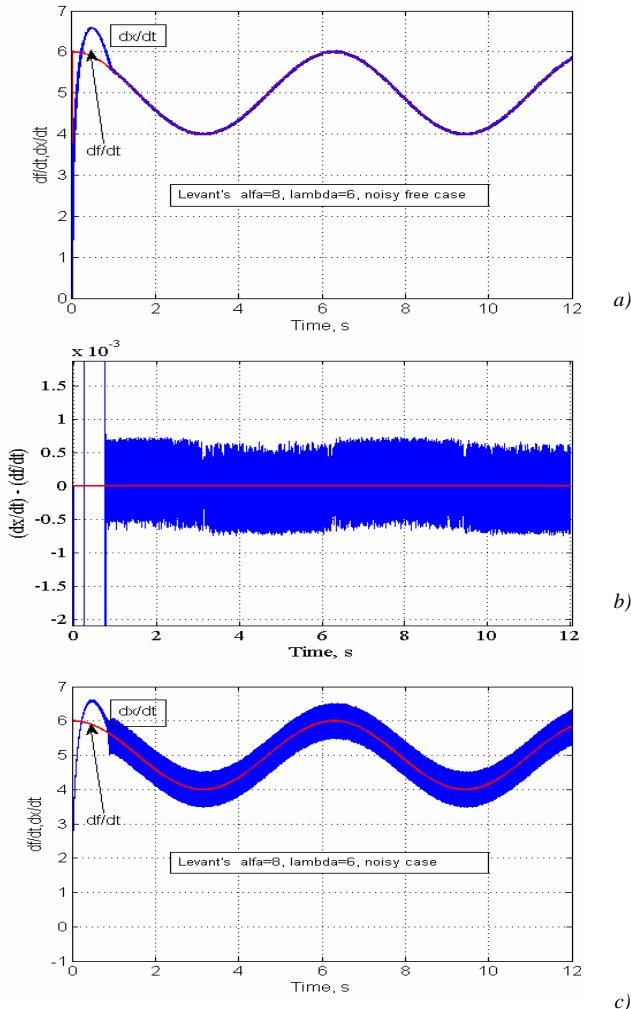
Fig. 6. Levant's differentiator: a) noise-free case; b) derivative estimation error for the noise-free case; c) contaminated case.

B. 2.2 Xu's et al. derivative estimator

This estimator is shown in Fig. 7.
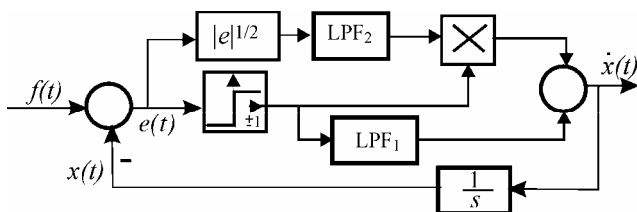
Fig. 7. Xu's et al derivative estimator [2].

Its main aims were to eliminate overshoot appearing in the Levant's differentiator and to minimize noise effects by inserting a LPF in the closed-loop. Under nominal conditions, i.e. with no noise, it provides soft reaching of the sliding hyper-surface.

As an example in [2], differentiation of the signal was given.

$$f(t) = \sin(50\pi t); \dot{f}(t) = 50\pi \cos(50\pi t) \qquad (6)$$

LPFs are described by the following transfer functions: LPF₁: 1000/(1+0.000055s); LPF₂: 1/(1+0.003s).

For Levant's differentiator and the signal (6) parameters α and λ are: 25000 and 180, respectively [2]. Simulation results of both estimators are given in Fig. 8a. Fig. 8b displays the expanded initial phase of estimation. The estimator of Xu et. Al. either does not have an overshoot at all, or a very small overshoot. The Levant's differentiator has a significant deviation from the exact derivative at the start of estimation.

Simulation for both differentiators with the same noisy input has similar outputs. Note very high signal amplitude, i.e. a very low noise/signal ratio. Also observe that the sign function in Xu's et al. estimator is replaced with saturation element.

For the higher noise/signal ratios, the estimator of Xu et al. gives a lower performance Fig. 9b, than the Levant's exact differentiator, Fig. 6c, for the same input signal (5). For a better estimation of the noisy signal derivative it is necessary to add one more LPF of Butterworth type [2] or to modify parameters in LPFs.

III.   A Novel Real Differentiator

In order to design derivative estimator that does no need parameters adjustment to the input signal $f(t)$ and to noise/signal ratio, a new simple structure is proposed in this paper, Fig. 10. This structure resembles the simple real differentiator structure from Fig. 2, but exhibits a more efficient noise filtration.

It is easy to deduce that, in the linear working regime, i.e. for small signals, the transfer function of the proposed differentiator is identical to the transfer function (3) with time constant $\tau = T/(1+K)$. For a higher gain K the system has a low phase distortion.

The noise in the input is significantly amplified by the block du/dt. Since the obtained signal passes through the limiter, the noise amplitude will be symmetrically saturated and thus averaged to zero. It is assumed that the usefulsignal's derivative stays in the linear zone of the limiter. The large time constant of the LPF averages noises, reducing significantly their impact on the output.

To verify the concept, the proposed differentiator and the Levant's differentiator have been tested with a variety of signals. The parameters of the proposed differentiator were: $K=10^5$, $T=10$ s, limiter saturation: ±10. Integration time in simulation is 10^{-4} s. MATLAB Simulink differentiator is used as du/dt element.

The differentiators have been firstly simulated with input signal defined by (5) in the presence of the above given noise.

For the Levant's differentiator parameters are chosen as suggested in [1]. Simulation results are in the Fig. 11.

a)

b)
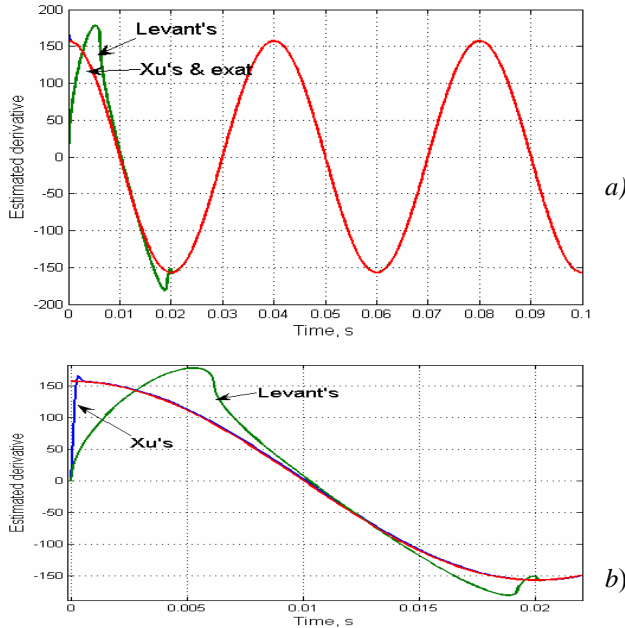
Fig. 8. Comparison of Levant's differentiator (α=25000, λ=180) and Xu's et al. derivative estimator.

a

b
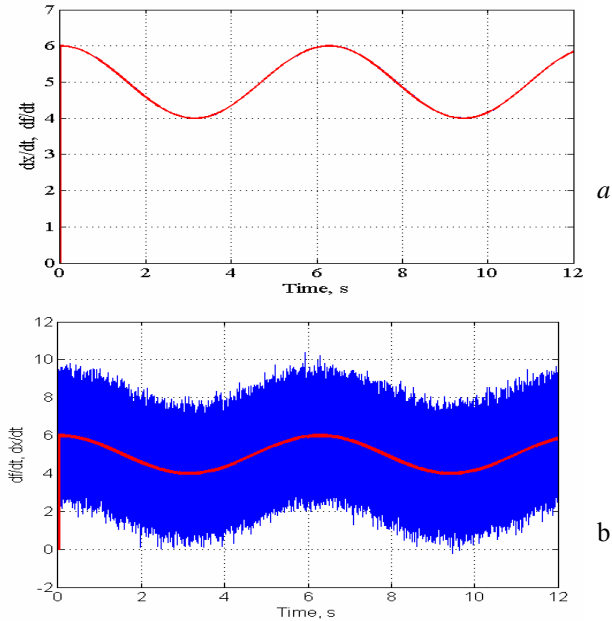
Fig.9. Xu's et al. derivative estimation for $f(t) = 5t + \sin(t)$ a) noise-free case; b) noisy case.
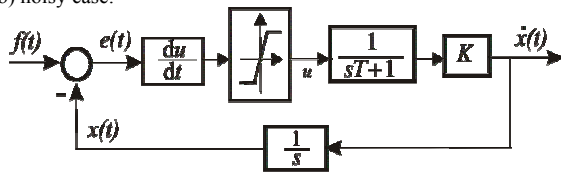
Fig. 10. Block-scheme of the proposed differentiator.

Fig. 11*a* displays the estimation error whose amplitude is near 0.4 for the Levant's differentiator. Response of the proposed differentiator depicted in Fig. 11*b*, indicates a shorter rise time and no overshoot in the response. Fig. 11*c* gives the estimation error of the proposed differentiator in the

presence of noise. Comparing the results from Fig. 11*a* and 6*b* it can be deduced that the Levant's differentiator has noise in the output even for a noise-free input. The amplitude of this noise is higher then the amplitude of the noises in the output of the proposed differentiator with a noisy input.

a)

b)

c)
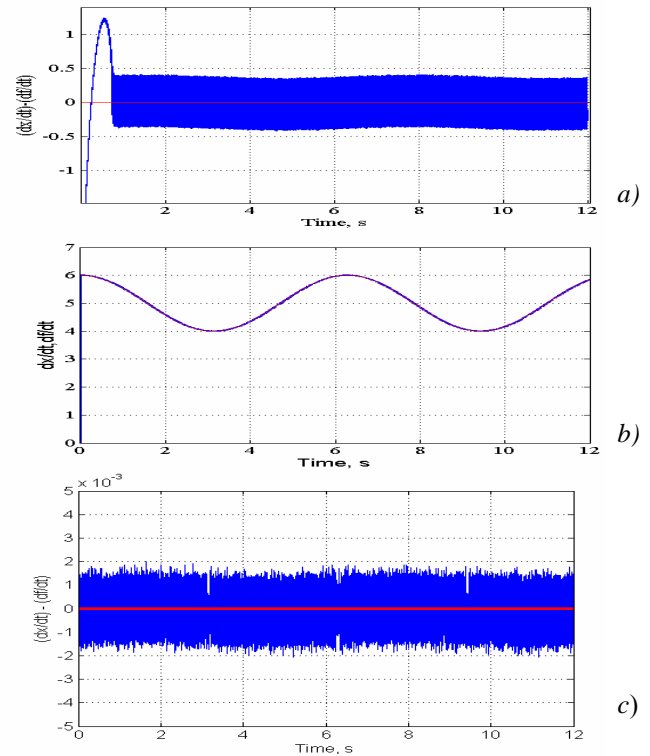
Fig. 11.   Responses of differentiators for the signal (5), noise case: a) estimated error of Levant's differentiator; b) and c) response and estimated error of the proposed differentiator, respectively.

a)
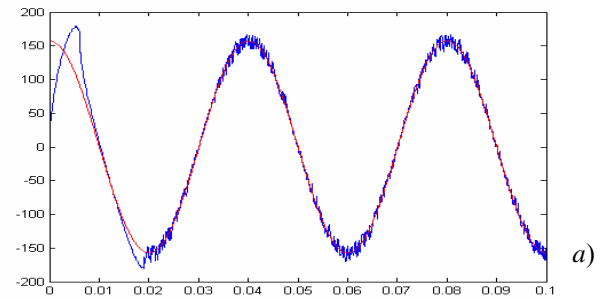
Fig. 12.a. Responses of differentiators for the signal $f(t) = \sin(50\pi t)$ in the noisy case. a) Levant's differentiator.

b)
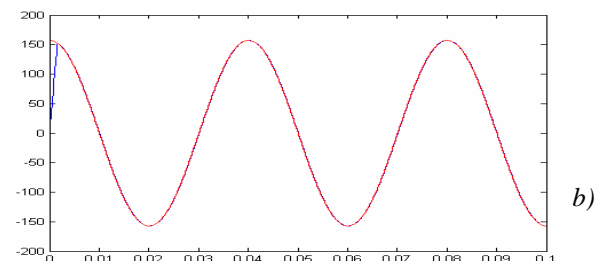
Fig. 12.b. Responses of differentiators for the signal $f(t) = \sin(50\pi t)$ in the noisy case. b) the proposed differentiator.
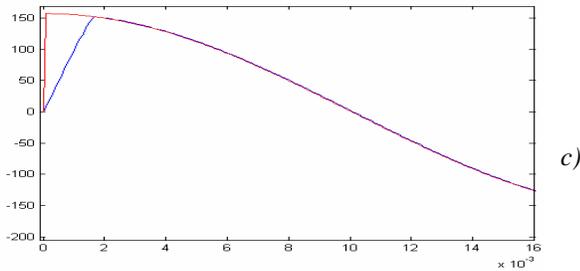
Fig. 12c. Responses of differentiators for the signal $f(t) = \sin(50\pi t)$ in the noisy case. c) Starting part of the response from Fig. 12.b (zoomed).
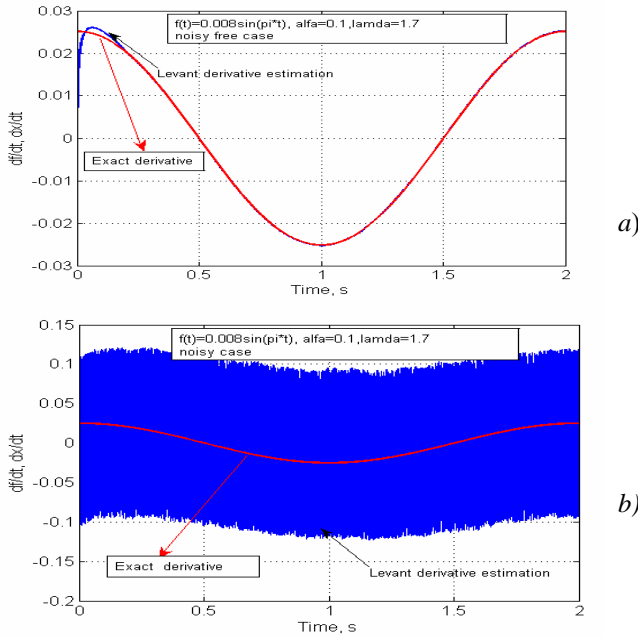
Fig. 13.a,b. Responses of differentiators for $f(t) = 0.008\sin(\pi t)$: a) and b) Levant's differentiator.
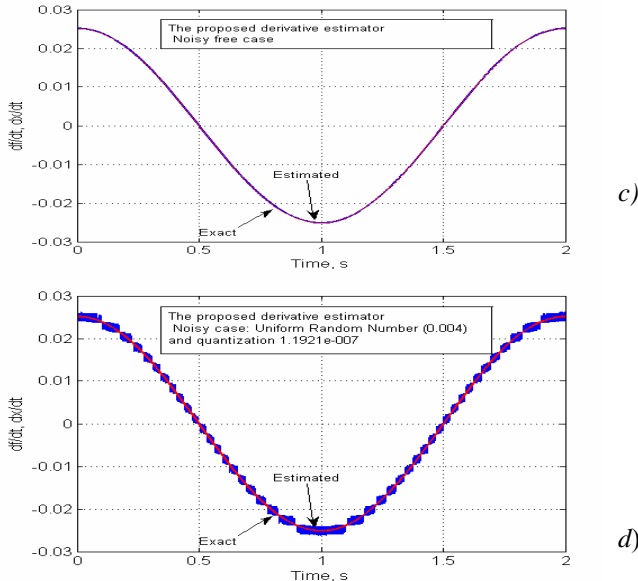
Fig. 13.c,d. Responses of differentiators for $f(t) = 0.008\sin(\pi t)$: c) and d) the proposed differentiator, noise-free and noise case respectively.

The second example is a differentiation of the signal (6) polluted with noise. Levant's differentiator parameters are chosen as in Fig. 8. The results are given in Fig. 12. Fig. 12a shows results of Levant's differentiator while the response of the proposed differentiator is given in Fig. 12b. Fig. 12c displays starting phase of the proposed derivative estimator. It is apparent that there are no overshoots.

In the next example a low amplitude signal $f(t) = 0.008\sin(\pi t)$ is used, with and without noise. The following parameters are chosen for the Levant's differentiator: α=0.1; λ=1.7. Parameters of the proposed differentiator are not changed. Simulation results are given in Fig. 13. Fig. 13a and 13b display the response of the Levant's differentiator, for a noise-free and a noisy input respectively. Figure 13c and 13d show outputs of the proposed differentiator to the same signals.

Given simulation results indicate that the proposed differentiator has considerable better characteristics then Levant's differentiator except in one case. Namely, in Fig. 13d the resolution of D/A converter has the same consequence as a noise of step type in the output signal of the proposed differentiator. The analysis of simulation point out that the proposed differentiator requires a D/A converter resolution better then 24 bits. For the given study the resolution of 32 bits has been applied.

Operation of the Levant's and the proposed differentiator is given in Fig. 14 and Fig. 15 in the noisy case for the indicated signals, without any additional comments. Parameters of Levant's differentiator are specified in the figures, while parameters of the proposed differentiator are again unchanged.
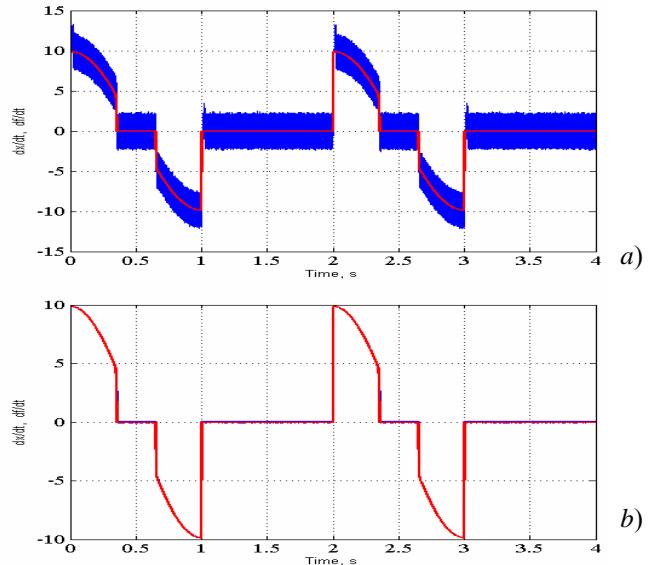
Fig. 14. Responses of differentiators for $f(t) = \pi \sin(\pi t)$ whose amplitude is saturated at ±2.8, in the noisy case: a) Levant's differentiator $\alpha = 500, \lambda = 35$; b) the proposed differentiator.

a)

b)

c)
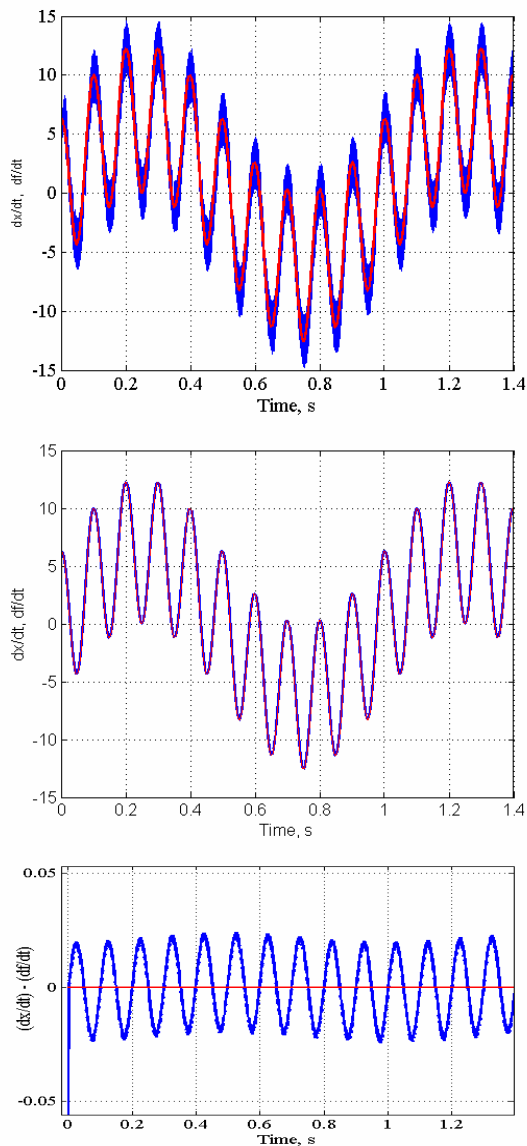
Fig. 15. Responses of differentiators, $f(t) = 1 + 0.1\sin(20t) - \cos(2\pi t)$, the noisy case: a) Levant's differentiator $\alpha = 500, \lambda = 35$ [4]; b) the proposed differentiator; c) estimation error of the proposed differentiator.

IV. CONCLUSION

A new control structure of real differentiator with LPF in the control loop is proposed in this paper. The proposed differentiator is compared with the well known Levant's exact differentiator. The obtained simulation with a variety of input signals show that the proposed differentiator shows significantly better results for to continuous-time input signals. For signals obtained from D/A converter the proposed differentiator needs a converter of very high resolution.

REFERENCES

[1]   Levant, "Robust exact differentiation via sliding mode technique", *Automatica* 34(3),379-384, 1998
[2]   J.-X. Xu, J. Xu, and R.Yan, "On sliding mode derivative estimators via closed-loop filtering", *Proc. of the 8th IEEE Workshop on VSS*, Barselona, Spain, Sept. 2004.
[3]   S. Kobayashi, S. Suzuki, K. Furuta, "Adaptive VS -differentiator", *Proc. of the 7th Int. Workshop on VSS,* Sarajevo, 2-4 July 2002, pp. 35-45.
[4]   V. A. Taran, "Application of nonlinear correction and variable structure for improving dynamic properties of automatic control systems". *Automatic & Remote Control* 25 (1), 1964, pp. 140-149.
[5]   R. Garirdo, Y.B. Stessel, L.M. Fridman, "Application of VS differentiators to DC servomechanisms, 8th Int. Workshop on VSS, Vilanova ila Geltru, 6-8 Sept. 2004.
[6]   Z. Pašić, "Obtaining signal derivative by using sliding mode", *Automatika* 5, 1971, 295-299. (in Serbo-Croatian)
[7]   V. I. Utkin, *Sliding Modes in Optimization and Control*, Nauka, Moscow, 1981.
[8]   S. Ibrir, S. Diop, "A numerical procedure for filtering and efficient high-order signal differentiation", *Int. J. Appl. Math. Comput. Sci,* 14 (2), 2004, pp. 201-208.
[9]   A. Tilli, M. Montanari, "A low-noise estimator of angular speed and acceleration from shaft encoder measurements", *Automatika* 42(3-4), 2001, 169-176.
[10] W. Gao, , J. C. Hung, "Variable structure control of nonlinear systems: A new approach", *IEEE Trans.* IE-40(1), 1993, pp. 45-55.

Self-Oscillating Fluxgate Current Sensor with Pulse Width Modulated Feedback

Radivoje Đurić and Milan Ponjavić

Abstract—A self-oscillating fluxgate current sensor with pulse-width modulated feedback is discussed in the paper. The current feedback creates additional dissipation in the circuit which could be reduced by applying the method of pulse-width modulation. For simplicity, the pulse-width modulator is realized as a self-oscillating structure whose frequency is adjusted by means of the hysteresis of a regenerative comparator, and the feedback is realized with no additional winding.

Index Terms—Fluxgate, self-oscillating, pulse-width modulation.

I. Introduction

THE most widespread sensors for galvanically insulated measurement of current are, at present, sensors based on the Hall-effect. The cheap open-loop Hall-effect sensors having low consumption, and of relatively low accuracy are realized as a silicon chip set in the air gap of a ferrite core [1]. The closed-loop Hall sensors having feedback have better metrological characteristics, linearity, accuracy, and bandwidth, but also a considerably higher consumption owing to the current which compensates the action of the measured current in the ferrite core. Both types have high values of the voltage offsets and drifts**.**

The fluxgate current sensors have the best metrological characteristics and have a considerably better sensitivity compared to the Hall-effect sensors. A standard realization of these sensors is carried out by the two windings, excitation and measuring, which are wound on a toroid magnetic core [2]. Through the excitation winding flows variable current causing a periodic saturation of the core. The conductor carrying the measured current passes through the center of the toroid and creates the asymmetry in the magnetic field of the core, which causes its asymmetric saturation, i.e. the appearance of even harmonics. The most frequently applied are the sensors detecting the second harmonic and a high linearity is accomplished by closing the feedback loop. When realized with the cores having no air gaps, they are, compared to the Hall effect sensors, insensitive to the influences of external magnetic fields. The commercial versions of thesesensors have one order of magnitude better

characteristics compared to the sensors based on the Hall-effect, but they are considerably more expensive.

There is a room for a class of sensors which have better immunity to external electromagnetic fields and better temperature variation of the characteristics compared to the sensors based on the Hall element, and which have good characteristics of the fluxgate current sensors, but are considerably simpler for realization, the so called self-oscillating fluxgate current sensors.

II. Self-Osillating Fluxgate Current Sensor

Compared to the classic fluxgate current sensor, the self-oscillating sensor operates based on the principle of autonomous generation of excitation for the secondary of the current transformer which serves for obtaining information on the current of the primary. This is voltage excitation and the self-oscillation process limits the excitation current of the secondary winding.

Fig. 1a shows an open-loop self-oscillating fluxgate current sensor. The basis of this sensor is the core whose simplified nonlinear characteristic is shown in Fig. 1b, where: L_m and L_{sat} are the magnetization inductances of the secondary when the core is not saturated and saturated, respectively, I_{sat} and φ_{sat} are the current and magnetic flux bringing the core to saturation. Thresholds of the Schmitt comparator are symmetric $V_{TL} = -V_{TH}$, therefore the corresponding current thresholds $I_{SL} = -I_{SH} = -V_{TH}/R_S$ are also symmetric. On the core characteristic of Fig. 1b the times, from t_1 to t_7, which correspond to the movement of the oscillator operating point during one full period at steady state are marked. Since $L_m \gg L_{sat}$, time intervals when the core is saturated, $t_2 - t_4$ and $t_5 - t_7$ are much shorter compared to the interval when the core is not saturated, thus the period of the self-oscillating process is approximately equal to

$$T_S \approx \Delta t_1 + \Delta t_2 , \qquad (1)$$

where $\Delta t_1 = t_2 - t_1$ and $\Delta t_2 = t_5 - t_4$.

At the initial moment of observation, $t = t_1$, the core comes out of negative saturation, thus

$$i_S(t) = i_S(\infty) + \left(i_S(t_1^+) - i_S(\infty)\right)e^{-\frac{t-t_1}{\tau}} , \ t_1 \le t \le t_2 , \qquad (2)$$

where the time constant is $\tau = L_m/R_S$.

Since inductance L_m is large, $\tau \gg \Delta t_1$, Δt_2, i.e. $e^{-t/\tau} \approx 1 - (t/\tau)$, and expression (2) can be simplified:

R. Đurić (e-mail: radivoje@gmail.com) and M. Ponjavac (e-mail: milan@el.etf.rs) are with the Faculty of Electrical Engineering, University of Belgrade, Serbia.

$$i_S(t) = i_S(t_1^+) + \left(i_S(\infty) - i_S(t_1^+)\right)\frac{t - t_1}{\tau}, \ t_1 \le t \le t_2, \quad (3)$$

$$i_S(t_1^+) = (I/n) - I_{sat} = I_{EQ} - I_{sat} \quad (4)$$

$$i_S(\infty) = V_{DD}/R_S, \quad (5)$$

where I_{EQ} is the equivalent measured secondary current.

(a) (b)

(c)

(d)
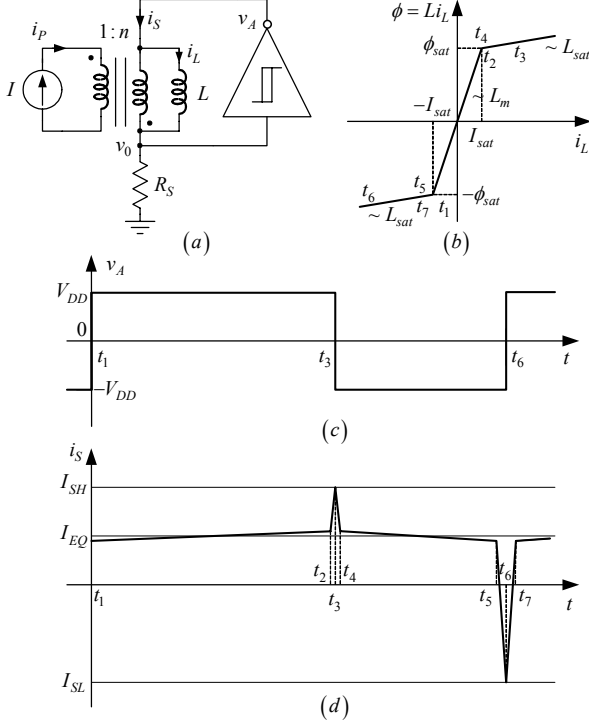
Fig. 1. The characteristic diagram of the open-loop self-oscillating fluxgate current sensor.

At the end of time interval Δt_1 the core is at the threshold of the positive saturation, $i_L = I_{sat}$, thus $i_S(\Delta t_1) = I_{EQ} + I_{sat}$, wherefrom one obtains

$$\Delta t_1 = \frac{2L_m I_{sat}}{V_{DD} - R_S I_{EQ} + R_S I_{sat}}. \quad (6)$$

In a similar way time interval Δt_2 is:

$$\Delta t_2 = \frac{2L_m I_{sat}}{V_{DD} + R_S I_{EQ} + R_S I_{sat}} \quad (7)$$

From (6) and (7), the approximate value of the period of oscillations is

$$T_S \approx \Delta t_1 + \Delta t_2 \approx \frac{4L_m I_{sat} V_{DD}}{V_{DD}^2 - (R_S I_{EQ})^2}, \ I_{EQ} \gg I_{sat}. \quad (8)$$

Since the average value of voltage across the coil is equal to zero, the average value of the output voltage is

$$\bar{v}_0 \approx V_{DD}\frac{\Delta t_1 - \Delta t_2}{\Delta t_1 + \Delta t_2} \approx R_S I_{EQ}, \ V_{DD} \gg R_S I_{sat}. \quad (9)$$

When the time interval of core in saturation is negligibly small compared to the interval when the core is not in saturation, the average value of current i_S is equal to the equivalent secondary current I_{EQ}. Then the slope of the linearized transfer characteristic

$$\bar{i}_0 = \bar{v}_0/R_0 = f(I_{EQ}) \quad (10)$$

is equal to one. Duration of the time interval when the core is saturated is finite and changes as a function of the measured current, thus in practice the slope of the transfer function is always less than one. Influence of the hysteresis losses in the ferrite core is significant only when the hysteresis loop has large coercive field and magnetic field in saturation B_{sat}. When parameter variation of the ferrite core and control electronics is small, fluxgate current sensors without feedback are an adequate solution in applications where a cheap sensor and accuracy not better than 0.5% are required [3].

III. CLOSED-LOOP SELF-OSCILLATING FLUXGATE CURRENT SENSOR

Static gain of the open-loop self-oscillating current sensor and maximum error of linearity, both dependent on sensor parameters and environmental conditions, are most sensitive to supply voltage variations. Closing the feedback loop is used in applications where the precise measurement of current, a wide bandwidth, and small variations of the gain and linearity with parameter variations are required. It can be realized according to the simplified scheme shown in Fig. 2, [4].
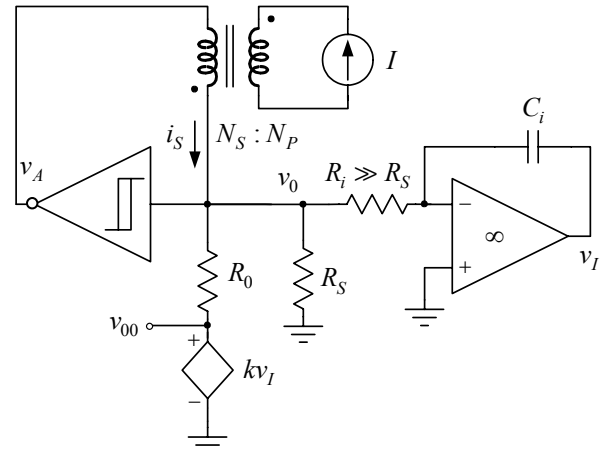
Fig. 2. Closed-loop self-oscillating fluxgate current sensor.

According to Fig. 2

$$V_I(s) = -\frac{1}{sT_i}V_0(s), \ T_i = \frac{1}{C_i R_i}, \quad (11)$$

$$I_s(s) = \frac{V_0(s)}{R_S \| R_0} - \frac{V_{00}(s)}{R_0}, \ V_{00}(s) = kV_i(s), \quad (12)$$

giving,

$$\frac{V_{00}(s)}{I_s(s)} = -\frac{R_0}{1 + \frac{sT_i}{k}\left(1 + \frac{R_0}{R_S}\right)} \quad (13)$$

and

$$Y_{0S}(s) = \frac{I_s(s)}{V_0(s)} = \left(\frac{1}{R_S} + \frac{1}{R_0}\right) + \frac{k}{sT_i R_0}. \quad (14)$$

On the basis of Fig. 2 and expression (14) it follows:

$$V_a(s) - V_I(s) = V_0(s) \text{ and } I_s(s) = Y_{0S}(s)V_0(s), \quad (15)$$

where from a block diagram is obtained which represents the circuit for regulation of current i_S, Fig. 3.
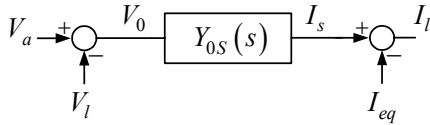
Fig. 3. Block diagram of the circuit for regulation of current i_S.

Since transfer function $Y_{0S}(s)$ is of the form of a PI regulator,

$$PI(s) = G_1 + \frac{G_2}{s}, \ G_1 = \frac{1}{R_S} + \frac{1}{R_0}, \ G_2 = \frac{k}{T_i R_0}, \qquad (16)$$

it is concluded that the steady state error reduces towards zero, i.e.

$$V_0(0) \to 0, \ I_l(0) \to 0, \ I_s(0) \to I_{eq}. \qquad (17)$$

Ideally, by means of an integrator and a controlled voltage source kv_1, $k>0$, it can be ensured that the average value of v_0 is equal to zero. This means that the variable and DC components of current i_S close their loops through resistors R_S and R_0, respectively, giving at the output the equivalent value of the DC measured current

$$v_{00} = -R_0 \overline{i_S} = -R_0 I_{EQ} = -R_0 I / n . \qquad (18)$$

Owing to a strong feedback, positive and negative peaks of the secondary current are of the same absolute value, thus the static gain is equal to one. Since the stray inductances are connected in series with the secondary winding, they do not affect the error of the static gain at steady state.

When the feedback loop is closed, an average current I_{EQ} is established through this contour and since there are significant voltage drops, the power dissipated in the circuit is increased. When the controlled voltage generator kv_I, or integrator output for $k=1$, are realized so that the output stages are in class A, B, or AB, they dissipate relatively high power, the consumption is increased and this may cause drifts of the current sensor characteristic, static gain, and linearity.

IV. PULSE-WIDTH MODULATION FEEDBACK

In order to reduce dissipation in the circuit of the current sensor a pulse-width modulator and a class D amplifier are used. Output stage of the class D amplifier contains switching transistors which ideally dissipate zero power, owing to zero current when turned off or zero voltage when turned on.

There are several types of pulse-width modulators, and they can be divided in two large groups. The first group consists of modulators having external generator of «triangular carrier», while modulators of the second group generate internally the carrier frequency, the so called self-oscillating pulse-width modulators [5]. Because of its simplicity the self-oscillating pulse-width modulator, shown in simplified form in Fig. 5., has been selected to close the feedback loop.

In the absence of the driving signal, $v_I = 0$, the circuit oscillates at a frequency which corresponds to the modulus of the loop gain equal to one and zero phase. Since the feedback is returned to the negative input terminal, the self-oscillation

requires an additional phase shift of 180° at the carrier frequency. This is provided by an integrator which introduces 90° phase shift and a phase delay through the comparator circuit and output switching transistors which add additional 90°. The comparator could be with or without hysteresis, depending on the desired carrier frequency. If there is no hysteresis, the frequency is determined by the delay introduced by the comparator circuit, while introduction of a hysteresis results in adjustment of the carrier frequency by the width of the hysteresis loop [6]

$$f_{PWM} = \frac{1 - M^2}{4(V_H / V_{DD}) T_{iPWM}}, \qquad (19)$$

where: V_H – width of the hysteresis loop, T_{iPWM} – time constant of the integrator, and M – modulation index of the pulse-width modulator.
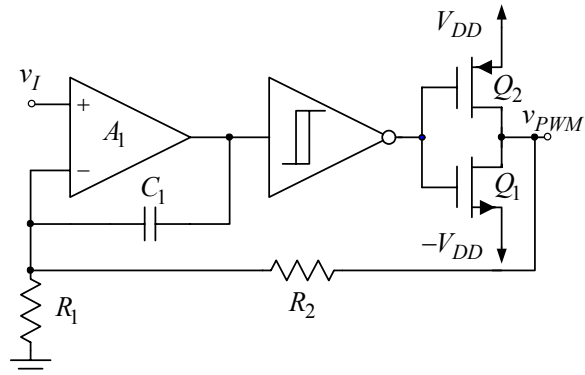
Fig. 4. Self-oscillating pulse-width modulator.

Low frequency signal is fed to input v_I of the amplifier and by the comparator and current feedback it is ensured that the output voltage of the modulator is pulse-width modulated and proportional to the input voltage. This voltage drives switches Q_1 and Q_2 and ensures low dissipation in them, i.e. efficient signal amplification.

The modulating frequency is much higher than the driving frequency, thus the transfer function of the modulator at the driving frequency

$$H_{PWM}(s) = \frac{V_{pwm}(s)}{V_i(s)} = \left(1 + \frac{R_2}{R_1}\right)\frac{1 + sC_1(R_1 \| R_2)}{1 + sC_1 R_2 / k_{PWM}}, \qquad (20)$$

where k_{PWM} is the gain from the output of amplifier A_1 up to output v_{PWM}.

Losses in the pulse-width modulator circuit can be presented in the form [7]

$$P_{PWM,loss} = P_{sw} + P_{cond} + P_g . \qquad (21)$$

In expression (21): P_{sw} – switching losses in the drain circuit,

$$P_{sw} = 0,5 C_{OSS} V_{DD}^2 f_{PWM} + I_{PWM} V_{DD}(t_f + t_r) f_{PWM}, \qquad (22)$$

where: $C_{OSS} = C_{ds} + C_{gd}$ are output capacitances of the switching transistors, $C_{OSS} = C_{OSS1} + C_{OSS2}$, t_r and t_f are the turn-on and turn-off times of the transistors, respectively; P_{cond} – conduction losses in the switching transistors,

$$P_{cond} = R_{on1,2} I_{PWM,rms}^2 , \qquad (23)$$

where R_{on} are the switch resistances, $R_{on1,2} = R_{on1} + R_{on2}$ and $I_{PWM, rms}$ is the rms value of the output terminal current of the PWM modulator, and P_g - switching losses in the gate circuit,

$$P_g = Q_{g1,2} V_{DD} f_{PWM} \,, \tag{24}$$

where Q_g is the charge required by the gate in order to turn on the switching transistor, $Q_{g1,2} = Q_{g1} + Q_{g2}$.

V. EXPERIMENTAL RESULT

In Fig. 5. the prototype of the sensor of Fig. 2. with pulse-width modulated feedback is shown. By resistive divider R_1 / R_2 and battery supply $V_{DD} = 2,5\,\text{V}$ thresholds of the comparator are adjusted to values $V_{TH} = -V_{TL} = 0,1\,\text{V}$, while $R_S = R_0 = 1\,\Omega$, $C_F = 3,3\,\mu\text{F}$, $L_F = 47\,\mu\text{H}$, and $T_i = 10\,\text{ms}$. Comparator circuit *comp* is realized by using standard LM311 comparator and Schmitt circuits 74HC14 which serve for shaping of driving pulses for the switching transistors ZXM64N02 and ZXM64P02. Ferrite core R12.5 made of standard ferromagnetic material N30 and $N_S = 200$ turns is used in the prototype. Switching frequency of the pulse-width modulator, where the same switching transistors as in the circuit of the current sensor with no feedback are used, is adjusted to 150kHz.
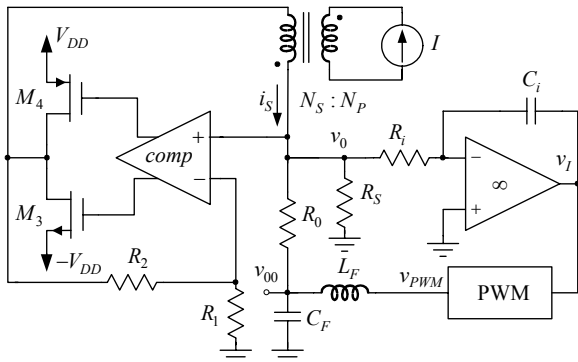
Fig. 5. Prototype of the self-oscillating current sensor with pulse-width modulated feedback.

By using prototype of Fig. 5 transfer characteristic of the current sensor $-\dfrac{N_S}{N_P} \dfrac{V_{00}}{R_0} = f(I)$, for the range of measured currents $-20\,\text{A} \le I \le 20\,\text{A}$, is taken and shown in Fig. 6.
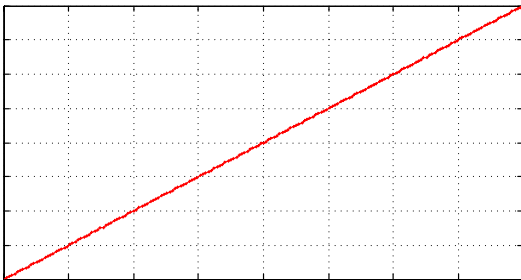
Fig. 6. Static transfer characteristic of the current sensor of Fig. 5.

Static gain of the current sensor $k_L = 0.999$ was obtained by curve fitting, while the maximum error of linearity was $\delta_{Lmax} = 0.1\%$.

Simultaneously, the record is made of the power consumption as function of the measured current, shown in Fig. 7, indicating that the maximum consumption of the current sensor amounted $P_{DD\max} \approx 70\,\text{mW}$. Dominant losses in the circuit are the conductive losses in resistances of the switches, coil, and resistance R_0, approximately amounting $P_{cond} \approx 40\text{mW}$. Switching losses in the drain circuit can be neglected, while $P_g \approx 5\text{mW}$. Owing to the self-oscillation, in the absence of the measured current somewhat less than 30mW is dissipated in the circuit. Variation of the switching frequency with variation of the consumption is small. Since low level currents are being switched, levels of the generated electromagnetic noise are low.
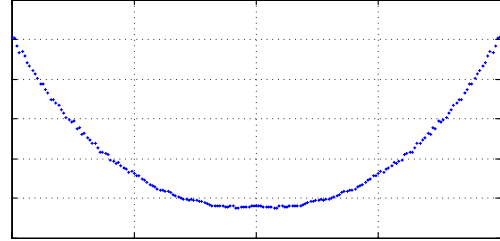
Fig. 7. Dependence of the power consumption as function of the measured current.

VI. CONCLUSION

On the basis of theoretical considerations a self-oscillating fluxgate current sensor with pulse-width modulated feedback has been realized. Fig. 6. indicates that this sensor has practically ideal transfer characteristic, which is a consequence of a strong negative feedback, while Fig. 7. shows that the current sensor has a very small consumption, 70mW at the most. Due to the good properties of negative feedback, the sensor is insensitive to variations of the supply voltage and circuit parameters. Due to pulse-width modulation is has low consumption, thus the sensor offers itself as a cheap and reliable solution for galvanically insulated measurement of DC current.

REFERENCES

[1] P.Ripka, "Current sensors using magnetic materials", Journal of optoelectronics and advanced materials, vol. 6, no. 2, pp. 587-592, June 2004.
[2] F. Primdahl, "The fluxgate mechanism, Part 1", IEEE Transactions on Magnetics, vol. 6, pp. 376-383, 1970.
[3] R. Đurić, M. Ponjavić, N. Smiljanić, "Galvanically insulated current sensor having digital output", INFOTEH-Jahorina, Vol. 8, pp. 379-383, March 2009.(in Serbian)
[4] P. Pejović, "A simple circuit for direct current measurement using a transformer", IEEE Transactions Circuits and Systems, vol. 45, no. 8, pp. 830-837, August 1998.
[5] B. Putzeys, "Simple Self-Oscillating Class D Amplifier with Full Output Filter Control", 118th AES Convention, Barcelona, May 2005.
[6] M. Berkhout, L. Breems, E. Tuijl, "Audio at Low and High Power", ESSCIRC 2008, pp. 40-49, September 2008.
[7] J. Honda, J. Adams, "Class D Audio Amplifier Basics", International Rectifier Application Note AN-1071.

Improving Efficiency of Power Electronics Converters

Milomir Šoja, Marko Ikić, Mladen Banjanin, and Milan Đ. Radmanović

Abstract—**This paper presents the analysis of power electronics converters efficiency and the basic procedures and methods for improving its (optimal topology selection, optimized design with selecting switching frequencies and using new types of power switches, application of digital control). Particular attention was paid to possibilities for efficiency improving by parallel connecting multiple converters with the appropriate turn ON/OFF strategy.**

Index Terms—**Power Electronics Converters, Efficiency Improving, Design Optimization, Digital Control.**

I. INTRODUCTION

THE most important characteristics of the power electronics (**PE**) converters are: low cost, high reliability and efficiency, small size, long life, **EMC**. Order of importance depends on the specific application. With the contradiction requirements, the design was necessary to achieve certain compromises. Recently, more attention is paid to procedures and methods for improving converter(s) efficiency: selecting the optimal topology, optimized design, and use of modern powerful switch in the power and digital components in the converter control system. Here is given an analysis of losses in the converter with the aim of better understanding the causes of certain types of losses and their impact on the efficiency. A new procedure for efficiency improving, parallel connecting of more converters with the use of appropriate turn **ON/OFF** strategies is described, which is expected to experience significant applications.

II. IMPORTANCE OF EFFICIENCY IMPROVING

Electric power represents about **40%** of the total energy consumption. **CPES** and **EPRI** estimates, for **2010**, through the **PE** device will be supplied about **80%** of consumers in the **US** [1]. It is possible to save about **30%** of electricity with

proper use of a new generation of **PE** devices [2]. Each percentage of improving converter efficiency has positive economic, environmental and other effects. The biggest effects are possible in the control of electric motors, lighting, electronic devices power supply (**PFC**), and renewable sources. Some specifications have been adopted for the purpose of recognition and popularization of efficient devices. Satisfying these specifications allows assigning certain efficiency qualifications to the devices. For **AC** input voltage power supplies ≤ **250 W** is assigned the **ENERGY STAR** qualification, if they meet **ENERGY STAR** specification **v2.0** in active and no-load mode and for true power factor [3]. **Fig.1.** shows given requirements for power supply ≤ **200 W** in active mode. For a nominal power ≥ **49 W**, average efficiency must be ≥ **0.87**. It is calculated as the arithmetic average value of efficiency, measured for all test voltages at **100, 75, 50,** and **25%** of the nominal current. In no-load mode (**Fig.2.**) it is defined **AC** maximum current. In addition, all qualifying power supplies with ≥ **100 W** input power must have a true power factor ≥ **0.9** at nominal current. There are other specifications (e.g. **80PLUS, 85PLUS** [4]), for other types of power supplies.
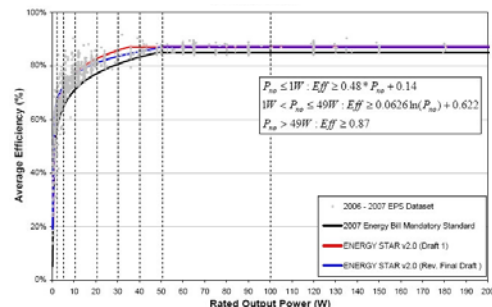

Fig. 1. ENERGY STAR v2.0 revised final draft specification, standard models, to 200 W [3].
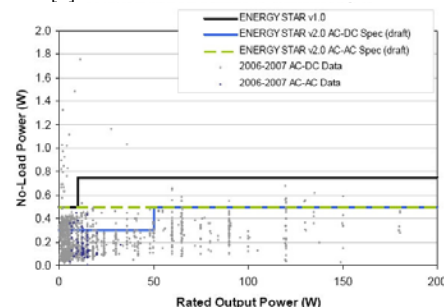

Fig. 2. ENERGY STAR v2.0 revised final draft, no-load spec [3].

III. METHODS FOR EFFICIENCY IMPROVING

Some basic methods and procedures for **PE** converter(s) efficiency improving are:
- Optimal topology selection,
- Design optimization,
- Efficiency optimization by digital control,
- Parallel connection of converters with the proper turn **ON/OFF** strategy.

A. Optimal topology selection

Choosing the right topology is vital to the success of the product and requires detailed knowledge of all the available choices. There are many well known circuits that fit certain applications well, but to find the best solution for a given application is needed to understand how the choice of topology may affect the key parameters, cost, overall size, **EMC** performance and efficiency. The importance each of these parameters varies between application and trade-offs made between each of them have a significant effect on the choice of topology. In order to choose the most appropriate topology designer needs to consider the attributes of possible solutions by adopting a simple scoring process. Each topology have to be evaluated in two stages; firstly for most important, and then for less important characteristics. Each attribute would be ranked, e.g. from "**1**" meaning bad through to "**5**" meaning good, and the results of both stages would be weighted together. The scores should be combined with weighting where the most important factors (efficiency, cost) are more heavily weighted than less important. After applying these weightings designer can eliminate unsuitable topologies.

New topologies, which bring significant benefits in terms of the most important characteristics, including efficiency, appear in all areas of application **PE** converters. [5] [6] [7]

B. Design optimization

Converter design optimization is reduced to defining the objective function (efficiency, price and etc., or a combination of them) and finding its maximum/minimum. Defining the objective function means finding a mathematical dependency (efficiency) of all relevant variables in the system [8], while finding the extreme requires development of complex software tools able to quickly solve the task and provide a quantitative analysis of the impact of individual requirements and operating conditions on the value of objective function. The use of optimization techniques in the component design of **PE** systems offers the following attractive advantages: [9]

−Complete automated component design tools can be developed, that allow:
- improved solutions with respect to traditional design procedures, since more complexity can be considered in the design process,
- in a reduced design time, once the optimization problem has been specified and the appropriate tools to solve it developed.

−Quick assessment of optimum solutions for different sets of specifications, evaluation of the design objective function sensitivity with the variation of certain specifications and parameters, etc.

−The application of optimization techniques in the design has also an added educational value, since the optimization tool will highlight the critical aspects in each design scenario, allowing the user to focus his attention on these aspects and gain a better understanding of the system design peculiarities.

−In a traditional design approach, each designer often follows his own particular design methodology which, on the other hand, is not rigorously specified anywhere. In contrary, the use of optimization techniques pushes the design team to work jointly to clearly and rigorously specify the design problem and methodology for its solution, which also allows future revisions to improve the design formulation. It provides a written and clear record of the design approach.

On the other hand, there are still several challenges to improving the practicality of optimization techniques:
- Efficient models of the system cost, performance, etc., have to be developed, fast and accurate enough for an optimization process requiring hundreds of design evaluations.
- The component data sheets do not always contain all the required information, and there are often significant differences among the data provided by each manufacturer. Some standardization would help the application of optimization techniques in the design process.
- The formulation of the optimization problem and the development of the tools to solve it require some time. The time required, however, decreases substantially once several design problems have been solved, since the component parameter definition, the component database, certain common models, etc., are already available.
- A real design process is complex, involving several considerations, some of which are hard to identify and express quantitatively. However, once identified they can normally be expressed in some acceptable mathematical form in order to be incorporated into the design problem formulation.

The usage of optimization techniques is particularly recommended in situations when is needed a big improvement in the design of certain characteristics, but also in cases where a small bit of improvement is important. In [9] is given an example of an optimized design of **1 kW PFC** boost converter, with a price as the objective function, where the total price reduced by **58%** compared to the traditional design solution.

On the converter efficiency decisively influence the switching frequency and characteristics of semiconductor switches, which makes them special attention.

1) Optimal switching frequency

Total converter losses are:

$$P_{loss} = P_{cond} + P_{fixed} + P_{sw} \tag{1}$$

- P_{cond}: conducting losses,
- P_{fixed}: fixed losses (independent of the load and f_{sw}),
- P_{sw}: switching losses.

At the critical frequency (f_{crit}), switching losses are equal to other losses. It is switching frequency limit of real converters, because increasing frequency over f_{crit} leads to rapidly decreases of converter efficiency [8]. Another criterion for selecting the switching frequency is related to the satisfied achievement of **EMC**. There is a set of frequencies at which the **EMC** limits are minimum [10], and operation on some of them allows the use of smaller **EMC** filter and greater freedom in the selection of critical components. Optimum switching frequency should be chosen from that set, provided $f_{sw} < f_{crit}$.

2) New powerful semiconductor components

Powerful semiconductor switches have decisive influence on the **PE** converter(s) efficiency. Continuous reduction of switching and conduction losses results in increasing switching frequency simultaneously reducing the converter size, with no reduction in efficiency (or improving efficiency). After decades of development, characteristics of powerful semiconductor switches, based on **Si** technology, moved closer to the limits. Fortunately, in the near future, new technologies and materials will create components with dramatically improved characteristics, which will allow further accelerated development **PE** converters. One of these technologies is based on **SiC** (*Silicon Carbide*), which has some unique characteristics that make it an almost ideal material for high voltage or high temperature operation. First, the thermal conductivity of **SiC** is several times higher than that of **GaAs** and more than three times higher than that of **Si**, which enables the production of components that operate on higher currents. Also, the breakdown voltage of **SiC** is about ten times higher than that of **Si**, so it is possible to make high-voltage Schottky diode which has a negligible reverse current compared to conventional **Si PiN** diode, independent of temperature, operating current and switching *di/dt*. Their recovery voltage is equal to zero and have almost immediately extinguishing, which drastically reduces the switching losses of **MOSFET** (**IGBT**), and in good part eliminates **EMI**. Converter efficiency is significantly improved, also in many cases with simplifying of **PE** converter topology. **Fig.3.** shows **PFC** boost converter with **Si PiN** diode on the left, and with **SiC** diode on the right side. Converter with **SiC** diode is much simpler and more efficient because there is no need for commutation circuit. [11]
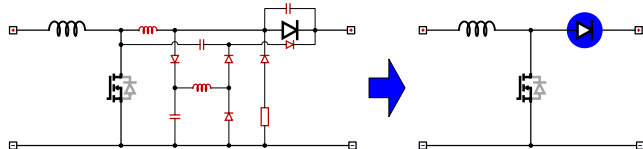
Fig. 3. Boost converter with standard Si PiN and with SiC diode.

Similar effects are achieved by using **SiC** diodes in the inverter, where the average efficiency reached **97.5%** (record **>99%, Si 96%**) as a result of reduced losses by **25%**. Applied to the **PV** system, this inverter allows conversion more solar energy into electricity, which, taking into account that the **PV** systems should work at least **30** years, is a great improvement

in energy saving means, faster investment return, and because of lower operating temperature, extended life. First power module with all **SiC** components is introduced in [12]. Basic problems in **SiC** technology are high cost and limited supply.

A revolutionary new power devices, based on **GaN-on-Si** (*Gallium Nitride on Silicon*) technology developed by **International Rectifier Corporation** (**IR**), promises to deliver cost-effective performance that is at least ten times better than existing **Si** devices, to enable dramatic reductions in energy consumption and improving of **PE** converter efficiency in end applications in markets such as computing and communications, consumer appliances, lighting and automotive applications. **GaN** transistor with high mobility of electrons (*High Electron Mobility Transistors* - **HEMT**) provides a major improvement of key characteristics ($R_{DS(on)} \times Q_{sw}$ is **33%** less than the last generation **Si MOSFET**) and allows the converter realization where the product **efficiency×power_density/price** is at order of magnitude better than existing **Si** and **SiC FET**'s [13]. The reverse recovery characteristics (Q_{rr}) of high voltage **GaN** diode is the same as for commercially available **SiC** diodes, both being significantly better than state-of-the-art silicon fast-recovery diodes (**FRED**) (**Fig.4.**). Characteristic is "*soft*" due to the essential absence of holes in the **GaN HEMT** structure, eliminating the minority carrier effect in reverse recovery charge Q_{rr}. These results are eliminating the otherwise needed filtering (snubber) circuitry. In turn, this reduces system size, cost and weight, and has been used extensively in **PFC** circuitry in **AC-DC** converters using expensive **SiC** diodes and when anti-parallel diode functions are required, such as **IGBT**s in motor drive circuitry. Demonstration of the advantages of the new **GaN-on-Si** components is shown in [13].
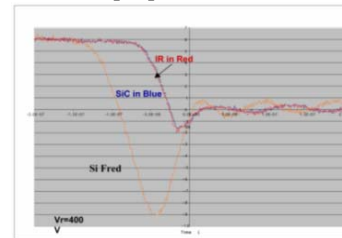
Fig. 4. Reverse recovery characteristics of 600 V GaN, SiC and Si FRED diode [13].

Great progress in reducing size and improving efficiency is achieved by the integration of functional **PE** converter components and using **IPEM** (*Integrated Power Electronics Module*) and **PEBB** (*Power Electronics Building Block* [7]), which, except a powerful switches, contain electronic driver modules, protection, measuring and etc.

C. Efficiency optimization by digital control

The application of digital control brought new opportunities for improving **PE** converters efficiency. Particularly interesting for the application of digital systems is multi-phase control, which is now widely applied to power supply converters for microprocessors, **FPGA** and similar components, as well as the **PFC** circuits. Phase shedding and

other forms of phase control (the order, compensation, balancing) allow converter efficiency optimization over a wide range of operating conditions without degrading other characteristics. The essence of the technique leads to reduce switching losses by turning on as many phases as needed for each load level. **Fig.5.** shows influence of phase control on the efficiency of four-phase synchronous buck converter (V_{in}=10 V, V_{out}=1 V, 500 kHz). [14]
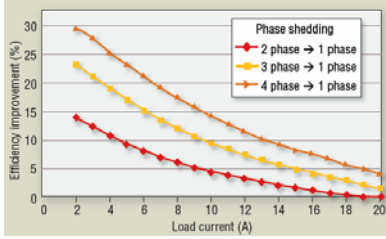
Fig. 5.   The influence of phase control on the efficiency of four-phase synchronous buck converter.

Except phase shedding the digital control can remember operating parameters, allowing the controller to make choice how to enable and disable phases in individual situations.

Digital control can further improve the efficiency of the synchronous buck converter by controlling "*dead time*" of **MOSFET**. Optimization of **MOSFET** switching and minimizing "*dead time*" can improve efficiency by **1%** or **2%**, depending on the application. [15]

An excellent example of improving efficiency using a digital control is given in [16]. It shows **400 W BCM** (*Boundary Conduction Mode*) two-phase **PFC** converters, controlled with **FAN9612**. Part of the **FAN9612** synchronization circuit utilizes a maximum frequency clamp to limit frequency-dependent C_{oss} **MOSFET** switching losses at light load and near zero crossing of the **AC** input voltage. During the portion of the line voltage for V_{IN} greater than V_{OUT}/2, C_{oss} capacitive switching losses are further reduced through a valley-switching technique used to sense the optimal **MOSFET** turn-on time. Conversely, when V_{IN} is less than V_{OUT}/2, the main power **MOSFET** turns-on using zero voltage switching (**ZVS**).
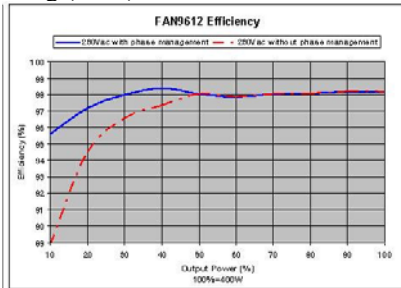
Fig. 6.   Phase management efficiency performance [16].

ZVS in conjunction with zero current switching (**ZCS**), from **BCM** operation, eliminates **MOSFET** turn-on switching loss and reverse recovery loss in the output rectifier. **FAN9612** automatically disable one phase at **30%**, and enable at **40%** load current (adjustable in the appropriate input **FAN9612**). **Fig.6.** show the measured efficiency improving at low loads **6.5%** at V_{IN} = 230 V_{AC}.

IV.   POWER CONVERTERS EFFICIENCY ANALYSIS

A function $P_{loss}(x)$ represents **PE** converter losses, where x is related to the output or input current:

$$P_{loss}(x) = a_0 + a_1 x + a_2 x^2 + a_3 x^3 + a_4 x^4 + ... + a_n x^n , \qquad (2)$$

Whose fixed coefficients a_0, a_1, a_2... a_n correlate well to the different sources of power loss [17] [18]. For instance, a_0 represents fixed overhead losses independent of input/output current. The losses associated with the second coefficient, a_1 are directly related to the input/output current and can be typified as output diode losses, switching losses and losses due to "*dead time*" in synchronous rectifiers. The third coefficient, a_2 is easily recognized as conduction losses. It is typified as losses in the resistances of the **FET**, magnetic wiring and interconnect. Useful results can be obtained by considering only the first three coefficients. (2)

$$P_{loss}(i_o) = a_0 + a_{1.o} i_o + a_{2.o} i_o^2 \qquad (3.1)$$

$$P_{loss}(i_{in}) = a_0 + a_{1.in} i_{in} + a_{2.in} i_{in}^2 \qquad (3.2)$$

The appropriate expressions for the efficiency are:

$$\eta(i_o) = \frac{P_{out}}{P_{out} + P_{loss}} = \frac{v_o i_o}{v_o i_o + a_0 + a_{1.o} i_o + a_{2.o} i_o^2} , \qquad (4.1)$$

$$\eta(i_{in}) = \frac{P_{in} - P_{loss}}{P_{in}} = \frac{v_{in} i_{in} - \left(a_0 + a_{1.in} i_{in} + a_{2.in} i_{in}^2\right)}{v_{in} i_{in}} . \qquad (4.2)$$

Coefficients a_0, a_1, a_2 are determined experimentally by measuring the losses in the three operating points and forming and solving resulting matrices. The solution is simplified if one of the loss measurements is no−load case, where all of the losses are equal to the first coefficient, a_0. The problem then reduces to two equations and two unknowns, which are easily solved. Once the coefficients are calculated, a loss curve can be constructed showing the three loss types. The presented method for the losses determination in the **PE** converter give the power supply designer useful insight into understanding the actual circuit losses and good opportunities for the analysis of circuits with different operating modes. Experimental determination of losses should be approached cautiously.

Functions (4.1) (4.2) can be optimized, selecting the parameters a_0, a_1, a_2, in order to achieve maximum average efficiency: [19]

$$\eta_{max} = \frac{v_o}{v_o + a_{1.o} + 2\sqrt{a_0 a_{2.o}}} , \qquad (5.1)$$

and

$$\eta_{max} = \frac{v_{in} - a_{1.in} - 2\sqrt{a_0 a_{2.in}}}{v_{in}} = 1 - \frac{a_{1.in} + 2\sqrt{a_0 a_{2.in}}}{v_{in}} , \qquad (5.2)$$

and occur at currents:

$$i_{opt} = \sqrt{\frac{a_0}{a_{2.o}}}, \quad i_{opt} = \sqrt{\frac{a_0}{a_{2.in}}}. \tag{6}$$

Equation (6) shows that the coefficient a_1 does not affect the current value at maximum efficiency. This is because it is related to losses that are proportional to output current. So as output current increases, these losses and the output power increases directly, and there is no impact on efficiency. Besides, optimum efficiency occurs at a point where the fixed losses and the conduction losses are equal. This implies that designer should be able to optimize efficiency as long as there is control over the components that determine the value of a_0 and a_2. Regardless of this, it should be worked to reduce the value of a_1, in order to improve overall efficiency. The values a_0 and a_2 can be influenced by proper selection of power switch. E.g., selection of power **MOSFET** with a corresponding surface (semiconductor) and active resistance $R_{DS(on)}$, affect control losses, losses of output capacitors and circuit surge protection losses. $R_{DS(on)}$ and the conducting losses are reverse and parasitic capacitance and switching losses connected with them, are directly proportional to the surface. Therefore, it is possible to select the optimal combination of surface and resistance. In [17] is showed that the losses were minimal in the broad area of surface, which allowing the designer flexibility in trading the cost of the **MOSFET** for the loss reduction achieved. Minimum loss occurs when drive loss equals conduction loss. **Fig.7.** is an efficiency plot for three normalized die area around optimum point.
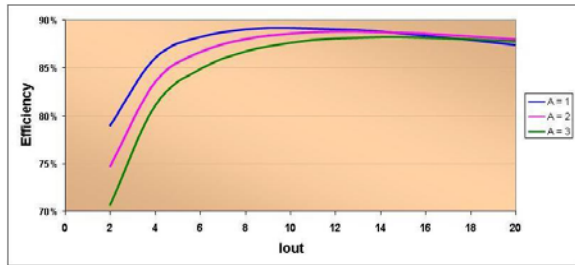
Fig. 7. Efficiency peak occurs before full current rating [18].

At light loads, the efficiency of the larger area is penalized by increased drive losses, while at heavy loads the smaller area device suffers due to increased conduction losses. It is important to note that these curves represent a three-to-one variation in die area and cost. The design with a normalized die area of one is just slightly less efficient than the larger design at full power, and is higher efficiency at light load where the design may typically run.

V. IMPROVING EFFICIENCY BY PARALLEL CONNECTED CONVERTERS

New and very significant opportunities for **PE** converters efficiency improving brings concept based on the parallel connection of multiple converters, with an appropriate turn **ON/OFF** strategy. Let realize the power supply with maximum efficiency, for variable load (0-P_{nom}). Identical converters are available, with maximum power $P_n = P_{nom}/n$ (n-number of the converter), efficiency η_n and possibility for parallel connection and independently turn **ON/OFF**. Two different implementation of the power supply are possible, depending on the **ON/OFF** strategy of individual converters.

S₁: All n converters, with uniform current sharing, are permanently turned **ON** (usually the case). The system acts like single converter which efficiency (η_1) corresponds to the efficiency of an individual converter (η_n):

$$\eta_1 = \frac{p_{out}}{p_{out} + p_{loss}} = \frac{np_n}{np_n + np_{n.loss}} = \frac{p_n}{p_n + p_{n.loss}} = \eta_n \tag{7}$$

- p_{out}: output power of n converters,
- p_{in}: input power of n converters,
- p_n: power of individual converter,
- $p_{n.loss}$: individual converters losses.

The basic disadvantages of this strategy are the low efficiency at light loads, and the fact that all converters are always turned **ON**, which potentially can reduce the reliability and lifetime of power supply system.

S₂: Next ($m \leq n$) converter is turned **ON** only after the (m-1) previous turned **ON** converters are loaded with nominal power P_n. The efficiency of power supply system is:

$$\eta_2 = \frac{p_{out}}{p_{out} + p_{loss}} = \frac{(m-1)P_n + p_n}{(m-1)(P_n + P_{n.loss}) + p_n + p_{n.loss}} \geq \eta_n \tag{8}$$

- p_{out}: output power of n converters,
- p_{in}: input power of n converters,
- P_n: nominal power of individual converter,
- p_n: power of individual converter,
- $P_{n.loss}$: converters losses at nominal power,
- $p_{n.loss}$: individual converters losses.

The following figure (**Fig.8.**) show improving of efficiency for **2** and **4** parallel connected converters with **S₂** strategy implemented. For simplicity, examples were made with the assumption that the losses of the converter are constant in the whole range of power, which does not diminish the generality of the solution. In the case of different efficiency curves (maximum efficiency occurs when the power is <P_n) essence of strategy remains the same, only the turn **ON/OFF** thresholds of certain converters have to be adjusted. Colored area, on the efficiency diagrams, gives an improvement by using strategy **S₂** compared to **S₁**. The efficiency improving is evidently in the whole range of power. When the all converters are turned **ON** the efficiency is identical to **S₁**. **Fig.8.b** shows that there is a difference in the efficiency improving using **4** compare to the **2** converters. Theoretically, the larger number of converters means higher opportunities to efficiency improving. However, in practice, the numbers of converters that can be simultaneously connected are limited. In addition, a higher number of the converters means reduction of individual power, which after a certain limit leads

to reduced efficiency of individual converter (losses cannot continue to decrease), which negatively affects the overall efficiency.

a)   b)
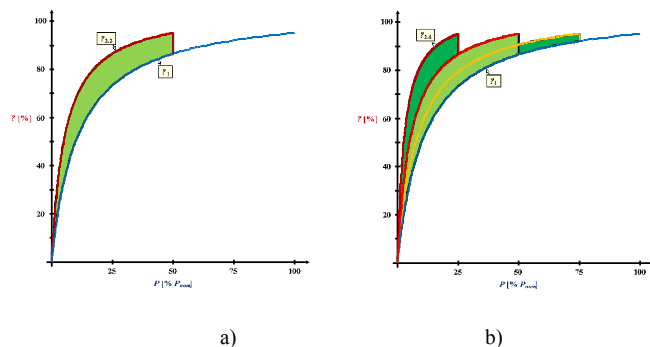
Fig. 8. Efficiency improving by 2 (a) and 4 (b) parallel connected converters.

The big advantage of S_2 strategy is the possibility of individual converters equally using, depending on how long they have each operated, in order to reach higher reliability and sustainability (converters are turned **ON** minimum required time). In addition, if one of the power circuits were to stop working for whatever reason, the others can continue to work independently. It is possible to find practical examples that confirm the benefits of the S_2. [20] [21]

Great opportunities for the S_2 strategy implementation offer **microinverters**, a relatively new option for optimizing **PV** system efficiency. Microinverters are based on the concept of **"single PV panel-single inverter"**. The chief benefit of the microinverter topology is that the system will continue to convert energy even when one (more) inverter malfunctions. Another important advantage is the ability to adjust conversion parameters on each panel. Clouds, shadows and other environmental conditions can vary the output of individual panels. Equipping each panel with its own microinverter allows the system to accommodate its changing load, which provides optimum conversion for both individual panels and the entire system. [22] [23]

Currently, microinverters were connected in the supply system using S_1 strategy. Microinverter with several parallel units would enable the application of S_2 and further improving its efficiency. Besides, in the existing control system for tracking and monitoring is possible, without additional investment, implement S_2 strategy and include as many microinverters is really needed to supply a particular load, with better utilization of individual microinverters/**PV** panels and improving the efficiency of the entire **PV** power supply system.

VI. CONCLUSION

By implementation appropriate design procedures and methods and usage of modern powerful switches in the power and digital components in control part, it is possible to

significantly improve the efficiency of **PE** converters. The completed analysis of converter losses allows a better understanding of their origin and points on possible directions of improving efficiency. The principle of parallel connecting multiple converters, with appropriate turn **ON/OFF** strategy, offers a significant potential to improve efficiency, which is confirmed by the latest developments in applied **PV** power systems.

REFERENCES

[1] Lee F.C., "*Power Electronics System - Introduction*", Virginia Tech, 2005.
[2] "*Power Electronics System-A Joint Course*", taught by Virginia Polytechnic Institute and State University (Virginia Tech), 2005.
[3] Vince Biancomano, "*Energy Star update eases Active efficiency spec*", POWER MANAGEMENT Design Line, March, 2008.
[4] John Chiem, "*How to boost your embedded design's power supply efficiency*", POWER MANAGEMENT Design Line, February 2009.
[5] Andrew Skinner, "*Choosing the right power supply topology*", POWER MANAGEMENT Design Line, April 2009.
[6] Issa Batarseh, "Research Activities in Power Electronics at UCF", Florida Power Electronics Center Orlando, Florida USA, 2003.
[7] Dushan Boroyevich, "*Power Electronic Converters for Advanced Electric Power Systems: The DOE Workshop on Systems Driven Approach to Inverter R&D*", Center for Power Electronics Systems, April 2003.
[8] Erickson R. W., Maksimovic D., "*Fundamental of Power Electronic - second edition*", Springer Science+Business Media, LLC, 2001.
[9] Sergio Busquets-Monge, "*Application of Optimization Techniques to the Design of a Boost Power Factor Correction Converter*", Master thesis, Virginia Polytechnic Institute and State University, Blacksburg, Virginia, 2001.
[10] Erik Hertz, "*Thermal and EMI Modeling and Analysis of a Boost PFC Circuit Designed Using a Genetic-based Optimization Algorithm*", Master Thesis, Virginia Polytechnic Institute and State University, 2001.
[11] Alfred Hesener, "*How a power switch can save the world*", Embedded Europe, August 2009., (www.embedded-europe.com),
[12] Sam Davis, "*SiC and GaN Vie for Slice of the Electric Vehicle Pie*", Power Electronics Technology, November, 2009.
[13] Michael A. Briere, "*GaN-based power devices offer game-changing potential in power-conversion electronics*", INDUSTRIAL CONTROL Design Line, December 2008., (www.industrialcontroldesignline.com),
[14] Dave Freeman, "*Digital Power Control Improves Multiphase Performance*", Power Electronics Technology, December 2007.
[15] Marty Pandola, "*Explore the Lesser-Known Benefits of Digital Power*", Power Electronics Technology, November 2006.
[16] Steve Mappus, "*Intelligent Interleaving: improving energy efficiency in AC-DC power supplies*", POWER MANAGEMENT Design Line, March, 2008., (www.fairchildsemi.com/pf/FA/FAN9612.html),
[17] Robert Kollman, "*Power Tip #11: Resolve Power Supply Circuit Losses*", POWER MANAGEMENT Design Line, June 2009.
[18] Lars Petersen, "*High Efficient Rectifiers*", Ph.D. Thesis, Ørsted•DTU, Automation Technical University of Denmark, August 2003.,
[19] Robert Kollman, "*Power Tip 12: Maximize Power Supply Efficiency*", POWER MANAGEMENT Design Line, June 2009.
[20] Yang Qiu, "*Improving the interleaved DC/DC converter*", POWER MANAGEMENT Design Line, September, 2008.
[21] FRONIUS INTERNATIONAL GMBH, 2009., (www.fronius.com),
[22] Keith Ogboenyiya, "*Taking Energy Efficiency to the Next Level*", Texas Instruments, SPRAAZ6-September 2008.
[23] Graham Jesme, "*Solar Power Optimizers Gaining Market Share*", November, 2009.,(www.RenewableEnergyWorld.com).

Design of an Open Software Architecture for Leg Control of a Walking Robot

Mladen Milushev

Abstract—**In this paper we present a general description and a Software design of a six-legged laboratory prototype robot. The work presented in this paper has been carried out within a project concerning the investigation of a modular architecture for control of mechatronic multi-link structures at the Faculty of Mechanical Engineering, Technical University of Sofia.**

The presentation describes the software that is designed to control the hardware and the actuators and thus the whole machine. The software design is described in detail, the division into modules, each module and the important algorithms. Thus it is easier to grasp is the description in the form of block diagrams. In addition, it should include possible extensions already in the planning.

Index Terms—**Mechatronics System, Walking Robot, Embedded Control, Modular Control, Sensor.**

I. INTRODUCTION

SIX legged locomotion is the most popular legged locomotion concept because of the ability of static stable walking. The hexapods are often inspired by nature; two examples of such robots are Lauron [1] and Genghis [2]. Most of the walking robots are laboratory prototypes [3, 4, 5], but there are also few walking machines built for specific applications, such as SILO06 [6], a six-legged robot built for humanitarian demining.
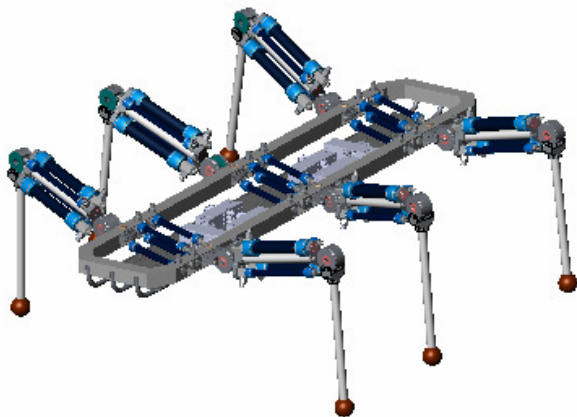
Fig.1. Leg-to-body attachment design.

In this paper we consider a walking robot with six identical legs equally distributed along both sides of the robot body in three opposite pairs. The leg joints are driven by pneumatic muscles (FESTO). So far the six-legged walking robot (Fig. 1.) has been developed using Solid Woks.

II. HARDWARE PLATFORM

For the walking robot *BiMoR* (**B**iologically **M**otivated **R**obot) a hierarchical and distributed computing architecture has been selected. By distributing the possibility of concurrent control functions is implemented on various micro-controllers. Through the concept of distribution the need for communication is generated. The communication based on the master-slave principle with provides a suitable option for the control system for keeping the protocol economical and within the determined time limits for securing safety to the critical functions. It is important that the used sensors provide information about the absolute co-ordinates. The hardware of the control system must fulfill the following tasks:

- collection and analysis of the measured variables;
- calculation of tax information;
- output control signals to the actuators.

For executing the basic legs functions like the closed-loop joint control (valve control, recording signals from the joint encoders) six R8C/23-microcontrollers are installed. On a basic level each sensor and actuator are connected with the interface board to the micro-controller board. The R8C/23 microcontroller is installed on industrial controller boards and contains one Full CAN module, which can transmit and receive messages in both standard (11-bit) ID and extended (29-bit) ID formats.

III. SOFTWARE SYSTEM DESCRIPTION

The software for the leg's local control is comprised of five modules shown in Fig. 2 along with the related interactions. Both processes run in cycles the first one - *JC_Таск, Joint Control,* tracks down and regulates the motion of the three joints; the second one *CAN_Таск, Controller Area Network* is in charged with the Master generated messages. These

M. Milushev is with the Faculty of Mechanical Engineering, Technical University of Sofia, Bulgaria (e-mail: mcm@tu-sofia.bg).

processes are regulated by the *Main* Module.
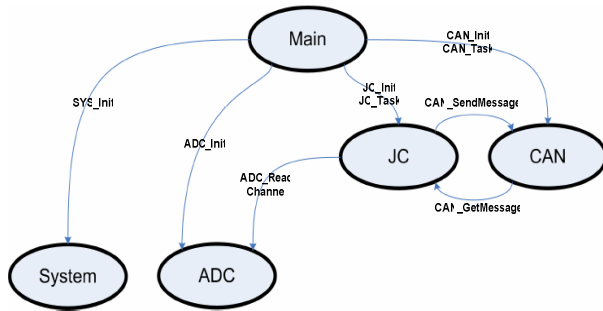
Fig. 2. Software modules and their interactions.

A. *Main module*

This module is the main module (Fig. 3.). It contains only one main function, which has the role of the operating system. It initializes all the modules in the correct order and carries out both processes are cyclical. It obeys to the following initialization rules:

- The system module should be initialized before CAN and ADC, as the CAN and ADC clocks from the Main-clock dependent.
- ADC will be initialized before JC just as with the JC-initialization of the A/D converter - the leg is put in the initial position.
- CAN must be initialized before JC, as in the JC-initialization a CAN module is used. The microcontroller sends this message to the master: "successful initialization" or "initialization error".
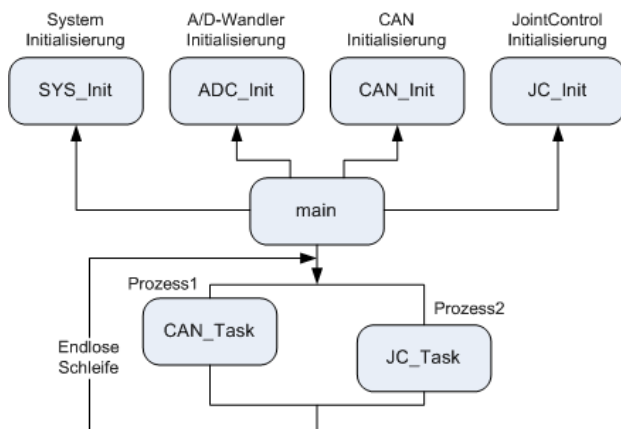
Fig. 3. Block diagram of main function.

B. *System module*

Simple module to the system initialization – in this case it will be the clock source, clock pre scalar configured and parallel inputs and outputs defined and configured.

C. *ADC module*

This module does the functions of configuration and access to the A/D converter of the microcontroller. The configuration is done through the following steps:

- Choice and setting of the AD channels
- ADC-Clock Set (10 MHz)

- ADC-resolution set (8-bit mode)
- ADC-set mode (one-shot mode)
- A/D conversion method you choose (with Sample and Hold)

The ADC module is currently used to measure the actual value of each of the three joint angles provided but also for other local sensors (for example force sensor and pressure sensor). This will gain through an interface function. She gets as parameters the number of analog input, and then read it very easily to other sensors - one must know only the number of analog input.

D. *CAN module*

Module to configure and control the CAN controlle - implemented were the following functions (Fig.4.):

- *CAN_Init* - function for setting the CAN SFRs: CAN clock (10 MHz), CAN baud rate (500 kbps) and CAN mode (Basic CAN),
- *CAN_ConfigRxSlot* - function for setting a CAN-slot as a CAN-RX slot. There are also interface functions to communicate with the master available.
- *CAN_SendMessage* - Function to send a message to the master via the CAN bus.
- *CAN_GetMessage* - When a new message is completely received it will be copied using this function from the CAN internal RX-buffer in a application RAM-buffer. The execution should happen as quickly as possible because it is being called into the CAN-RX-interrupt.
- *CAN_Task* - one of the two cyclic processes. This function checks whether new messages exists in the receive buffer and if so - they are removed (consumed) from the buffer and processed further.
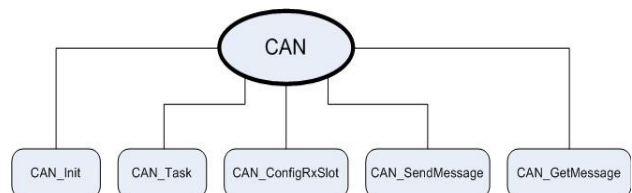
Fig. 4. Functions implemented in the CAN module.

JC module

In this module two abstract levels are introduced - leg and joint. Each level is assigned to its own state, which is updated regularly and individually. In Fig. 5. are shown the functions that are to be implemented in the JC module.
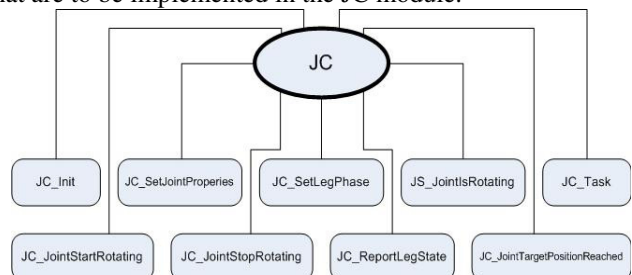
Fig. 5. Functions implemented in the JC module.

JC_Init Function

After switching on and initialization of the system, the ADC - and CAN-modules, each leg enters the state *LEG_STATE_POWERED_UP* and "reports" on to the master. If all six legs are prepared (the master has received six certificates), the master sends to the 1st, 3rd and 5th leg a *INIT-command* - put the leg in a starting position. Each of these legs occurs in the state *LEG_STATE_INIT* and performs an INIT-procedure:

- The leg is lifted (by the β-joint);
- The remaining two joints (α and γ) are set in start position;
- The leg is placed (again, through the β-joint);

The first joint (angle **ά**) is perpendicular to the robot's body; the first (angle **ά**) and second (angle **β**) joints are perpendicular то one another, while the second (angle **β**) and third (angle **γ**) are parallel. At this point, all three joints are in their initial position (in the state *JC_STATE_STATIC_INIT*, - the leg is initialized and the state *LEG_STATE_READY* is set. A confirmation message to the master will be sent. All three legs have sent the confirmation and then sent the INIT-command to the master of the 2nd, 4th and 6th legs. The legs are initialized in pairs so that the body always remains stable.

JC_SetJointProperties Function

If the leg is in the state *LEG_STATE_READY* it can accept set-points. They will be transferred by the master of the CAN bus and checked through the function *JC_SetJointProperties* for validity. The valid values are in the range [0x06 ... 0xF9] or [26.5 ° -26.5 ° ...]. For security reasons 1° shift on the left for both side-positions is allowed. The values represent the start and end positions where a phase change takes place. The "longest" step is defined, for example, at a starting value of 0x06 (26.5 °) and at a final value of 0xF9 (-26.5 °).

JC_SetLegPhase Function

When the set points are accepted the leg can be set in motion. The command is sent again from the master through the CAN bus. Upon receiving a suitable value (stance or swing phase) the states of the three joints will be set depending on the phase (JC_STATE_ROTATING_START and JC_STATE_ ROTATING _END).

JC_Task Function

The JC_task is the second cyclic process implemented in a state machine (Fig. 6.). Apart from the stance and swing phases known the Master, additional ones which are used in local control are introduced.

In each state the actual value is compared to the value of the corresponding joint; the movement stops when the set point is reached and the new parameters for the next state are load:
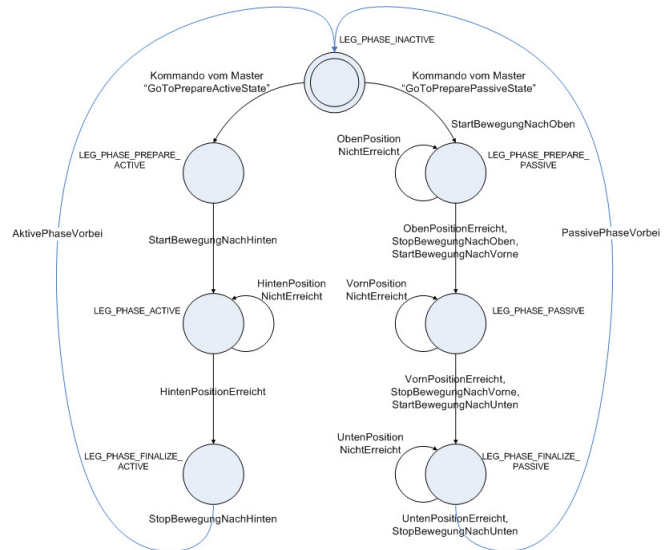
Fig. 6. State machine of the JC_Task Process.

In each state the actual value is compared to the value of the corresponding joint; the movement stops when the set point is reached and the new parameters for the next state are load:

- Direction of rotation - when loading a new state in eJointState - JC_STATE_ROTATING_START or JC_STATE_ROTATING_END;
- Turn Speed - when loading a valid (0 <= PWM <= 100) value in uJointRotationSpeed. Currently the speed is fixed to 100.

JC_JointStartRotating Function

This function is set by the input parameters specified joint with the previously loaded rotation and rotational speed in movement. Currently, the control is based on the principle Bang-Bang. This means that there are two discrete states of the control valves - on and off. But it is a controller using PWM (Pulse Width Modulation) provided. This allows the speed control. Driving the PWM signal to 0% means that the corresponding solenoid valve is closed for the entire period; 100% value means that it is open for the entire period. A value of 50% means that half the time it is open and other half period it is closed. The direction of rotation determines at which control valve (inflation or deflation) the PWM signal is created. Is the direction from the start to the end position the instruction is TRUE when the current value bigger or equal to the end value is

JC_JointTargetPositionReached Function

This Boolean function performs the comparison between the actual value and the value of the input parameters specified by the joint. It reads the actual value of the A/D module and compares it to the appropriate value (start or end position) in contrast to the current direction of movement. И. е., if the direction from the start is toward the final position, then this function turns to be TRUE only if the actual value is > or = of the end value. If the direction of the end is toward the start position this function turns TRUE only if the actual value is < or = of the end value.

JC_JointStopRotating function

This function has to stop the joint and is specified by the input parameters. The stopping is done by way of using of the PWM signal that promotes the appropriate one-or outlet valve to 0%.

IV. PRACTICAL IMPLEMENTATION

For the development the evaluation board EVBR8C20-23 was used; the implementation is done in the "C" language. For the compilation is used the HEW (High-performance Embedded Workshop), 4.02 version by RENESAS. Since it is IDE, it contains all the necessary tools:

- Compiler - to compile the software;
- Left - to the left of the compiled software;
- Flash Tool - for the program to be "registered" in the microcontroller;
- Run-Time Debugger / Emulator - to test the program in real environment.

In Fig. 7 the experimental test rig is shown. It includes he mechanics-the leg prototype; hardware – microcontroller with interfaces. The algorithms had also been tested.

Fig. 7. General view of the leg with the control.

V. CONCLUSION

Based on the implementation of control algorithms has been shown how using a dependency analysis a process model can be created that forms the basis for the implementation of a real-time system. Using the example of algorithms based on fixed-point arithmetic has been shown how the control algorithms can be implemented efficiently and predictably over time. In the present case a calendar-based scheduling model could be used. By means of case consideration and maturity provisions the real-time capability of the implementation could be shown.

Based on the achieved results the identified approaches can be applied for further research work. The control architecture is complex and only manageable with appropriate and identical design methods.

Currently, the control is based on the Bang-Bang principle.

Further experiments propose the implementation of the discussed PWM module depending on the pressure within the muscle and the joint's position. This would allow certain synchronization between all three joints in real-time.

Another advantage of the system is the open possibility for including reflexes.

REFERENCES

[1] S. Cordes, K. Berns, "A Flexible Hardware. An Architecture for the Adaptive Control of Mobile Robots, 3rd Symposium on Intelligent Robotic ystems '95, 1995.
[2] http://www.ai.mit.edu/projects/leglab /robots/ robots.html.
[3] Waldron, Kenneth J., "Machines That Walk: The Adaptive Suspension Vehicle", The MIT Press, 1989.
[4] K. Berns, V. Kepplin, R. Miller, M. Schmalenbach: "Six-Legged Robot Actuated by Fluidic Muscles" In Proc. of the 3th International Conference on Climbing and Walking Robots (CLAWAR), 2000.
[5] V. Kepplin, K. Berns (September 1999) Clawar 99: "A concept for walking behavior in rough terrain", In Climbing and Walking Robots and the Support Technologies for Mobile Machines, pp. 509-516
[6] P. Gonzalez de Santos, E. Garcia, J. Estremera and A. Armada, SILO06: "Design and configuration of a legged robot for humanitarian demining", Int. Workshop on Robots for Humanitarian Demining,2002

Profibus Interface Based Connection and Actuation of the Servo-Electric and Pneumatic 2-Finger Parallel Gripper by Using of the Quick Release Gripper-Change-System Realized for the Fanuc Robot

Duško Lukač

Abstract—The paper gives an example of the technical solution for the connection of the two different types of the 2 -finger parallel gripper regarding their driving power, both used in one application process. The grippers used in the application are a servo-electric 2-finger parallel gripper with highly precise gripping force control and long stroke and a universal pneumatic 2-finger parallel gripper with large gripping force and high maximum moments. Both grippers used are connected via quick release Gripper-Change-System (GCS) and are controlled via control panel with integrated Profibus-DP master unit. The end-effector is mounted to the GCS typically by using an interface plate designed by the user. The realization of the application is specifically designed for the Fanuc robot ARC Mate 120iB and the controller R-J3iB and represents the unique technical solution, not designed with the named parts and control unit in such way before.

Index Terms—Profibus, Robot system, Gripper, Quick Release Ripper-Change-System, FANUC.

Fig. 1. Top view on the robot cell.

Furthermore the solution has to fulfill the requirements of the modern industrial robot cell in order to enable the trainees to seamlessly be able to undertake the sophisticated engineering tasks in working environment.

I. INTRODUCTION

THE technical realization of the connection of the servo-electric and pneumatic 2-finger parallel gripper via quick release gripper change system for the FANUC robot ARC Mate 120iB and control unit R-J3iB [1] and in the paper described control of the system by using the Profibus-DP, is a part of the degree dissertation supervised by the author [2] aiming the construction of a robot training cell for Rhenische Fachhochschule Köln gGmbH - die University of Applied Sciences. The robot training cell serves the education of the university's students as well as the external customers who are trained at the university in the scope of the various courses offered by the university. The construction of the robot cell is presented in the Fig.1.

D. Lukač is with Department of Mechatronics, Rheinische Fachhochschule Köln gGmbH - University of Applied Sciences, Vogelsanger Strasse 295, 50825 Köln, Germany. Phone: +49-221-5468759, Fax: +49-221-5468755, e-mail: lukac@rfh-koeln.de.

II. DESCRIPTION OF THE SYSTEM COMPONENTS

All relevant system components used for the realization of the mentioned task are covered in greater detail below and give the reader a necessary basis for the traceability of the function of the realized system.

A. Robot system

The base of the FANUC robot system consists of three main components: robot, switch board and hand operating device. According to the DIN EN 775 standard in conjunction with DIN EN ISO 8373 the safety fence is also treated as a part of the robot system. Without the safety fence, which is designed according to the operating modes T1, T2 and automatic mode of the robot controller, robot system may not be put into operation. The control of the power engine for the robot axes is built up in the switch board. An automatic process originates from the programming of the robot movements in combination with the operating modes. The isometric view of the robot is presented in the Fig. 2.
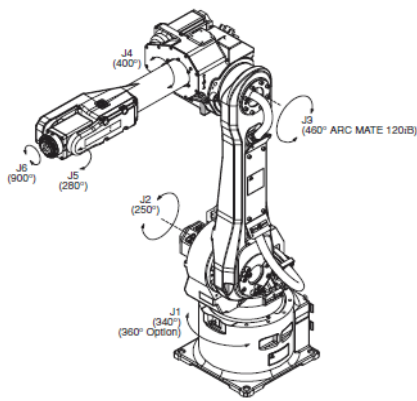
Fig. 2. Isometric view of the ARC Mate 120iB.

The ARC Mate 120iB series is 6 axes, electric servo-driven robot designed for precise, high-speed welding and cutting. Based on the simple and reliable construction, the ARC Mate 120iB provides accurate and consistent path performance necessary for welding and cutting. The R-J3iB controller and integrated so called Arc Tool software, provide reliable performance with high productivity. In connection with the standard VDI 2861 Part 1-3 [3] (DIN EN ISO 8373) J1 to J3 are the main axes and J4 to J6 the hand joint axes of the robot. Behind the axes-marks in the Fig.2 there are data about the robot motion range, necessary for the determination of the workspace and the toll-workspace. The tools are mounted in the gripper flange which can be flexible integrated and exchanged according to working step. ARC Mate 120iB has 1667 mm reach and 1282 mm stroke. There are permitted 20 kg load on faceplate. In the T1-mode of operation the safety fence (safety door) figured out in Fir.1 is deactivated and the tool center point and tools flange can be moved only at a maximum speed of 250 mms/sec. In this mode the operator writes the suitable robot program and he/she can test the single robot movements and stored program sequences at low speed. In the T2-mode security fence is also inactive. A program can be started only from the operating device (robot control hand-panel) and compared with T1 mode it can be proceed with the maximum speed. The T2-mode is used to test the program with the actual tools road and the actual cycle time. In the automatic mode the function of the security fence is activated. The persons must according to the security rules, to leave robot cell. While opening the door the robot stops. By using of the operating panel placed at the robot control unit, the hand operating device or an external device, the program sequences can be started at the planned speed.

B. Electric 2-Finger Parallel Gripper PG 70

The electric 2-Finger Parallel Gripper PG 70 [4] can be used universally. It is very flexible gripper for great part range and sensitive components in clean working environments. The gripping force control is possible in the range of 30 - 200 N. Because of the adjustable force range it can be used for the sensitive gripping of accident-sensitive work-pieces. The gripper has a long stroke of 70 mm for versatile work-piece handling. The power electronics and the control unit of the gripper are fully integrated in the gripper case. It allows the

creation of a decentralized control system. The gripper has a flexible actuation options for simple integration in existing servo-controlled concepts via Profibus-DP, CAN bus or RS-232. The 2-Finger Parallel Gripper PG 70 is presented in the Fig. 3.
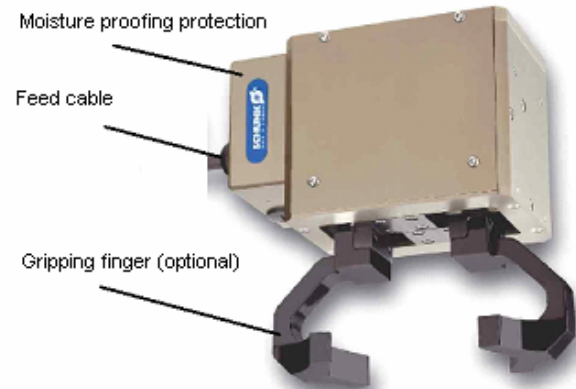
Fig. 3. Electric 2-Finger Parallel Gripper PG 70.

For the communication via bus-system the so called SMP - SCHUNK Motion Protocol - is used. This enables the creation of the industrial bus networks, and ensures easy integration in control systems. The gripper is actuated by brushless servo-motor (24V) who drives the ball screw by means of the gear mechanism. The rotational movement is transformed into the linear movement of the base jaw by base jaws mounted on the spindles. The dependence of the gripping force of the finger length is presented in the following figure.
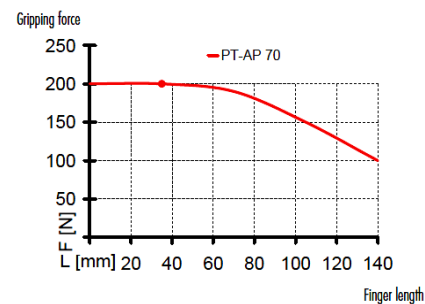
Fig. 4. PG 70 gripping force in dependence of the finger length.

C. Pneumatic 2-Finger Parallel Gripper PGN-plus 80

This gripper is actuated pneumatically, with filtered dry, lubricated or non-lubricated compressed air (10 μm) [5]. Requirements on quality of the compressed air according to DIN ISO 8573-1: 644 have to be fulfilled. Working principle of the gripper is based on Wedge-hook kinematics. It is a gripper with large gripping force and high maximum moments thanks to multiple-tooth guide and it can be used universally in clean to slightly dirty environments. Because of the high maximum load capabilities gripper is suitable for the use of long gripper fingers. Air supply occurs via hose-free direct connection or screw connections for the flexible supply of compressed air in all automation systems. It allows also integration of the comprehensive sensor accessories, like e.g. MMS magnetic switches for diverse monitoring tasks and stroke position monitoring – e.g. definition of the permitted / non-permitted range. Such magnetic switch is also integrated in the realization described in this paper. The recommended

work-piece weight is calculated for a force-type connection with a coefficient of friction of 0.1 and a safety factor of 2 against slippage of the work-piece on acceleration due to gravity. Considerably heavier work-piece weights are permitted with form-fit gripping. The 2-Finger Parallel Gripper PGN-plus 80 is presented in the Fig. 5.
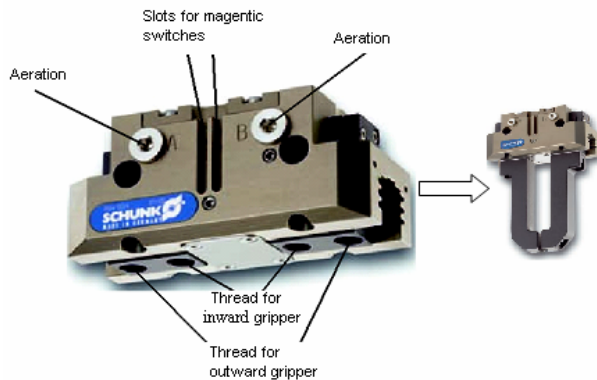
Fig. 5. Pneumatic 2-Finger Parallel Gripper PGN-plus 80.

The dependence of the gripping force (arithmetic total of the gripping force applied to each jaw) of the finger length is for the case of outward gripping presented in the Fig.6.
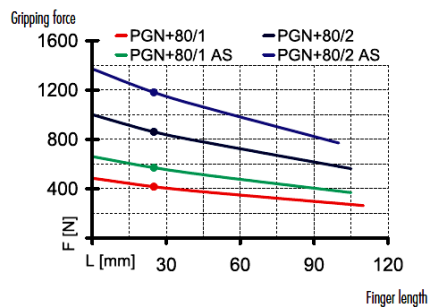
Fig. 6. PGN-plus 80 gripping force in dependence of the finger length.

With nominal air pressure its closing gripping force reaches up to 415 Newton. Its maximum heave is limited to 16 mms. In order to actuate the pneumatic gripper the 3/2-direction control valve cartridges, which are equipped with throttle check valves, are used. Two 3/2-direction control valve cartridges with the nominal wide of 1.5 millimeters are actuated electrically.
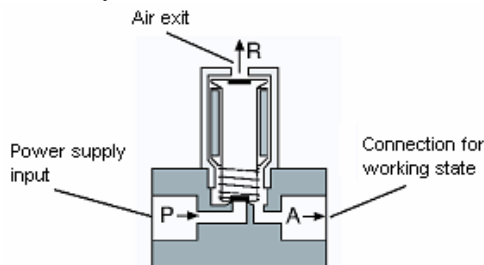
Fig. 7. 3/2-direction control valve.

As figured out in the Fig.7, in the currentless state the spring closes the power supply input P and the connection for working state A is bled via the air exit R. If the currency is switched on, the connection for working state A is connected with the power supply input P and the air exit R is closed. To influence the speed of the closing and opening of the gripper,

a throttle check valve at the exit A of the 3/2-direction control valves is to be adjusted.
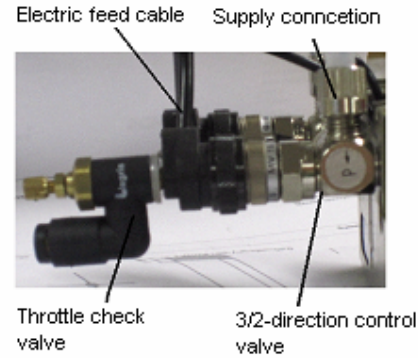
Fig. 8. Realized pneumatic actuation device.

D. Electro-Pneumatic Gripper-Change-System SWS 21 and the Quick-Change Rack

Aluminum built Quick-Change-System (QCS) SWS 21 consists of a Quick-Change-Head (QCH) and a Quick-Change-Adapter (QCA) and it is used to carry out a change of the end-effectors (tools) with the different driving power, as e.g. electric and pneumatic. It builds the connection between robot flange and the gripper. The connection assembly transmits electrical signals over the 19-pole connection pins. QCS uses patented self-retaining locking system for a safe connection between the QCS and the QCA. The QCH, mounted onto the robot, couples up the QCA mounted onto the tool. A pneumatically driven locking piston ensures that the connection is secure. After coupling, pneumatic and electric feed-throughs automatically supply the robot tool. In the event of a drop in air pressure, the locking piston is held by the cylindrical part of the locking piston. The Quick-Change-Rack (QCR) is used for to support the tools. The tolls can be laid down on the QCR. The storage plate is either mounted onto the mounting block or on the 3 or 4 position adapter.
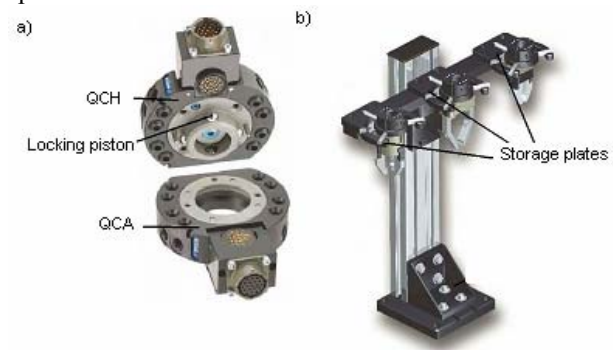
Fig. 9. a) Quick-Change-System and b) Quick-Change-Rack.

In order to control the docking and undocking the QCH and QCA as well as the actuation of the air supply, so called ganged valve is used. Ganged valve consists of three 3/2-direction control valves. Laterally the baffles are fixed. The LED display shows the respective valve which is active. The wiring of the road valve cartridges lead to a 12-pole connector.
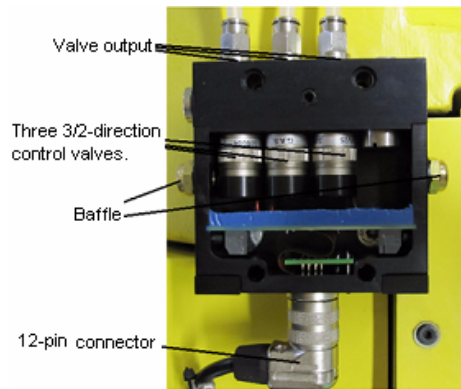
Fig. 10. Connected ganged valve.

1) Operating device - Multi Panel 277 8"

For the communication between the electrical gripper and the control unit via the Profbus-DP, the new operating device Multi Panel 277 8"(Siemens) [6] is used. It has an integrated Profibus-Master function. The handling of the panels occurs through the keys fixed in on the control panel, as presented in the Fig.11. The respective program is presented on the TFT screen. At the side a slot for memory SD-Card is behind two USB interfaces, an Ethernet/LAN interface and RS-422 / RS-485 interface available. By using of computer with the WINAC, WIN CC flexible and Step 7 software an application program can be written and loaded in the control panel. From there the automation process can be steered and supervised.

Fig. 11. Multi Panel 277 8"(Siemens).

E. Profibus-DP Slave ET 200M

As a Profibus-DP slave system the ET200M [7] (Siemens) is used. The whole system consists of the interface module IM153-1, digital input and output component as well as of the counter component. With the interface module the single construction groups are connected and further connected up with the Profibus-Master unit. With the slip-on front connectors the construction groups can be extended. The signal construction groups are used to steer and evaluate the signal levels used. As a power supply the rectifier 24 V/5A DC is used.
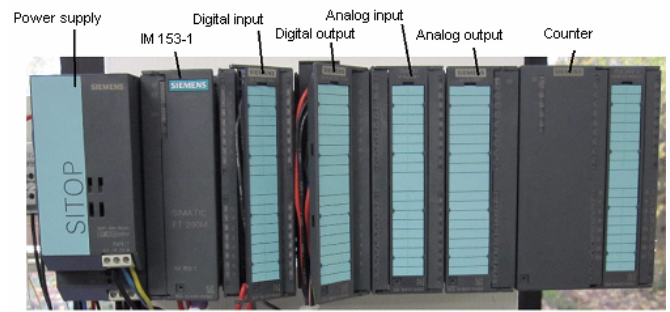
Fig. 12. Profibus-DP Slave ET 200M.

III. REALIZATION OF THE COMMUNICATION SYSTEM

To connect the mentioned devices presented, the communication system figured out in Fig. 13. has been developed, which connects all named components. The robot is programmed by using the FANUC R-J3iB control unit, which again actuate the 2-Finger-Pneumatic-Gripper PGN plus 80 via a quick Gripper-Change-System SWS21. The 2-Finger-Electric-Gripper PG 70 is controlled via Profibus-DP which, for the intact functioning, presupposes master and slave components [8]. Therefore the electric gripper is projected for the use via control panel MP277 (Siemens) and in panel integrated visualization system [9].
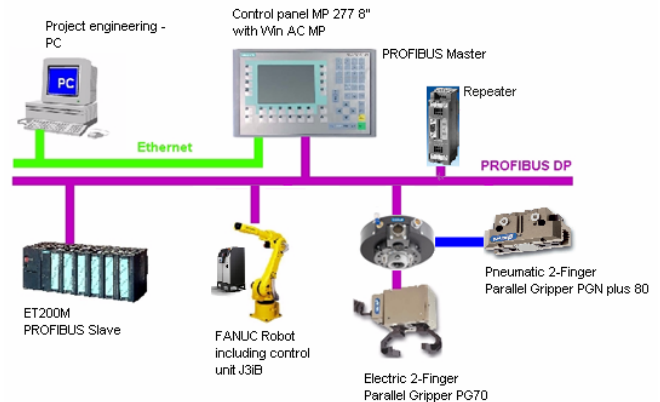
Fig. 13. Communication system.

The Profibus master must communicate on the other hand via the robot control unit R-J3iB with the electric gripper PG70, because the electric gripper commands are a parts of the robot program which needs to be written on the robot control unit. The commands for the robot movements are, because of the security reasons and the observance of modes of operation T1, T2 and AUTOMATIC, exclusively to be programmed via the robot control unit. In order to develop a functioning program for the control of the robot and the electric and pneumatic gripper over the control panel and robot control unit, following software components has been used: Step7 V5.4, WinCC flexible 2008 SP1 und WinAC MP 2008. These products of the Siemens company were selected because they are used very often in the German and international industry. The software Step7 is used generally to configure the hardware, for the parameterizing, to program the devices and to carry out diagnosis functions. The program

WinCC flexible is visualization software which is suitable for control panels. With WinCC flexible on the basis of the projected so called "screen blocks" and graphic objects, operating and observation of the device is possible. The software-control technology WinAC MP 2008 is based on an embedded system. It concerns a combination of the hardware and software which work together as a functional unit with defined tasks. The so called Soft-PLC contained in it, which works by using of operating system Windows CE which runs on the control panel, offers a graphic user interface (GUI) for the automation tasks. As a communication interface WinAC provides a so called Softbus. The configuration of the hardware begins with the integration of the system ET200M (Profibus slave device) and the operating device MP 277 (Profibus master device). Therefore project engineering PC is used, which is connected via Ethernet with the operating device.
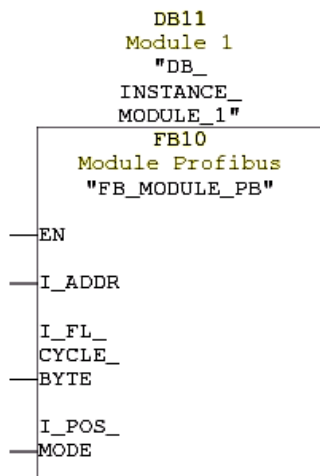
Fig. 14. Cut-out of FB10.

To actuate the PG70 electrical gripper, also manufacturer-specific function block, so called FB10 is required. To parameterize the inputs of the FB10 the EEPROM data of the module PG70 are required. These data are provided by the manufacturer. In the second step the GUI of Software-PLC is loaded on the control panel. In the last step of the system configuration, the FANUC robot system and the 2-Finger-Electric-Gripper PG70 are integrated in the configuration by using of the SIMATIC manager. To integrate the FANUC robot the manufacturer-specific General Station Description (GSD) file, is required.
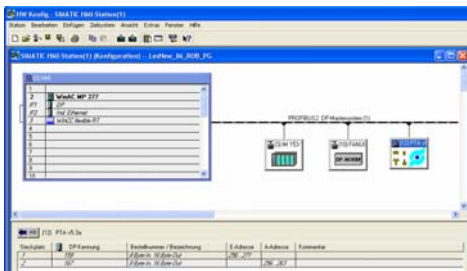
Fig. 15. Integration of the gripper in the data communication.

After the system configuration, the following graphical user interface appears and can be used for the control of the electric gripper.
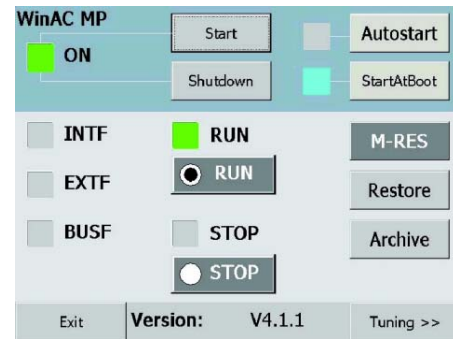
Fig. 16. Finished GUI.

The realized Gripper-Change-System is presented in the following figure.

Fig. 17. Gripper-Change-System in operation.

IV. CONCLUSION

Especially for the universities and other educational institutions, it is important to use equipment which enables technologically up-to-date education and the research projects in line with industrial requirements. Technical solution for the realization of the modern robot cell which is also in similar form used in the industry is presented in this paper. It can be used as a proposal for companies and universities to realize the same or similar solution.

IMPORTANT: The detailed description of the system as e.g. the configuration of the in-/ and outputs of the robot control unit, the setting of the tools-/and base coordinate systems, complete PLC program etc. is because of the limitation of the paper length not possible. Nevertheless, this information can any time be requested from the author. Please use author's e-mail address for the request.

REFERENCES

[1] FANUC, "SYSTEM R-J3iB Controller™", Avaliable: http://www.micromech.co.uk/dir_products/pdf/fanuc/r_j3ib_controller.pdf, February 2010.

[2] Maruszczyk, LT „Programmierung und Inbetriebnahme eines FANUC-Robotersystems mit Anknüpfung an eine Automatisierungsaufgabe (Programming and commissioning of a FANUC robot system and establishing of the automation process)", December 2009, Rheinische Fachhochschule Köln gGmbH- University of Applied Sciences, pp.2-179.

[3] VDI „Assembling and handling; characteristics of industrial robots; designation of coordinates" Avaliable :http://www.vdi.de/7899.0.html?&tx_vdirili_pi2[showUID]=90417, February 2010.

[4] Schunk "Electrical 2-Finger Parallel Gripper Universal Gripper PG70", Avaliable:http://www.schunk.com/schunk_ _ files/ attachments/ PG_70_En.pdf, January 2010.

[5] Schunk "PGN-plus80 Pneumatic 2-Finger Parallel Gripper Universal Gripper", Avaliable: http://www.schunk.com/schunkfiles/attachments/PGN-plus_80_En.pdf, January 2010.

[6] Siemens "Multipanel 277" Avaliable: http://aunz.siemens.com/NewsCentre/ProductReleases/Pages/IACPRMP277.aspx, February 2010.

[7] Siemens "ET200M" Avaliable: https://www.automation.siemens.com/download/internet/cache/3/1464409/pub/de/SIP-LUS_ET200M_A2.pdf, February 2010.

[8] Weigmann J. and Kilian G. Dezentralisieren mit PROFIBUS-DP/DPV1.Aufbau,Projektierung und Einsatz des PROFIBUS-DP mit SIMATIC S7 (Decentralize with PROFIBUS-DP/ DPV1/. Construction, project engineering and application of the PROFIBUS-DP with SIMATIC S7), 3rd edn, Siemens Verlag, November 2008.

[9] Siemens „Bedienen und Beobachten mit WinCC V6 - Modul_F05 Teil 1" (Serve and observing with WinCC V6–module F05 part 1), Avaliable:www.automation.siemens.com /fea/ftp/module/de/f05/f0-5wincc1.pdf,September2006,pp.2-193

Monitoring in the Control System of Robotized Medical X-ray Device for High Functional Safety

Milun S. Jevtić and Goran S. Đorđević

Abstract—**Robotized medical x-ray system must operate as a high safety device during its lifetime. Therefore the control system should include a safety monitoring module. One such safety monitoring module is described in this paper. The module design is based on the microcontroller with increased dependability. The main task of the module is to monitor the correctness of the tasks performances during regular or irregular operation. It accepts all the commands and all the signals from the sensors, safety components and from inverters, to detect possible dangerous events. By monitoring and by exchange of the messages the safety module also detects malfunctioning in each of the motion control components. In the event of a failure, the module activates the process to guide the x-ray device into the safe state. Altogether, the controller and the safety monitoring module provide fully reliable and predictable operation of the robotized x-ray device.**

Index Terms—**Control, monitoring, safety, dependability, robot, x-ray.**

I. INTRODUCTION

CURRENT trends in design of bulky medical devices for x-ray diagnostics are mostly relying on solutions developed for industrial robotics. Automated movements of heavy diagnostic tools such as x-ray tubes, collimators and bucky assembly reaching 100kg payload with sub-millimeter precision might be very useful in diagnostic procedures to replace presence of operator thus decreasing the level of accepted radiation and increasing the number of patients examined in the same time. An automated, preprogrammed movement of heavy medical equipment on the other hand rises a question of patient safety due to uncontrolled movements or collisions with objects in working area. This paper proposes one solution of this topic.

Global structure of x-ray device is given in [1] and corresponding block diagram of control system is given in Fig.1. This particular x-ray system has four degrees of mobility but in application it is a redundant 2dof system. It is designed to position and orient x-ray receptor, a bucky assembly, in a vertical plane while at the same time it aligns x-ray tube with collimator, which is source assembly, to it, allowing controlled distance between source and bucky.

The movements are produced with AC drives controlled with standard, low-cost inverters. Inverters are controlled digitally with standard PLC system. User interface is organized through touch panel and corresponding keyboards according to medical standards. It can be used for steering the unit into programmed positions in the factory or into the new positions stored during operation. Keyboards and touch panel are connected to PLC via multipoint RS485 connection. This connection is essential for commanding the motions controlled by PLC hence a Monitoring Safety Module (MS Module) is designed to monitor its healthy status. Its task is to ensure high functional safety of the system, i.e. its predictable and safe behavior even in the event of input error or malfunction in the control system. Therefore we have placed various sensors on the x-ray positioned to detect motion limits, collisions and failure of vital mechanical and electrical components. These sensors are not shown in the Block diagram in Fig. 1 but their function will be described in details later in the paper.

II. MS MODULE FUNCTIONING

The most important function of the MS module is monitoring of all processes that may impend the safe functioning of the device and navigating the system into one of the safe states defined during the design process. The MSM Module may function into two modes:
- Service mode, or S-mode,
- Functional Safety mode or FS-mode.

Entering the S-mode is allowed only to authorized personnel. In the S-mode service engineer may set up parameters of the system such as parameters for motion sequences, software limits of motions for each mobility axis, etc., and to start inherent procedures of interactive testing. Besides, the MS module does a safety monitoring in both of the modes of operation. However, in the S-mode it does permit motion beyond standard safety limits. This is to enable thorough testing of all hardware devices such as all limit switches, optical switches, bumper sensor, potentiometers, and force sensor for rope break detection.

M. S. Jevtić is with the Department of Electronics Faculty of Electronic Engineering, University of Niš, Serbia, 18000 Niš, A. Medvedeva 14 (corresponding author; e-mail: milun.jevtic@elfak.ni.ac.rs).

G. S. Đorđević, is with the Department of Automation Faculty of Electronic Engineering, University of Niš, Serbia, 18000 Niš, A. Medvedeva 14 (e-mail: goran.s.djordjevic@elfak.ni.ac.rs).
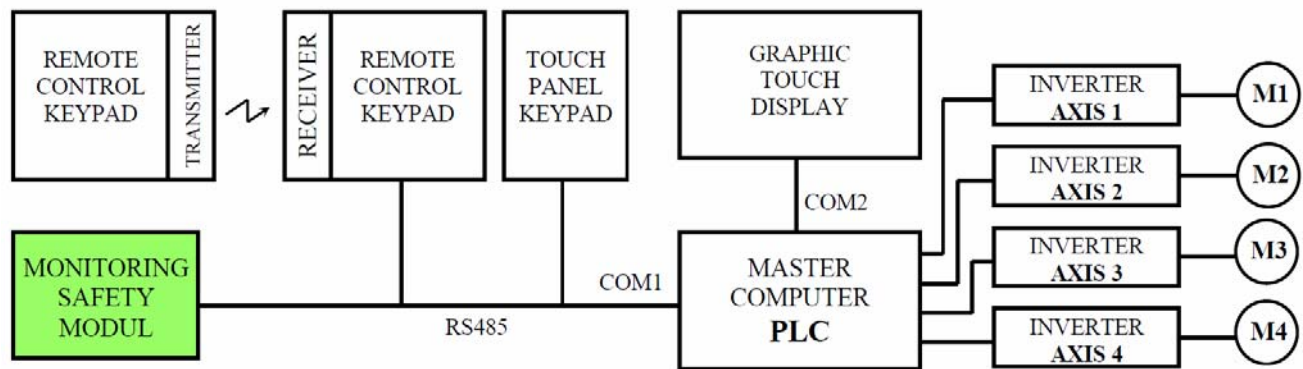
Fig. 1. Block diagram of control system in X-ray medical device.

The MS module in FS-mode gives high safety in the functioning of the x-ray positioning system through the following tasks:

- Upon power up it enables operation of the system i.e. overrides the Unconditional Stop (US) only after checking if there exist no single STOP condition.
- Monitors if all devices of the control subsystem are connected and properly functional via multipoint connection through perfect failure detector [3, 4]. This way we detect possible malfunctioning of the MS module and PLC control unit which are two vital components of the safety system.
- In periodic messages exchange the MS module recognizes motion command for each axis generated by PLC control unit and sends status word of the whole system from all sensors in the system and the correctness of motion outcome.
- Detects all hazardous events on time and undertakes proper actions to guide the system into the safe states.
- Generates US state for some hazardous events thus stopping all movements and override further manual commands from keyboards.
- Generates US state for some hazardous events thus stopping all movements and enables further manual commands from keyboards, if and only if hazardous event is not observed anymore.
- In the case of bumper activation event the MS Module stops the motion and it reverts the movement in the two axes of the system.
- Provides inherent self-testing procedures of the whole system.

III. MS MODULE STRUCTURE

The MS Module is designed as microcontroller system based on model of dedicated operative systems for real-time operation. Its architecture represents the block diagram in Fig. 2. It is based on microcontroller PIC 16F887 with integrated watchdog time and oscillator. This enables reliable detection of correct program execution as well as testing the watchdog timer itself. 24 digital inputs with optocouplers are grouped into three groups with the possibility of using separate power supply for each group. Nine DI can generate CPU interrupt

with their active state. Conditioning of analog signals is also designed. They handles four analog signals from positioning potentiometers and one from force sensor for collision detection. Full range of AD converter is engaged with customized reference voltage generated as Vref+ and Vref-, as well as referent voltage for force sensor and positional potentiometers. USART and RS485 drivers are used to establish communication channel with PLC. Power unit also supply voltage to digital and analog circuitry. The PCB design digital and analog circuitry is carefully located to minimize the interference of digital noise to AD accuracy. Two relay outputs are with Normally-closed and Normally-open contacts.

Serial connection of relay active contact and two passive contacts of the Emergency Switch (ES) we define so called
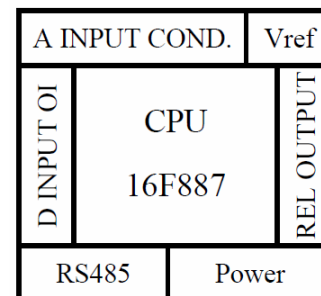
Fig. 2. Block diagram of MS module hardware.

safety loop which deactivates power supply to motor inverters. Active contact of the other relay output is used for power supply needed to deactivate electromagnetic brakes for all mobility axes. The MS module activates relay outputs thus enabling motion further controlled via PLC DO module, but only upon:

- Successful self-initialization,
- Establishing the communication with PLC,
- No active input demanding STOP action exists,
- Checking if a previous hazardous action did not produce persistent STOP condition requiring only service personnel for recovery.

Sensors used in this system are purposefully chosen. In the case of contact loss in wirings and connectors, or power loss, or sensor malfunction, the MS Module reverts to excess

situation assuming the motion should be prevented until service personnel overrides operator limitations.

The MS Module software is designed so to follow strict timing conditions. The communication is handled via interrupts and threads activation when a message is accepted in pre-specified timing interval. In periodically activated threads we handle groups of sensors, while those sensors that may result unconditional STOP are handled with highest priority.

IV. PLC TO MS MODULE MESSAGE EXCHANGE PROCEDURE

The message exchange between PLC unit and other slave units connected to a common half duplex communication channel is based on message sending from PLC as master unit and on reply from the slave units in specified time interval.

Basic message the MSM receives periodically every T_{mes}=100ms is shown in Fig. 3. The beginning of the message starts with byte 0xFF, that cannot be part of the message, except at the end of the message as CRC code for error correction. This does not interfere correct detection of the message beginning as the byte 0xFF can be repeated several times. The message gives status information on axes movements. Based on that, the MSM validates motion correctness. One STOP/ START enable bit per axis marks the status of the motion per each axis thus leading to motion disable/enable signal to the inverters. This is not to be confused with safety loop STOP action in the case of emergency or Emergency Stop button activation.

If after time out T_{out} > T_{mes}, the MSM does not receive message from the PLC unit, all movements are disabled activating the STOP command. Upon the new message arrival the system functioning is enabled. Two consecutive errors in transmission-reception are detected as CRC Error and loss of communication is declared. In this case all of the movements are disabled and the system is navigated into STOP state.

The response of the MSM to each received message from the PLC unit follows the completion of the reception and shout timeout for line revert. The structure of the reply message is shown in Fig. 4. The message embodies limit switches status as well as software limits status and other errors detected during operation.
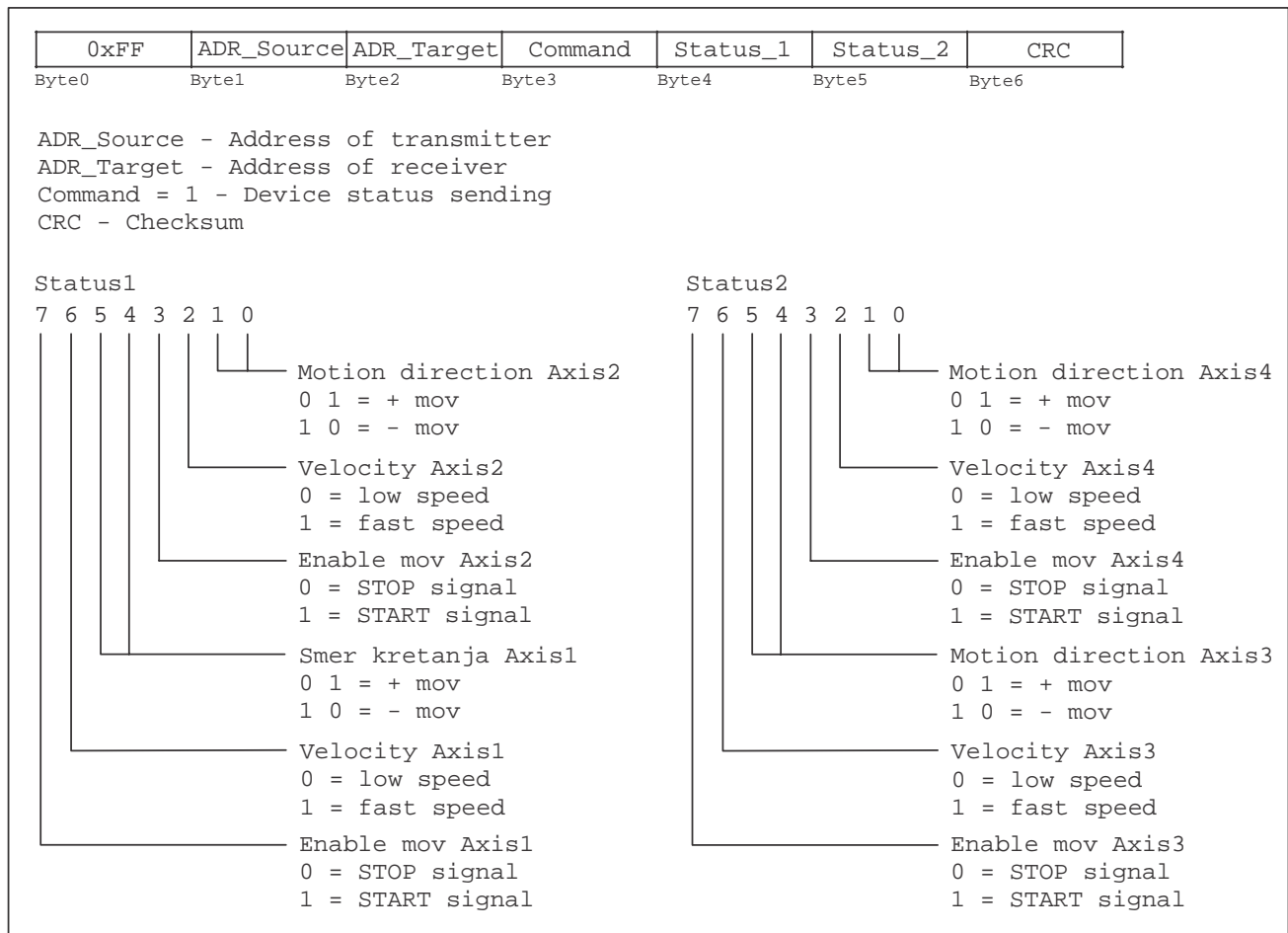
Fig. 3. Structure of PLC to MS Module Message.
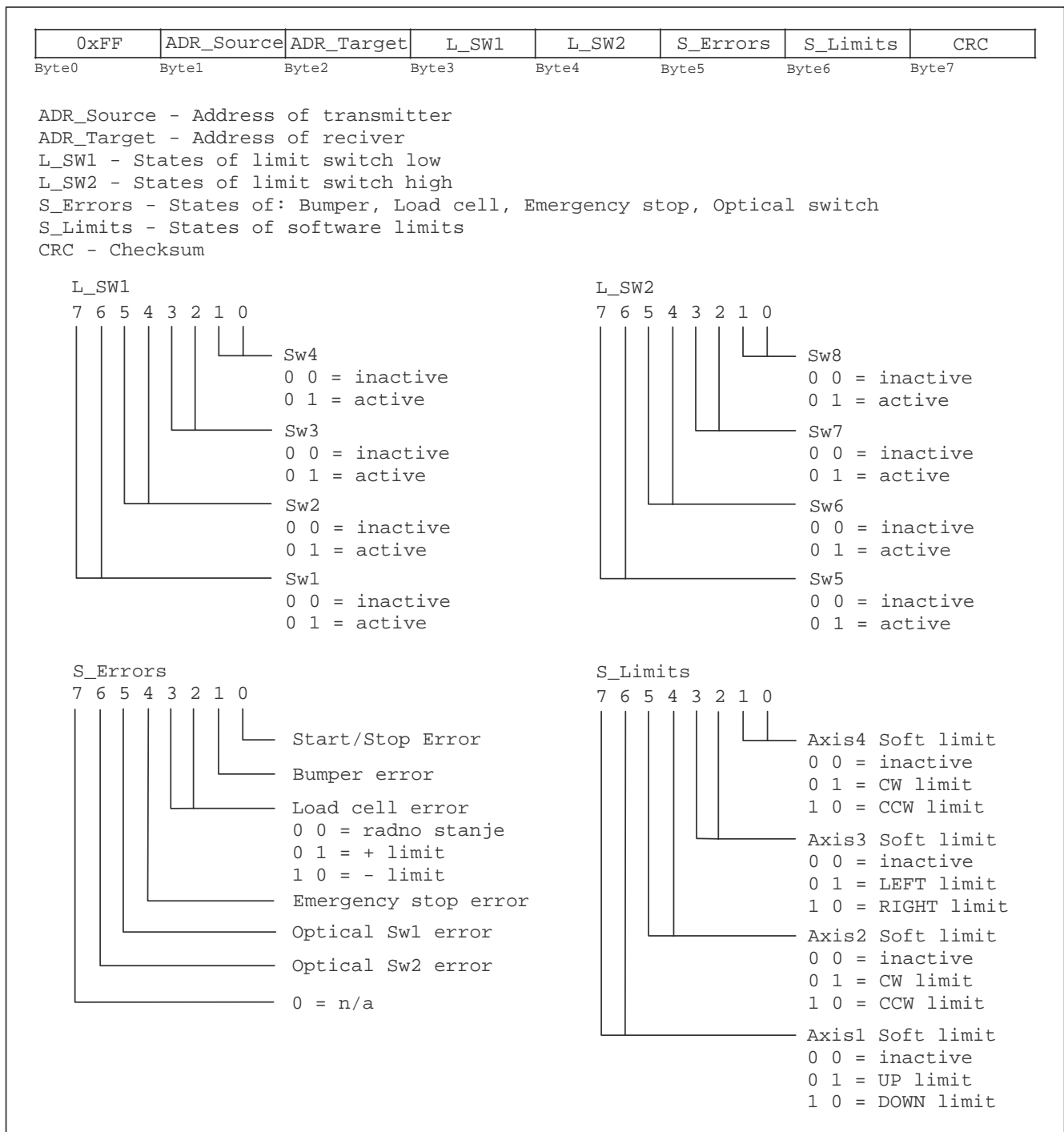
Fig. 4. The MSM to PLC Reply Message.

V. ERRORS DETECTED BY MSM AND MSM ACTIVITIES IN THAT CASE

Sensors in the robotized medical roentgen device whose states are provided to PLC and MSM (**M**onitoring **S**afety **M**odule), are used to detect the errors and start the security activities as foollows:

A. *Limit switch errors*

If anyone of limit switches (*Sw1* to *Sw8*) is activated, the following MSM activity is performed:

➢ Unconditional safe STOP activated: OUT1_OFF, OUT2_OFF – all movements in system are suspended (the robotized medical roentgen device is stopped - system functioning is suspended by putting the releys outputs to off state);

➢ Refunctioning of the system is enabled by the service skilled worker.

B. *Start/Stop error*

This error appears if PLC has generated the command for the end of motion (MSM received the information through the

STATUS_1 and STATUS_2 that there is no motion) but still there is the motion. When MSM detects the move more than 1 cm after T*stopm* time (time to hold up because of inertia) after the end of move status is received, MSM starts the following activities:

➢ Unconditional safe STOP is activated – system functioning is suspended by putting the releys outputs to off state (OUT1_OFF, OUT2_OFF);

➢ Refunctioning of the system is enabled by the service skilled worker.

C. Bumper error

If the Bumper sensor is activated during the movement on *Axis_1* downward or on *Axis_2* in + direction (counterclockwise), PLC starts the inverse movement to safe position – back. At the same time, MSM reacts with following activities:

➢ Starts the timer Tbump (Tbump is the time needed for putting the robotized medical roentgen device to safe position – back by the movement in the opposite direction);

➢ If the bumper sensor is stil active after Tbump has passed, Unconditional safe STOP is activated – all movements in system are suspended;

➢ Refunctioning of the system is enabled by the MSM (Unconditional safe STOP is deactivated) when the Bumper sensor become inactive and there is no other STOP condition.

D. Load cell errors

The error is detected by comparing the state of the force sensor *Vr_FS* with the limit values.

➢ If Vr_FS < LDVr_FS is detected during the moving downward the Axis_1 and/or in – direction (clockwise) on the Axis_2 (low limit – minimal load with no colision and no rope break) with duration more than Tcoli (colision), MSM generates Unconditional safe STOP and sets the error Load_Cell_Error = 10;

➢ If Vr_FS < LDVr_FS is detected in any other situation with duration more than Tcb (rope break), MSM generates Unconditional safe STOP and sets the error Load_Cell_Error = 10 (rope unload);

➢ If Vr_FS>LUVr_FS is detected during the moving upward the Axis_1 (high limit – maximal load with no damage in mechanics), MSM generates Unconditional safe STOP and sets the error Load_Cell_Error = 01 (rope overload);

➢ The oscillations Vr_FS coused by starting and stopping the movement, or coused by other reasons, have no affect since they are in the range below the value limit;

➢ Unconditional safe STOP is deactivated (refunctioning of the system is enabled by the message fromPLC) if the condition that coused STOP doesn't exist anymore, and there are not other conditions that could activate STOP.

E. Emergency stop error

Activating the Emergency stop switch couses this error. MSM reaction is as follows:

➢ Unconditional safe STOP is activated: OUT1_OFF, OUT2_OFF – all movements in system are suspended (the robotized medical roentgen device is stopped);

➢ After the Emergency stop switch is deactivated, MSM cheks the state of the system. If no one sensor is active, i.e. there is no one condition to generate STOP, the functioning of the equipment is enabled – STOP is deactivated after received the message from PLC;

➢ If any of sensors is active, i.e. there is some error, system functioning is not enabled.

F. Optical SW1 error

If *Optical_SW1* is active, MSM reaction is as follows:

➢ After receiving the message from PLC, MSM analizes STATUS_1 and STATUS_2 to check if too low speed is established;

➢ If too low established speed is not detected after next received message (two successive), MSM activates Unconditional safe STOP;

➢ This STOP can be deactivated when Optical_SW1 become inactive and when there are no other conditions to activate STOP.

G. Optical SW2 error

If Optical_ SW2 is active during the movement of Axis_1 downward and/or Axis_2 in + direction (counterclockwise) MSM reaction is as follows:

➢ After time Tstopm activates Unconditional safe STOP (PLC stops the movement);

➢ This STOP can be deactivated when Optical_SW2 become inactive and when there are no other conditions to activate STOP.

H. Soft limits errors

If the positional potentiometer state is equal to the soft limit values or it exceeds the limit values for that axis, MSM reaction is as follows:

➢ Check in next received STATUS_1 and STATUS_2 if the movement is stopped (established to no move),

➢ If stopping the movement is not detected after next received message (two successive), MSM activates Unconditional safe STOP.

➢ If MSM detects the movement by the positional potentiometer state change for more than 1 cm after the time Tstopm passed from the Soft_limit detection, MSM activates Unconditional safe STOP,

➢ If the movement is stopped and there is no move after Tstopm, MSM doesn't make any action.

➢ If Unconditional safe STOP is activated, refunctioning of the system is enabled by the service skilled worker.

VI. CONCLUSION

Increasing hardware complexity in robotized medical devices for x-ray diagnostics inevitably means higher probability of hardware failure and corresponding functional

safety issues. We overcome this problem by complementary monitoring module for safety. This reduces chances for error and increases patient's security in the working area of the system. The functions of the MSM are designed to ensure reliable and always predictable operation of the system. All possible failures or combination of events are predicted and consistent actions are planned so to reduce the risks even in the case of errors due to mistakes in manual operation.

REFERENCES

[1] Svemir Popić, Srđan Mladenović, Goran S. Đorđević, "Final prototype of robotized x-ray device for medical applications", *Proceedings of INFOTEH-JAHORINA 2009*, Vol. 8, Ref. E1-9, ISBN-99938-624-2-8, pp. 824-828, March 2009. (in serbian)

[2] M. Božić, Miljan Milanović, "Control interface for universal x-ray positioner", *Proceedings of INFOTEH-JAHORINA 2009*, Vol. 8, Ref. E1-1, ISBN-99938-624-2-8, pp. 786-789, March 2009. (in serbian)

[3] Milun Jevtić, Bojan Jovanović, Sandra Brankov, Marko Cvetković, "One realization of fault detector in robot control systems", *Proceedings of INFOTEH-JAHORINA 2009,* Vol. 8, Ref. E1-7, ISBN-99938-624-2-8, pp. 814-818, March 2009. (in serbian)

[4] C. Fetzer, "Perfect Failure Detection in Timed Asynchronous Systems," *IEEE Trans. Computers,* vol. 52, No. 2, pp. 99-112, Februar 2003.

User Interface in Medical Information Systems – Common Problems and Sustainable Solutions

Tatjana N. Stanković, Petar J. Rajković, Aleksandar M. Milenković, and Dragan S. Janković

Abstract—As the other segments of society, healthcare delivery can be significantly improved having Medical Information Systems (MIS) as part of its IT infrastructure. MIS systems can be described then as one of founding blocks of efficient, well organized and reliable work of healthcare facilities. This is in theory, but in reality there are quite some cases when introduction of MIS downgraded business processes of medical institutions. These cases are usually related to poorly understandable and confusing user interface. This is particularly emphasized in the MIS employment phase, when users are not used to the new applications. Our research has shown that MIS developers have completely different view to the system than the end users. This fact leads towards serious problems during the adoption phase of MIS. Problems escalate when IT professionals try to apply some fancy interface to "improve" functionality of the system, rather than to follow the end- users' habits. Working on a project of developing MIS for Serbian public healthcare, we have tried one opposite approach – to make user interface as much is possible similar to existing documents and follow existing processes and documentation workflows. Having these two design postulates in mind, we managed to give some improvements in MIS development, which have already resulted with users' approval, and extremely reduced time needed for their training.

Index Terms—Electronic Health Record, Medical Information System, user-centered software development, user-interface design approaches.

I. INTRODUCTION

DURING last decade of 20th and at the beginning of the 21st century enormous efforts are done in the area of implementing and using modern information systems all over the world. Information system design approaches, architectures, developing methodologies and technologies are constantly improved and upgraded during mentioned period.

T. N. Stanković is with the Faculty of Electronic Engineering, Aleksandra Medvedeva 14, 18000 Niš, Republic of Serbia, e-mail: tatjana.stankovic@elfak.ni.ac.rs.

P. J. Rajković is with the Faculty of Electronic Engineering, Niš, Serbia, e-mail: petar.rajkovic@elfak.ni.ac.rs.

A. M. Milenković is with the Faculty of Electronic Engineering, Niš, Serbia, e-mail: aleksandar.milenkovic@elfak.ni.ac.rs.

D. S. Janković is with the Faculty of Electronic Engineering, Niš, Serbia, e-mail: dragan.jankovic@elfak.ni.ac.rs.

Information system covered all areas of nowadays world and made many business processes more effective than they ever been. Medicine could be just another field of successful implementation of information systems, but this mission turns not be so easy. Adoption of medical information systems (MIS) was a process that failed many times from many different reasons, from to-complicated architecture to user interface that is not sufficient for medical professionals. This paper presents our results related to user-centered approach of development of MIS system user interfaces.

Luckily, today, medical professionals' leading view is that MIS systems became a necessity for healthcare system in modern society. MIS systems offer wide variety of different functionalities related to healthcare delivery process – from simple document management to complex decision support systems. In more developed countries this kind of science has reached advanced stages of researches, such are preoperative risk predictions [1], or biosignal-based systems for different kind of patient's monitoring [2], but in Republic of Serbia we are at the first stages of introducing and developing of MIS systems yet. A lot of healthcare facilities use only a part of MIS, which is related to recording given medical services and consumption of medical materials, and generating reports needed for government's health insurance agency and public healthcare insurance fund ("*Republički zavod za zdravstveno osiguranje*" on Serbian).

In our project (Improvement, integration and collaboration of information systems of medical institutions, TR13015), which is supported by Serbian Ministry of Science and Technological Development, we have tried to develop much wider and comprehensive approach. MIS we have developed is intended to record not only basic information about given medical services (who did it, what was done, and how much does it cost), but all relevant medical information about medical examinations, therapies, treatments, hospitalizations and other documents that make complete medical history of the patient, or shortly, complete Electronic Health Record of the patient (EHR) [3]. Additional advantage of MIS is that such information system in health care greatly accelerates the process of generating the voluminous documentation that follows all the steps done in any of health services. Example of mentioned documentation is reports for other government institutions which are based on the provision of health services, and reports for the management of health institutions themselves. Data access is facilitated and accelerated in the

sense that they can be accessed from multiple locations simultaneously, and not for each episode of treatment to be performed a physical search of impressive archive of these institutions.

However, it was proven around the world that the introduction of wide software systems in health care has its negative side also [4]. MIS users, especially older ones, have deeply established routine in their daily work, and every novelty can be disruptive to them. Also, many doctors literally do not trust to computers. They are not sure if entered data will be really stored. Also, they doubt about privacy of entered data – which will have access, who can use then for which purpose etc.

Medical professionals usually have to deal with several electronic systems during their work (ultra-sound devices, EEG, Roentgen, etc), which are often provided by different manufacturers [4] and having different user-interfaces. In the period of introducing and implementing MIS (which should act integrative system for all the other electronic and computer systems) to health care facilities especially, it can slow down their working process instead of speeding it up. When a problem occurs with using the software tools, to us as developers, it is often the easiest to blame non-IT professional users, but is it only and real reason for such situations? Or maybe a different approach in the design and implementation of systems could contribute that such situations do not occur or be reduced to minimum?

This paper deals with problems that MIS users have or can have with non user-friendly interface. Section two briefly describes these problems in the way we have tried to classify them. The rest of the paper is dedicated to our approach and our solution to this problem, which gained to results. As one set of problems cannot be bound only to MIS users, but is universal, described solutions can be applied to arbitrary information systems, as well.

II. END USERS AND THEIR MAIN PROBLEMS WITH MIS

Users of information systems in health care, beside administration that can be met in every area of one society, are usually doctors and nurses. Administrative staff use IS modules like evidence of employees, financial accounting, accounting earnings, material assets, and similar. EHR modules are used only by doctors and nurses, according to the law of patient's data privacy [5].

In general, in relation to the use of application modules, we can define two main groups of users:
- Users that most of their work spends using only software tools.
- Users who are dedicated to clients (patients) or some other electronic systems, and only part of their work spend using software.

Doctors and nurses belong to the other group of users. Their daily work must be dedicated more to the patients' treatment and less to the information system. Let us consider the fact that they are confronted with several different

electronic systems, usually provided by different manufacturers, and in our country entirely never integrated with the information system. Additional difficulty is that they are strongly used to paper evidence in Serbia for many years. Working on the MIS development, on the basis of multiple interviewing medical staff employed at the Ambulatory Health Center of Nis, and the Clinic Center in Nis, (Department of Child Internal Clinic and Clinic of Neurology), we have attempted to categorize their current problems, and issues they could have in working with parts of the medical information system:
- Windows or web forms for inserting and editing data are endless.
- Lack of descriptions and ranges of normal values on the form
- Users find themselves "lost in application". When the functionality of the medical process is such that it demands entry (or choice) of a large amount of data, and more than one windows form is opened, and more than one "save" action is necessary, users after a while don't know where they are, or what they have recorded yet, and what to do next.
- "They lose a patient." If system demands moving patient from one list to another many times during the examination, one wrong mouse click and patient is completely "lost" in the system.
- The layout of tabs on the form is inadequate in terms of monitoring the natural process of entering data in a commonly used scenario.
- Search for right value is slow and endless. Combo boxes contain hundreds or thousands of values; too much of the working time is lost for searching.
- Some data is entered more than one time in the system.
- Too many rows lost because application did not ask the user: "Are you sure…" and the wrong mouse-click were fatal.
- Repeating of the same or similar actions several times in the working time. There are situations when user acts the same many times a day (like injections to the patients) and yet, he or she need to enter the same information every time again, just for different patient, because system demands, and many other.
- Scrolling up/down and scrolling left/right are too frequent.
- Suggested values are not properly spelled (especially in Latin sentences)

III. STEPS TOWARD SOLVING THE PROBLEM

Problems like described are detected not only in Serbia, but in the west Europe countries, as well. According to the researchers of the *Smart Transplantation Project* in *German Research Center for Artificial Intelligence (DFKI),* like it can be found in [4]: "More than 30 staff members of the Department of Hematology and Oncology at the Heidelberg University Clinic participated in an online survey which asked about various areas of application of Information and Communications technologies (ICT) within the hospital. 94%

of those asked responded that IT applications are critical to the daily routine at the clinic and 90% said more than 50% of their work involves the use of computers; 58% even reported more than 75%.

Important criterion for the respondents was not only a timely system response but also that the system be efficient and user friendly. The responses were ambivalent concerning the current state of integration of the IT applications in the daily work routines." Information as listed are not flattered for designers and information system developers at all. Without the strong cooperation of the development team and future users of software systems it is difficult to expect that the project will result in a satisfactory user interface. Our research project and development in this direction gave some results as this paper presents. The concept "From the conversation to the user interface" in the steps shown in Figure 1, resulted in mutual satisfaction of us and our users, both. The third step asks for attention, because it is the step that can save a lot of time to developers in the further designing.

IV. DESIGN OF INTERFACE

Addressing the second and third activity of the diagram shown in Figure 1, we have noticed that the medical staff deals with enormous paperwork. Usually, they need to enter data at least twice – once in patient's paper based health record and in institution's log book. However, they are very used to it, and they know in advance what paper form to fill and how to fill it, like they could do it with their eyes closed. We wanted to help users to improve process of entering data and help them to avoid inserting same data more than once. Critical point here is that medical staff members can be slowed with MIS compared to dealing with paperwork only. Main reason for this potential problem is that MIS users are usually slow-typers, and they need significant amount of time to type (instead of handwrite) different documents. So we came up with the idea that the patient's electronic health record should look the same or very similar to the paper based or the parts that cannot be fully copied should at least have the same layout of fields as in the paper document. Also we offer as-type-complete functionality for all entities that are described with codes and names – diagnoses, medicaments, standard documents, etc.

Instead of adjusting the form interface to the functionality, we have scanned paper documents, and planted them to the windows forms everywhere we could. One example, where it was possible to adjust interface in a great deal to paper, is shown in Figure 2. Figure 2a represents paper patient record that health workers operate dozens of years with. Similarity to the electronic form of the main page of patient record, which is shown in 2b, is obvious. Figure 2a shows front page of paper based patient health record. This record is an envelope consisting of four pages where each page contains some general medical data about patient – immunization statuses, common diseases, chronic diseases, findings on annual medical examinations, main health risks, information on

allergies, etc. Each page is represented by one tab looking exactly as corresponding page. Also, tabs have exactly the same sequence as the sequence of pages inside patient record. In the cases when it was not possible to provide exactly the same design in the electronic forms, we have tried to contain the layout of fields, like shown in Figure 3a and 3b. Here we tried as much is possible to follow paper document.
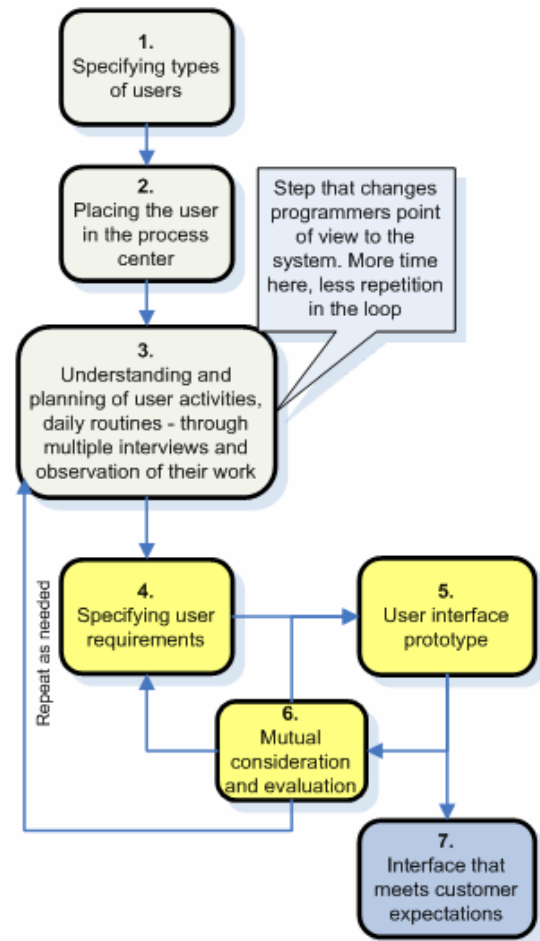
Fig. 1. The interdependence of human-centered user interface activities.

The result of this approach to designing the user interface was more than satisfactory. User's resistance to the new software was minimal, and they needed no explanation of windows forms for EHR. Another important moment in understanding user activities was a job routine and medical documentation workflow. Routine work with software is gained easier if it is similar in different functionality. For this reason we decided to follow the one and the same standard for every man-computer interaction. Unique ways for search data is used everywhere, to enter, read and delete data, etc [6].

After each action the recording of data in the database is provided, according to the research that showed that users often lose control of where they are in the application. Deleting is not permitted to all users, but it is in accordance with privileges. The time (on server) when the item is added is examined whenever someone tries to delete it. Time after which the removal is still allowed on the server is adjustable

[5]. Upon expiration of the time (the time seen as a time in which they can correct random errors) all changes are recorded (the old value, new value, who made changes and when). So the possibility for user to accidentally delete item is minimal.

Fig. 2a. The first page of patient's paper record, for preschool children.

Fig. 2b. The first page of EHR for preschool children.

Another important goal in EHR design phase was not to let user enter arbitrary data, but to choose between offered values whenever it is possible. Classical windows search through controls like combo or list box is exactly what our research showed that users complained to. For example, last catalog of diagnoses (standard MKB10) contains exactly 14193 different diagnoses. General practitioner (GP) has to have all diagnoses available for choosing. Can you imagine popup of 14193 items for choosing the right one? This subject has different approaches among designers worldwide. Some of them use the concept of giving only few dozens of most used diagnoses in the late period [7]. This approach, however, can signal to the doctor what diagnoses or therapy to determine, or what facility for hospitalization to recommend. To avoid that, and to let doctors rely on their own knowledge, but to provide them quick choice of items like diagnoses, drugs, facilities, medical materials, we have developed our own Search component which is applicable to any kind of catalog data.

Fig. 3a. The inner part of paper record, for recording diagnoses, therapies, dates, etc. during the visit.

Fig. 3b. Tab for visits. Double click on every cell opens modal form for recording proper medical data.

Fig. 4a. User typed three characters of the medication code and 11 coresponding medications have appeared for choice.

Fig. 4b. Choosing diagnoses in exactly the same way, only by typing the beggining of its name instead of code.

Starting with a fact that all catalogues are similar as entities, that they usually have the name and some kind of code for every item, we have made searching through 3 attributes (which are configurable). Every catalogue is modeled with a database table. Search component is independent and it links to a table. It addresses database after the third typed character (third is default, but it's configurable), and gather appropriate dataset, which is usually consisted of few dozens or only few items. Filtered items are shown under edit boxes, and user can easily, using mouse or keyboard arrows, choose proper value, or he can keep typing and narrow the selection to one or two items. The examples of searching values through our component are shown in Figures 4a and 4b.

Performing the same search process for every catalogue in all modules, we provided a kind of introduction of user applications in the daily routine and getting used to working with the system quickly. Another important item that we have avoided by this approach, and concerns the efficiency of the system, is the congestion that can occur when hundreds of concurrent users search through the same catalog in the database. Because the filtering is done after the third key typed, dataset that server returns to the client is consisted of ten or twenty records, the traffic in the network is greatly reduced compared to constant loading of entire catalogs.
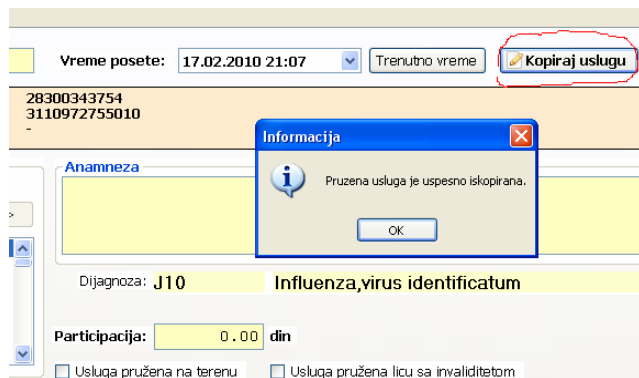
Fig. 5. The possibility of copying data for given service together with medical material, for giving injections.
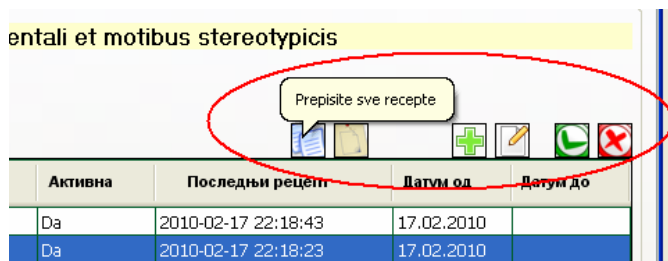
Fig. 6. Accelerated prescription of recipes for chronic patient.

In the choosing doctor module (in Serbia in the last few years, each patient selects his own doctor and make a contract with him), this component is used for the selection of doctors for whom the patient wants to make a statement. Since this function at the Health Center in Nis is made by nurses, they have to perform a search among the hundreds of physicians of this institution. However, with our module and described way of search through catalogs, their work in the recording patient statements proved to be easy and fast, without errors, and what is most important - do not create waiting lines at offices. According to the our research that users complain in the sense of repeating the same actions more time in a day, and having to enter the same data for insurers again, we have provided them *Copying of done actions* through user interface. Figure 5 shows Copy button for recording of given medical service, which is on our country an obligation of every health care facility.

Good example of copying actions is related to the patients with chronic diseases. They (especially older ones) come again and again to get the same or similar therapies from general practitioners. So we have provided our users (in this example only if they are GP) with a possibility to copy prescriptions, if the patient was marked as chronic one. With one mouse click through user interface, therapy is shown in the EHR, and doctor further has 6 different possibilities, provided through 6 buttons in user interface, described as follows from left to right (Figure 6): copy all medications, copy only selected one, add some therapy, change selected item, activate or deactivate selected therapy. Therapy is defined as permanent in the system, and it can be consisted of many medications.

V. CONCLUSION

In most cases medical information systems are charged with a large number of users, hundreds or even thousands of them. It is almost impossible to satisfy the great population like that with user interface in any kind of area. However, health care as a very important feature of a modern society requires fast and reliable systems, considering the fact that one side of systems are live people, with limited response waiting time (babies, old ill people, etc). Sometimes that time is critical, as when it comes to emergency situations. MIS instead of paperwork is a huge change, especially for medical staff with 20 or more years of working experience. It can seriously reduce their working performance, and produce long lines of patients in the waiting rooms, in the beginning phase of using it.

Without cooperation with future users we cannot even imagine a good MIS as a result, since the views are always different from the designers and user's points of view. Brokers in the development of the IS can play a key role in the whole process, if there are some. However, our project has shown so far that much can be done, and designers could easily become agents to themselves, if they strongly respect process of designing user interface as is shown in Figure 1. Interaction with future users should not be a waste of time to the designer in any case. On the contrary, the more time spent in the phase 3 of mentioned process will reduce with the less time spent looping, and users will be more satisfied, and give less resistance to introducing new software.

Three things have proved to be important for designers of medical information systems in our project in the system-user interaction: neutralize the fear of introducing innovation in the work process with having these innovations presented in the user-close way; keep the user in the process of the similar daily routine work that was before the introduction of new system; and enable quick and easy way of using system functions without suggesting the user what is his future step or choice in working with the system. Consistency in the

interface of the module and all forms is necessarily implied. In order to reduce errors it is necessary to reduce the entrance of free text to the minimum, and wherever there is a predefined catalog, user should be given the choice of appropriate values. The smaller count of values for choosing user get, the quicker choice he will make, and the resulting error rate in choosing process will be reduced. Appropriate search component can be a solution to that, like we have shown in previous chapter. The order of fields in the form should follow the established working process, and the design of the form should always have at least one thing that user will recognize at the first human-system contact.

Beside MIS, these recommendations could be applied in any kind of information system designing, with some kind of modifications.

REFERENCES

[1] Hitoshi Iyatomi, Tomotaka Kasamatsu, Jun Hashimoto, M. Emre Celebi, Gerald Schaefer and Koichi Ogawa, "Perioperative cardiac risk prediction", ITAB 2009, Larnaca, Cyprus

[2] [2] Nikolaos S. Katertsidis, Christos D. Katsis, Dimitrios I.Fotaidis, "INTERPID, a biosignal-based system for monitoring of patients with anxiety disorders", ITAB 2009, Larnaca, Cyprus

[3] [3] Petar Rajković, Dragan Janković, Vladimir Tošić, "A Software Solution for Ambulatory Health Facilities in the Republic of Serbia", HEALTHCOM 2009 - 11th International Conference on e-Health Networking, Application and Services, Sydney, Australia 2009

[4] [4] Detlef Zuehlke, Gerrit Meixner, Ulrike Klein, "Smart Medical Software Systems for Dummies", HEALTHINF 2010, Valencia, Spain, ISBN: 978-989-674-016-0

[5] [5] Rita Kukafka, et al, "Redesigning electronic health record systems to support public health", Journal of Biomedical Informatics Volume 40, Issue 4, August 2007, Pages 398-409

[6] [6] Web site of Laboratory for Medical Informatics, http://medisnet.elfak.ni.ac.rs/. Latest access: November 20th, 2010.

[7] [7] P. Farinha, R. Cruz-Correia, L. Antunes, Filipe Almeida, A. Ferreira: From Legislation to Practice - "A Case Study of Break the Glass in Healthcare", HEALTHINF 2010, Valencia, Spain, ISBN: 978-989-674-016-0

Feed – Forward Based Direct Torque and Flux Control of Induction Motor in Field Weakening Regime

Petar Matić, Slobodan N. Vukosavić, and Dejan Raca

Abstract—**An original feed-forward stator flux regulator for induction machines is presented in this paper. The regulator is well suited for torque and flux control of induction machines in flux weakening regime, when the only available control variable is stator flux angle. Proposed regulator is analytically described and tested via computer simulation.**

Index Terms—**Induction Motor, Torque Control, Field Weakening.**

I. INTRODUCTION

INDUCTION motor can operate over a wide speed range, starting from zero speed, to the speed several times higher than the nominal. Operating mode with speeds larger than nominal is called the "field weakening", because in this regime the flux amplitude is less than nominal. Flux weakening is a natural consequence of voltage limit. There are a number of methods for controlling asynchronous motor in both voltage and current limit, but a satisfactory solution suitable for field weakening has not yet been found [1-10].

A common approach to operate in the field weakening is to simply choose the flux reference inversely proportional to the speed. Such a method does not include the current limit, leading that maximum performance of the drive can't be achieved. Vector control is based on the assumption of an independent control of flux and torque by using active and magnetizing current components. For the realization of decoupled control, it is necessary to have two degrees of freedom, which is not the case in field weakening due to voltage limit. Therefore, there is a need to deeply explore possible methods to directly control the induction motor in field weakening, and take into consideration the simultaneous current and voltage limits. The method must ensure optimal use of magnetic core of the motor with high-quality dynamic response.

The maximum (transient) torque of machine depends on rotor flux squared, and slip. Flux depends on the voltage

P. Matić is with the Faculty of Electrical Engineering, Banja Luka, Republic of Srpska, Bosnia and Herzegovina (e-mail: pero@etfbl.net).

S. N. Vukosavić is with the Faculty of Electrical Engineering, Belgrade, Serbia (e-mail: boban@ieee.org).

D. Raca is with AMSC Windtec, Klagenfurt, Austria (e-mail: draca@ieee.org).

limit, slip depends on the current limit, so transient torque depends on both limits. When the machine is fed from an ideal voltage source, then the maximum torque is equal to the break down torque. In this regime, the slip is equal to the break down slip which depends only on the motor parameters (it is constant at all speeds). The effect of voltage limit on transient characteristic is that break down torque in the field weakening decreases with the square of speed, while in the constant flux zone is constant.

The maximum torque that can be obtained in the presence of current limit is less than break down torque, and the corresponding slip is then less than break down slip. The influence of the current limit on transient characteristic can be analyzed by comparing the slip in the presence of maximum permissible current with the break down slip.

Rotor flux vector control is usually analyzed by assumption of quasi steady states of rotor flux. Current and voltage limits are presented in the d-q frame by circle and ellipse. The torque reference in that frame is represented as parabola, and the working point is found as intersection of the parabola either with circle or ellipse. Therefore, three characteristic regimes can be defined: first, when only the current limit should be observed (constant flux region), the second regime, when both current and voltage limit are observed (this mode corresponds to constant power mode), and finally, the third regime, when only the voltage limit is present. [8-15].

Stator flux vector control is usually simpler in field weakening because it is inherently based on voltage control of the machine. Analysis of operating points is performed in a plane defined by stator flux and torque. In field weakening it is necessary to simultaneously observe voltage and current limits, as well as stability limit. The working point must always be chosen by respecting the stricter requirement. The basic drawback of stator flux vector control is that this approach does not include the dynamics of the rotor circuit. In flux weakening, rotor flux decreases when load is increasing [15-20].

Direct torque control (DTC) performances are superior to vector control. Direct torque control is based on direct control of stator flux and torque, without current regulation, with maintaining the rotor flux at a given value. DTC takes the advantages of rotor flux vector control because it controls

rotor flux, and the advantages of the stator flux vector control because it uses a direct link between the stator flux and voltage. Drawback of common DTC solutions is that the current and voltage limits are taken into account indirectly, using the motor equations in steady state. In transient regimes stator flux regulator can go into saturation, or it can generate reference voltages larger than nominal voltage [15-20].

Influence of stator resistance is neglected at high speeds, because the voltage drop on it is only a few percent of the motor voltage. The influence of magnetic saturation is such that the voltage limit becomes more stringent when machine is saturated, than in the case of linear magnetic core. Analysis of the influence of magnetic saturation is performed by an approximation of magnetizing curve. When the machine is saturated, the output power at the entering of the field weakening zone may be even greater than the nominal power because the current can be significantly reduced. Saturated machines have a higher power at the same flux and same current limit. In the field weakening mode, a linear magnetic core is usually considered.

In this paper a DTC approach, based on full voltage utilization with taking current limit into consideration is presented. First, mathematical model is developed. On the basis of the model, a feed-forward torque control scheme based on voltage angle control is presented. The presented method is verified through computer simulation.

II. MATHEMATICAL MODEL

State-space model of induction motor in stationary reference frame, with fluxes as state variables in discrete time $k\Delta T$, $k = 0,1,2...$ is given by following equations:

$$\underline{u}_{sk} = R_s \underline{i}_{sk} + \frac{\Delta \underline{\Psi}_{sk}}{\Delta T},$$ (1)

$$\underline{u}_{rk} = R_r \underline{i}_{rk} + \frac{\Delta \underline{\Psi}_{rk}}{\Delta T} + j\omega_{mk} \underline{\Psi}_{rk},$$ (2)

$$\underline{\Psi}_{sk} = L_s \underline{i}_{sk} + M \underline{i}_{rk},$$ (3)

$$\underline{\Psi}_{rk} = L_r \underline{i}_{rk} + M \underline{i}_{sk}$$ (4)

$$m_k = \frac{3}{2} P \left(\underline{\Psi}_{sk} \times \underline{i}_{sk}\right) = -\frac{3}{2} P \, \text{Im}\left\{\underline{\Psi}_{sk} \underline{i}_{sk}^*\right\},$$ (5)

Where $\underline{u}, \underline{i}, \underline{\Psi}$ are voltage, current and flux vectors, R, L are resistance and inductance, M is mutual inductance, ω_m is speed (normalized to one pole pairs), m is torque, P is number of pole pairs. Stator and rotor variables are defined by indexes s, r, and j is imaginary unit.

Stator and rotor flux changes during the one sample period k, $k = 0,1,2...$ are defined by:

$$\Delta \underline{\Psi}_{sk} = \underline{\Psi}_{s(k+1)} - \underline{\Psi}_{sk},$$ (6)

$$\Delta \underline{\Psi}_{rk} = \underline{\Psi}_{r(k+1)} - \underline{\Psi}_{rk}.$$ (7)

Control variable at instant k, $k = 0,1,2...$ is voltage vector $\underline{u}_{sk}$. By combining (1) with neglected stator resistance with (6), the stator flux can be expressed as:

$$\underline{\Psi}_{s(k+1)} = \underline{\Psi}_{sk} + \Delta \underline{\Psi}_{sk} = \underline{\Psi}_{sk} + \underline{u}_{sk}\Delta T .$$ (8)

In stationary $\alpha - \beta$ reference frame, stator flux vectors $\underline{\Psi}_{sk}$ and $\underline{\Psi}_{s(k+1)}$ in two adjacent sample periods are shown in Fig. 1. When $\left|\underline{\Psi}_{s(k+1)}\right| \neq \left|\underline{\Psi}_{sk}\right|$, tip of stator flux vector $\underline{\Psi}_{s(k+1)}$ is on the circle K_2, which diameter can be larger or lesser than diameter of circle K_1. When $\left|\underline{\Psi}_{sk}\right| = \left|\underline{\Psi}_{s(k+1)}\right|$, tip of stator flux vector $\underline{\Psi}_{s(k+1)}$ is on the circle K_1. The angle $\Delta \vartheta_k$ between fluxes in two sample periods is also shown in Fig. 1 and in steady state it is equal to the product of synchronous speed and sample time:

$$\Delta \vartheta_k^0 = \omega_{sk}\Delta T .$$ (9)
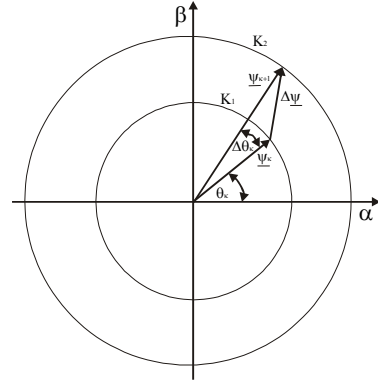
Fig. 1. Definition of Stator Flux Vector Increment $\Delta \underline{\Psi}$.

Stator flux vector increment can be rewritten in form of module and angle as:

$$\Delta \underline{\Psi}_{sk} = \left|\underline{\Psi}_{s(k+1)}\right|\left(\cos \Delta \vartheta_k + j \sin \Delta \vartheta_k\right) - \underline{\Psi}_{sk} ,$$ (10)

And from (1) stator flux vector increment is:
$$\Delta \underline{\Psi}_{sk} = \underline{u}_{sk}\Delta T .$$ (11)

By combining (10) and (11), stator flux vector increment is:
$$\Delta \underline{\Psi}_{sk} = \left|\underline{u}_{sk}\right|\Delta T\left[\cos\left(\pi - \Delta \chi_k\right) + j \sin\left(\pi - \Delta \chi_k\right)\right],$$ (12)

or
$$\underline{u}_{sk}^{\Psi_s} = \left|\underline{u}_{sk}\right|\left[\cos\left(\pi - \Delta \chi_k\right) + j \sin\left(\pi - \Delta \chi_k\right)\right],$$ (13)

where $\Delta \chi_k$ is the angle between stator flux increment vector, $\Delta \underline{\Psi}_{sk}$, and stator flux vector $\underline{\Psi}_{sk}$. The angles $\Delta \vartheta_k$ and $\Delta \chi_k$, as well as voltage vector $\underline{u}_{sk}^{\Psi_s}$ are referred to stator flux vector $\underline{\Psi}_{sk}$. These angles are shown in Fig. 2
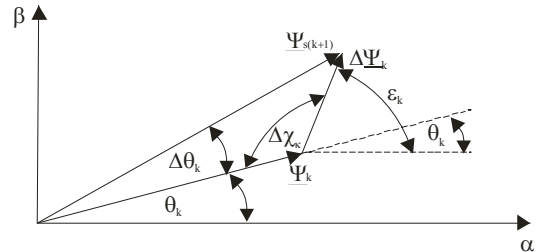
Fig. 2. Angle Definitions.

In (13), stator voltage vector, $\underline{u}_{sk}^{\Psi_s}$, which is control variable, is given by its modulus, $\left|\underline{u}_{sk}\right|$, and phase angle $\Delta \chi_k$

referred to the stator flux vector $\underline{\Psi}_{sk}$. Stator voltage transformed to the stationary reference frame is:

$$\underline{u}_{sk} = |\underline{u}_{sk}|\cos\varepsilon_k =$$
$$= |\underline{u}_{sk}|[\cos(\vartheta_k + \pi - \Delta\chi_k) + j\sin(\vartheta_k + \pi - \Delta\chi_k)]' \quad (14)$$

In constant flux region, stator voltage modulus is lower than rated voltage, i.e. $|\underline{u}_{sk}| < U_n$, while in the field weakening region, its modulus is constant and equal to the rated voltage $|\underline{u}_{sk}| = U_{MAX}$. In field weakening region, the only control variable is stator flux angle $\Delta\chi_k$.

Inputs to the mathematical model (1-5) are stator and rotor flux vectors, $\underline{\Psi}_{sk}$ and $\underline{\Psi}_{rk}$, and rotor speed ω_{mk}. Mechanical transients are slower than electrical ones, so in the model rotor speed can be assumed to be constant.

III. STATOR FLUX REGULATOR

Stator flux regulator can be realized as feed-forward regulator based on stator voltage equation (1) with stator resistance neglected [17]:

$$\Delta\underline{\Psi}_{sk} = \underline{u}_{sk}\Delta T = \underline{\Psi}_{k+1} - \underline{\Psi}_k. \quad (15)$$

Equation (15) is shown in Fig 3 and in Fig. 4 in stationary reference frame for cases of flux increasing and flux decreasing, respectively. Stator flux regulator should produce stator flux vector angle increment $\Delta\underline{\Psi}_{sk}$ which will guide both torque and flux to their references.
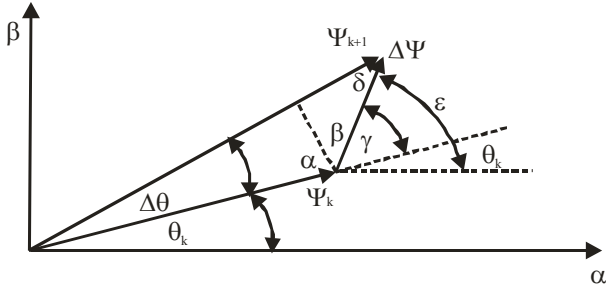
Fig. 3. Stator Flux Vector Increment When Flux is Increasing.
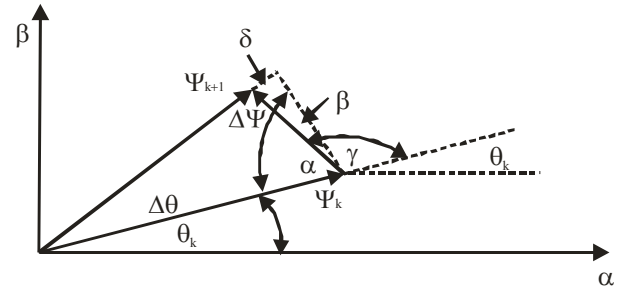
Fig. 4. Stator Flux Vector Increment When Flux is Decreasing.

Auxiliary angles α, β and δ shown in Figs 3 and 4 are the same as defined in Fig. 2. Components of stator flux vector increment are found as:

$$\Delta\Psi_\alpha = |\underline{\Psi}_{k+1}|\cos(\vartheta_k + \Delta\vartheta) - |\underline{\Psi}_k|\cos\vartheta_k = |\Delta\underline{\Psi}_{sk}|\cos\varepsilon, \quad (16)$$
$$\Delta\Psi_\beta = |\underline{\Psi}_{k+1}|\sin(\vartheta_k + \Delta\vartheta) - |\underline{\Psi}_k|\sin\vartheta_k = |\Delta\underline{\Psi}_{sk}|\sin\varepsilon. \quad (17)$$

Table 1 shows all combinations for angles from Fig 3 and Fig 4 for cases when flux is increasing, $|\underline{\Psi}_{k+1}| > |\underline{\Psi}_k|$, when flux is kept constant, $|\underline{\Psi}_{k+1}| = |\underline{\Psi}_k|$ and when flux is decreasing $|\underline{\Psi}_{k+1}| < |\underline{\Psi}_k|$. Angles for increasing and decreasing stator flux are different, and it is necessary to chose appropriate angle γ^+ or γ^- depending on the sign of the flux changes. When stator flux is kept constant, these angles are the same.

In case of very small sampling period, i.e., $\Delta T \to 0$, discrete model becomes continuous, and the angles α and γ are equal to $\pi/2$, meaning that flux vector increment has only the tangential component.

Stator flux regulator is shown in Fig. 5. Inputs to the regulator are stator flux angle advance $\Delta\vartheta$, the estimated flux $|\underline{\Psi}_{sk}|$ determined by its modules and the appropriate angle, and the sign of the difference between estimated and the reference torque. Outputs are the stator voltage components. The presence of sign of torque variations is necessary to determine the direction of flux change, increase or decrease. This sign is the same as the sign of torque change..

TABLE 1
CALCULATION OF ANGLES FROM FIG. 3 AND FIG. 4

	$\|\underline{\Psi}_{k+1}\| > \|\underline{\Psi}_k\|$	$\|\underline{\Psi}_{k+1}\| = \|\underline{\Psi}_k\|$	$\|\underline{\Psi}_{k+1}\| < \|\underline{\Psi}_k\|$
α	$\dfrac{\pi}{2} - \Delta\vartheta$	$\dfrac{\pi}{2} - \omega_k\Delta T$	$\dfrac{\pi}{2} - \Delta\vartheta$
β	$\dfrac{\pi}{2} - \arcsin\dfrac{\|\underline{\Psi}_k\|\sin\Delta\vartheta}{\|\Delta\underline{\Psi}_k\|}$	$\dfrac{\omega_k\Delta T}{2}$	$\dfrac{\pi}{2} - \arcsin\dfrac{\|\underline{\Psi}_k\|\sin\Delta\vartheta}{\|\Delta\underline{\Psi}_k\|}$
γ	$\Delta\vartheta + \arcsin\dfrac{\|\underline{\Psi}_k\|\sin\Delta\vartheta}{\|\Delta\underline{\Psi}_k\|}$	$\dfrac{\pi}{2} + \dfrac{\omega_k\Delta T}{2}$	$\pi + \Delta\vartheta - \arcsin\dfrac{\|\underline{\Psi}_k\|\sin\Delta\vartheta}{\|\Delta\underline{\Psi}_k\|}$
δ	$\arcsin\dfrac{\|\underline{\Psi}_k\|\sin\Delta\vartheta}{\|\Delta\underline{\Psi}_k\|}$	$\dfrac{\pi}{2} - \dfrac{\omega_k\Delta T}{2}$	$\arcsin\dfrac{\|\underline{\Psi}_k\|\sin\Delta\vartheta}{\|\Delta\underline{\Psi}_k\|}$
ε	$\vartheta_k + \Delta\vartheta + \arcsin\dfrac{\|\underline{\Psi}_k\|\sin\Delta\vartheta}{\|\Delta\underline{\Psi}_k\|}$	$\vartheta_k + \dfrac{\pi}{2} + \dfrac{\omega_k\Delta T}{2}$	$\vartheta_k + \Delta\vartheta + \pi - \arcsin\dfrac{\|\underline{\Psi}_k\|\sin\Delta\vartheta}{\|\Delta\underline{\Psi}_k\|}$

Fig. 5. Stator Flux Regulator.

IV. BLOCK DIAGRAM OF PROPOSED SOLUTION

Proposed solution for field weakening should satisfy the following requirements: a) Torque control should be based solely on the manipulation of the voltage phase angle when its amplitude is maintained at maximum. By this, full use of available inverter voltage is obtained. b) Torque increasing leads to rotor flux decreasing and vice versa, so there is a coupling between torque and flux which is the result of the voltage limit. c) The criterion for entering the field weakening is reaching the maximum available voltage. d) There must be a mechanism to prevent the collapse of the rotor flux because the algorithm is based on manipulation of the stator flux, to fulfill stability condition.

Fig. 6. shows the functional block diagram of the proposed direct torque control structure. The structure consists of a torque controller, stator flux controller, block for determining the entering to the field weakening region and the mechanism to prevent the collapse of the rotor flux. All necessary variables are estimated by the torque, and stator and rotor flux amplitude and angle estimator.

Torque controller is the PI feed-back controller, which is based on the deviation between torque reference and estimated torque. Another key element of the structure is a feed-forward

controller of the stator flux, which is based on the stator flux angle advance $\Delta \vartheta$.

Voltage amplitude is determined by the torque reference, synchronous speed and rotor flux (in the first zone), while in the second zone it is limited to maximum available voltage:

$$u_s = \begin{cases} \dfrac{|\omega_s|}{\Psi_r} \dfrac{L_s}{L_m} \sqrt{\Psi_r^4 + \sigma^2 L_r^2 \dfrac{4}{9P^2} m_e^2} & u_s \leq u_{sn} \\ u_{sn}, & u_s = u_{sn} \end{cases} \tag{18}$$

Finally, to prevent rotor flux collapse, which occurs when the slip is larger then break – down slip, there is a structure that stops increasing of the angle when slip becomes equal to the break – down slip.

In the constant flux zone, stator voltage will increase when the torque and speed increases. In the field weakening zone the voltage will be kept on the nominal value. As long as the voltage is less than the nominal, there are two control values (voltage angle and amplitude), whereas, when the voltage reaches the nominal value, the only control variable is the voltage angle.
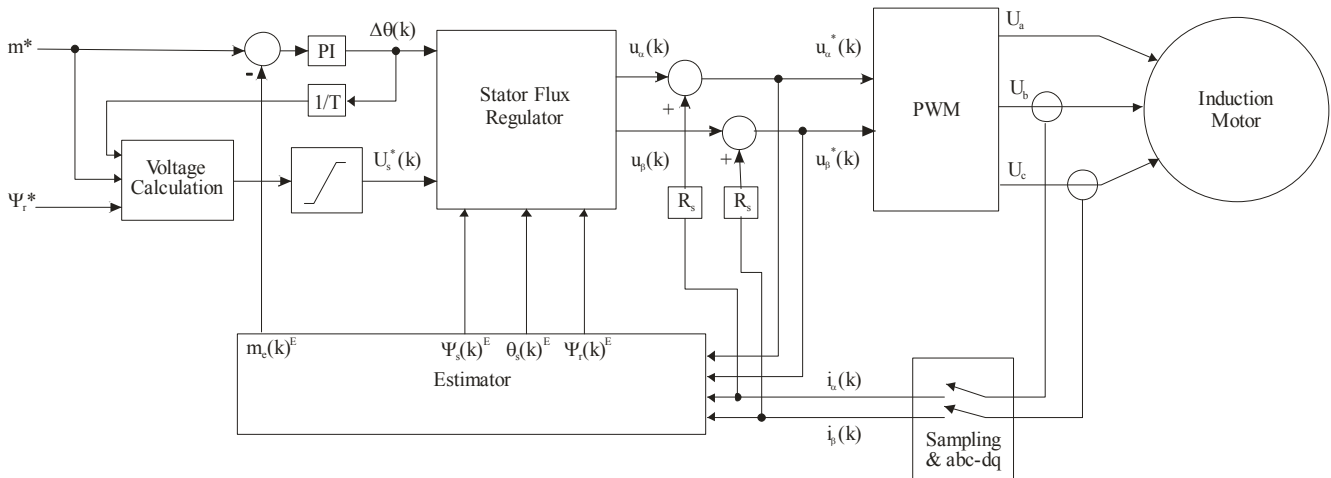
Fig. 6. Block-Diagram of the Proposed Solution.

V. SIMULATION RESULTS

Simulation of the proposed solution was performed in the program MATLAB – SIMULINK. Motor with rated parameters 7.5 kW, 50Hz, 380V is controlled in torque mode. Reference torque was equal to the 25% of the rated torque, so machine speeds up from standstill to the field weakening zone with constant torque. Simulation results of are shown in Fig. 7 with all variables in per-unit [p.u] values.

As it can be seen in Fig. 7, machine torque is constant through the whole simulation period. Stator and rotor fluxes are constant when the speed is below rated value, and are decreased in field weakening region.

Stator flux angle advance $\Delta\vartheta$ is continuously increasing, as synchronous speed increases. Slip speed is constant in the constant flux region, and is increasing in field weakening region because rotor flux decreases, even the torque is kept constant.

Finally, stator voltage increases in the constant flux zone when speed increases, and is kept on the rated value after the machine enters field weakening zone.

Fig. 7. Simulation results.

VI. CONCLUSION

The paper proposed a structure for the direct torque and flux control suitable for implementation in the field weakening regime. In field weakening regime there is only one control value, the voltage angle, because the machine voltage amplitude is limited to the nominal value. It is possible only to control torque, while the flux is independently established with respect to voltage limit.

Current limit can be satisfied by limiting the slip to the break – down slip.

Practical implementation of proposed solution is very complicated due to the parameter sensitivity. The further work on voltage angle control in field weakening should be based on the reconfiguration of the proposed solution to eliminate this parametric sensitivity.

REFERENCES

[1] Slobodan N. Vukosavić *Digitalno upravljanje električnim pogonima*, Akademska Misao, Beograd 2003.

[2] Peter Vas: *Sensorless Vector and Direct Torque Control*, Oxford University Press, London, 1998.

[3] Peter Vas Electrical Machines and Drives: *A Space-Vector Theory Approach*, Oxford University Press, London, 1992.

[4] G. Buja, M. Kazmierkowski: "Direct Torque Control of PWM Inverter – Fed AC Motos – A Survey", *IEEE Transactions on Industrial Electronics*, Vol. 51, No.4, pp. 744-757, August 2004.

[5] Đ. Stojić: „Direktno upravljanje asinhronim motorom", *doktorska disertacija*, Univerzitet u Beogradu, 2004.

[6] Dj. M. Stojic, S. N. Vukosavic: "A New Induction Motor Drive Based on the Flux Vector Acceleration Method", *IEEE Transactions on Energy Conversion*, Vol. 20, No. 1, pp.173-180, March 2005.

[7] P. Matić, D. Raca, B. Blanuša, S. N. Vukosavić: "Direct Torque Controlled Induction Motor Drive Based on Double Feedback Structure", *Electronics*, Vol. 1, No. 1, pp. 41-48, September/October 2006.

[8]   N. T. West, R. D. Lorenz: "Implementation and Evaluation of a Stator and Rotor Flux Linkage-Based Dead-Beat, Direct Torque Control of Induction Machines at the Operational Voltage Limits",*The Fourty-Second IAS Annual Meeting 2007, Conference Record*, pp.690-695, 23-27. September 2007.

[9]   M. Mengoni, L. Yarri, A. Tani, G. Serra, D. Casadei: "Stator Flux Vector Control of Induction Motor Drive in the Field Weakening Region", *IEEE Transactions on Power Electronics*, Vol. 23, No. 2, pp. 941-949, March 2008.

[10] Jidin, N. Idris, A. Yatim, M. Elbuluk, " A Novel Overmodulation and Field Weakening Strategy for Direct Torque Control of Induction Machines", *The Fourty-Third IAS Annual Meeting 2007, Conference Record*, pp.1-8, 5-9. October 2008.

[11] N. Oikonomou, J. Holtz: "Stator Flux Trajectory Tracking Control for High-Performance Drives", The Fourty-First IAS Annual Meeting 2006, *Conference Record*, Vol. 3, pp.1268-1275, 8-12. October 2006.

[12] M. Mengoni, L. Yarri, A. Tani, G. Serra, D. Casadei: "Stator Flux Vector Control of Induction Motor Drive in the Field Weakening Region", *IEEE Transactions on Power Electronics*, Vol. 23, No. 2, pp. 941-949, March 2008.

[13] A. Jidin, N. Idris, A. Yatim, M. Elbuluk: "A Novel Overmodulation and Field Weakening Strategy for Direct Torque Control of Induction Machines", The Fourty-Third IAS Annual Meeting, Conference Record, pp.1-8, 5-9. October 2008.

[14] N. T. West, R. D. Lorenz: "Digital Implementation of Stator and Rotor Flux-Linkage Observers and a Stator-Current Observer for Deadbeat Direct Torque Control of Induction Machines", *IEEE Transactions on Industry Applications*, Vol. 45, No. 2, pp. 729-736, March/April 2009.

[15] Y. S. Lai, J. H. Chen: "A New Approach to Direct Torque Control of Induction Motor Drives for Constant Inverter Switching Frequency and Torque Ripple Reduction", *IEEE Transactions on Energy Conversion*, Vol. 16, No. 3, September 2001.

[16] D. Casadei, G. Serra, A. Tani, L. Zarri, F. Profumo: "Performance Analysis of a Speed Sensorless Induction motor Drive Based on a Constant Switching Frequency DTC Scheme", *IEEE Transactions on Industry Applications*, Vol. 39, No. 2, March/April 2003.

[17] P. Matić, B. Blanuša, S. N. Vukosavić, "A Novel Direct Torque and Flux Control Algorithm for the Induction Motor Drive", IEEE International Electric Machines and Drives Conference, IEMDC'03, *Proceedings*, Vol. 2, pp. 965-970, 1-4. June 2003.

[18] Barbara H. Kenny, Robert D. Lorenz: "Stator and Rotor Flux Based Deadbeat Direct Torque Control of Induction Machines", *IEEE Transactions on Industry Applications*, Vol 39, No. 4, July/August 2003.

[19] C. Lascu, A. Trzynadlowski: "Combining the Principles of Sliding Mode, Direct Torque Control, and Space-Vector Modulation in a High-Performance Sensorless AC Drive", *IEEE Transactions on Industry Applications*, Vol. 40, No. 1, pp. 170-177, January/February 2004.

[20] N. T. West, R. D. Lorenz: "Implementation and Evaluation of a Stator and Rotor Flux Linkage-Based Dead-Beat, Direct Torque Control of Induction Machines at the Operational Voltage Limits",The Fourty-Second IAS Annual Meeting 2007, *Conference Record*, pp.690-695, 23-27. September 2007.

Mutual Inductance Variation Influence on Induction Motor IFOC Drive

Milan Mijalković and Petar Petrović

Abstract—**This paper describes a solution to the mutual inductance variation problem in the Indirect Field Oriented (IFOC) controlled induction motor. Initially, the influence of the variation on the produced flux, torque and torque per ampere is analyzed and experimentally verified. After that, a simple model modification is proposed and discussed. Finally, the solution is implemented on an AC motor-drive and verified experimentally by comparing the torque step response before the modification, and after it.**

Index Terms—**Induction motor, IFOC, Parameter variation, Nonlinearities, Saturation, Mutual inductance variation.**

I. Introduction

IN the contemporary high performance AC motor drives, the most widely used scheme is an indirect field oriented control (IFOC) with current controllers in *d-q* reference frame tied to the rotor flux vector. In this type of drives, a mismatch between machine parameters used in the controller and the actual machine parameters, which occurs due to changes in temperature or saturation, results in the following [1]:

- The flux level is not properly maintained, and the rotor flux amplitude is not equal to the expected value.
- The resulting steady state torque is not equal to the commanded values.
- The torque response is not instantaneous.
- The correlation between i_{qs} and torque, as well as the correlation between i_{ds} and flux is not linear anymore.

These effects are widely documented in literature [2,3]. In the indirect field oriented control schemes with current controllers in *d-q* reference frame tied to the rotor flux vector, the parameter of greatest interest is the rotor time constant τ_r, $\tau_r = L_r/R_r = (M+L_{\sigma r})/R_r$, where L_r, R_r and $L_{\sigma r}$ are rotor inductance, rotor resistance and rotor leakage inductance, respectively. *M* denotes mutual inductance between stator and rotor.

A wrongly set parameter in the model yields the differrence between the commanded and obtained values of the currents even if the current controllers are ideal. Both, the torque-producing (i_{qs}) and the flux-producing (i_{ds}) currents are affected.

This paper primarily deals with the influence of the mutual inductance mismatch (difference between the value of parameter *M* used in the controller and the real value of *M* in the machine) due to saturation and experimentally verifies a simple mathematical-model modification that reduces the above mentioned influence on the drive performance.

II. Mathematical Model

A model of an induction machine dynamics (assuming linear magnetic), in the *d-q* frame oriented so that the *d*-axis is aligned with the total rotor flux vector [1], is shown in Fig. 1.
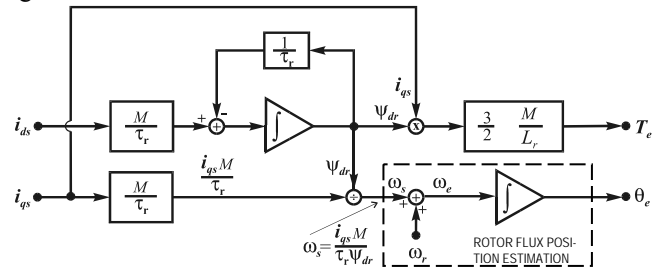
Fig. 1. Induction machine dynamics model in the *d-q* frame.

In Fig. 1, i_{ds} denotes the stator current *d*-component (flux producing current). This current component affects the rotor flux ψ_{dr} only. i_{qs} is the stator current *q*-component which controls the electrical torque T_e exclusively (has no influence on the rotor flux ψ_{dr}). ω_s is the angular slipping frequency, and ω_e and ω_r are the excitation (stator), and the rotor angular frequency, respectively. θ_e is current rotor flux angle, and p_p is the number of motor pole pairs.

This model assumes a correct orientation of the *d-q* reference frame. To get the correct orientation, the controller that controls *the* drive must have the correct information about the current rotor flux angle θ_e because this angle is used in the transformation of the measured currents. The result of the transformation is the value of the stator current components i_{ds} and i_{qs}, used as the input in the model. For this reason (to get current θ_e) the controller contains a software copy of the model. The software model runs in parallel with the machine following the dynamics of all variables.

M. Mijalković is with Professional studies school of electrical and computer engineering Belgrade, Serbia, (e-mail: milan.mijalkovic@viser.edu.rs).

P. Petrović is now with "Power network of Serbia".

The difference between the real model in the machine and the software model is that the latter has the reference currents i_{ds}^* and i_{qs}^* as the model input (instead of i_{ds} and i_{qs}).

The torque producing current reference i_{qs}^* (q-component) controls the torque while the d-component reference (or flux-producing current) i_{ds}^* controls the amplitude of the rotor flux. By means of i_{qs}^* the controller calculates the angular slip frequency as:

$$\omega_s^* = \frac{i_{qs}^* M^*}{\tau_r^* \psi_{dr}^*},$$

where τ_r^* presents the rotor time constant value used as a parameter in the controller. The rotor time constant is defined as $\tau_r = (M + L_{\sigma r})/R_r$. Stars in superscript for motor parameters identify the values used in mathematical model (in the controller) and are not necessarily equal to actual parameters in the machine.

The integral of ω_s^* presents the "slip contribution" to the rotor flux position, and is used to estimate (by adding to measured rotor position) current rotor flux position (θ_e^*), essential for coordinate transformations. Since the controller calculates ω_s^* using wrong parameter values, the estimated angle θ_e^* is not equal to the real rotor flux position (angle θ_e) in the machine. Unfortunately, the controller uses this, wrongly estimated, angle θ_e^* to rotate (transform from the stationary to rotated frame) the measured stator currents $i_{\alpha s}$ and $i_{\beta s}$. The transformation (rotation) is necessary to get the d and q component of the stator current because the current controllers work in the synchronous rotating d-q frame.

Critical parameters for the correct θ_e estimation are the rotor resistance R_r and the mutual inductance M. The leakage inductance $L_{\sigma r}$ which is also included in τ_r expression, is usually much smaller than M, appears always in sum with much larger M, and does not vary too much.

Rotor resistance varies a lot with the machine heating, and the mutual inductance M depends on current i_{ds} (or, more precisely, on magnetizing current, i_m, which is equal to i_{ds} in steady state). This paper discusses only the influence of mutual inductance variations. The rotor resistance R_r is considered as a known constant in the simulations, and the experiments are carried out in such a way that it could be treated constant as well.

III. SATURATION EFFECTS

Fig. 2. shows the magnetizing curve of the experimental motor and the shape of variation of the mutual inductance with the d-component of the stator current I_{ds} (which is equal to the magnetizing current i_m in steady state [5,6,8]). I_{ds} is a symbol for i_{ds} in steady state.

The diagram shows that the parameter M, for I_{ds} larger than nominal ($I_{dsn} = 3{,}59$ A), changes the value considerably. The value in the linear part is almost 2.5 times larger than the value of M at $I_{ds} = 12$ A.
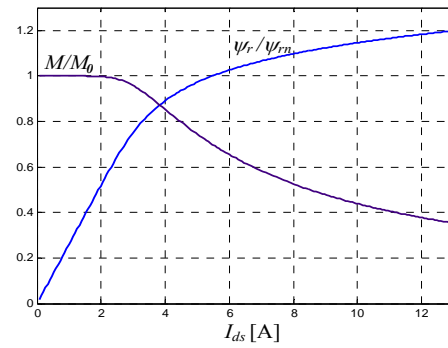
Fig. 2. Experimentally obtained magnetizing curve ψ_r / ψ_{rn} and relative mutual inductance M/M_0 for the experimental machine. M_0 is the mutual inductance in the linear part (163,7mH) and ψ_{rn} is the nominal motor flux (0,59Wb).

Even if the reference value I_{ds}^* never exceeds the nominal, the actual I_{ds} can be several times larger than expected if the parameter R_r^* used in the controller differs from R_r in the machine [7]. For these reasons, the variation of M cannot be neglected.

The importance of taking this variation into account can be seen from the maximum available torque with limited stator current amplitude ("Torque per Ampere" characteristic [8,9]).

Fig. 3. shows the maximum available electrical torque T_e as a function of the slipping frequency f_s with the limited current capacity of the inverter (which is certainly the case). The diagram is obtained by simulation of the experimental machine, described in chapter 5.

The maximum allowed inverter current (which is proportional to $|I_s|$) was first limited to 10A. The reference I_{ds}^* was varied from 0.25 I_{dsn} (0.9A) to $|I_s|$ in 0.05A increments. The entire remaining portion of the inverter current capacity (from 10A) was used for I_{qs}^*. For instance, in the point where $I_{ds}^* = 6$A for I_{qs}^* was left 8A ($\sqrt{10^2 - 6^2}$). For all obtained $I_{ds}^* - I_{qs}^*$ pairs, the values of slipping frequencies f_s ($f_s = \omega_s/2\pi$) and electrical torque T_e was calculated using the model given in Fig. 1. The produced electrical torque T_e was shown as a function of f_s. The simulations were repeated for $|I_s| = 8$A, then for 5A and finally, for 3A.
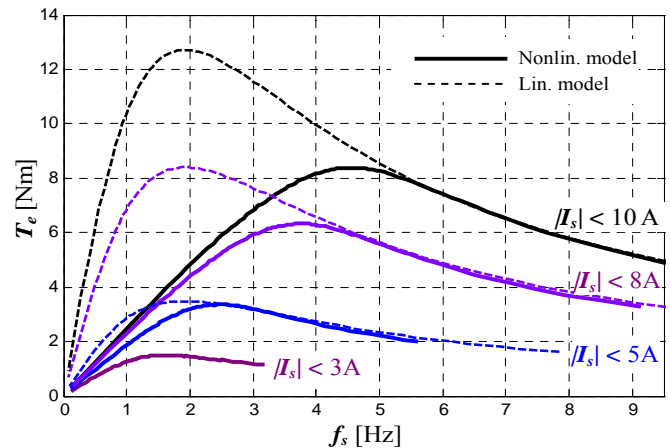
Fig. 3. Produced electrical torque as a function of slip speed for limited stator current magnitude $|I_s|$ using linear and nonlinear machine model. Simulation result for the experimental machine.

In Fig. 3., solid line presents the simulation result with the model that takes into account the variation of M as a function of I_{ds} (as shown in Fig. 2), and dashed line presents the result with the linear model ($M = M_0 = const$).

It is obvious that the maximum achievable torque is considerably different. Moreover, using the linear model, maximum moment is always achieved for $\omega_{s0} = 1/\tau_r$ [7] independently of the limited $|I_s|$ value. In the nonlinear model, the angular slip frequency that produces the maximum torque is different from ω_{s0}, and the difference is larger for larger stator currents.

IV. SATURATED MACHINE DYNAMICS

In the paper [8] the author analyzes the influence of the mistuned τ_r^* on the flux dynamics and on the electrical torque produced by the machine. The analysis described in this chapter is generally based on this paper, with more attention paid on the influence of changing mutual inductance M with i_{ds}, and with the presumption that the rotor resistance R_r is constant and equal to the parameter R_r^* set in the controller. The important influence of R_r variation is analyzed separately (not in this article).

If the value of parameter τ_r^* set in the controller is different from the actual rotor time constant τ_r for $\Delta\tau_r = \tau_r^* - \tau_r$, as a consequence of the mistuned mutual inductance which has been changed for $\Delta M = M^* - M$, the rotor flux in the machine will differ from the one expected in the model. Besides, the q-component of the rotor flux (ψ_{qr}), which should be zero in case of correct d-q frame orientation, will become non-zero. It is possible to define the following flux components errors:

$\Delta\psi_{dr} = \psi_{dr}^* - \psi_{dr}$, where ψ_{dr}^* is the value in the controller

$\Delta\psi_{qr} = -\psi_{qr}$ or, in the matrix form:

$$\begin{bmatrix} \Delta\psi_{dr} \\ \Delta\psi_{qr} \end{bmatrix} = \begin{bmatrix} \psi_{dr}^* \\ 0 \end{bmatrix} - \begin{bmatrix} \psi_{dr} \\ \psi_{qr} \end{bmatrix} \tag{1}$$

Since the d-component of the rotor flux is not zero, the model shown in Fig. 1. is not valid anymore. The equation system that now describes flux dynamics is:

$$\begin{bmatrix} \dot{\psi}_{dr} \\ \dot{\psi}_{qr} \end{bmatrix} = \begin{bmatrix} -\dfrac{1}{\tau_r} & \omega_s \\ -\omega_s & -\dfrac{1}{\tau_r} \end{bmatrix} \begin{bmatrix} \psi_{dr} \\ \psi_{qr} \end{bmatrix} + \dfrac{M}{\tau_r} \begin{bmatrix} i_{ds} \\ i_{qs} \end{bmatrix} \tag{2}$$

with dots over variables representing the first derivative of the variable.

The expression for the electrical torque is given by [1]:

$$T_e = \frac{3}{2} p_p \frac{M}{L_r} \left(\psi_{dr} i_{qs} - \psi_{qr} i_{ds} \right) \tag{3}$$

From the expressions (1) and (2), the flux error components are:

$$\begin{bmatrix} \dot{\psi}_{dr} \\ \dot{\psi}_{qr} \end{bmatrix} = \begin{bmatrix} -\dfrac{1}{\tau_r} & \omega_s \\ -\omega_s & -\dfrac{1}{\tau_r} \end{bmatrix} \begin{bmatrix} \psi_{dr} \\ \psi_{qr} \end{bmatrix} + \dfrac{M}{\tau_r} \begin{bmatrix} 0 \\ M i_{qs} \dfrac{1}{\tau_r} \dfrac{\Delta M}{M} \end{bmatrix} \tag{4}$$

The solution of these differential equations in s-domain is:

$$\Delta\psi_{dr} = M\, i_{qs} \frac{\Delta M}{M} \frac{\omega_s \tau_r}{s^2 \tau_r + 2s\tau_r + (1 + \omega_s^2 \tau_r^2)}$$

$$\Delta\psi_{qr} = M\, i_{qs} \frac{\Delta M}{M} \frac{1 + s\tau_r}{s^2 \tau_r + 2s\tau_r + (1 + \omega_s^2 \tau_r^2)} \tag{5}$$

The error between the actual electrical torque and the electrical torque produced in the hypothetical model with the well oriented d-q frame is given by:

$$\Delta T_e = \frac{3}{2} p_p \frac{M}{L_r} \left(\Delta\psi_{dr}\, i_{qs} - \Delta\psi_{qr}\, i_{ds} \right) \tag{6}$$

with the flux components errors given in (5).

The expression (6) shows the influence of the mutual inductance error ΔM on the electrical torque produced by the machine. Several conclusions can be drawn from (6):

- The torque response to the i_{qs} change has an oscillatory character. The system is under-dumped (and stable), because the eigenvalues of the system given by:

$$s_{1,2} = -\frac{1}{\tau_r} \pm j \frac{1}{\tau_r} \frac{i_{qs}}{i_{ds}} = -\frac{1}{\tau_r} \pm j \frac{1}{\tau_r} a \tag{7}$$

- The damping factor is:

$$\xi = \frac{1}{\sqrt{1 + \omega_s^2 \tau_r^2}} = \frac{1}{\sqrt{1 + \left(\dfrac{i_{qs}}{i_{ds}}\right)^2}} = \frac{1}{\sqrt{1 + a^2}} \tag{8}$$

with $\omega_s \tau_r = i_{qs}/i_{ds} = a$.

- The oscillations are more damped if the ratio i_{qs}/i_{ds} is smaller (eqn. 8). This means that the sensitivity of the field controlled drive generally increases with the load. With no load ($i_q = 0$), errors in fluxes are zero, as well as in the torque. Higher power motors (having relatively lower magnetizing current) are more susceptible.

- Besides the undesirable oscillations, the steady state error exists as well. Both the flux components and the produced torque have the steady state error. Using the "load factor" a, defined in equation (8), the errors in the fluxes are:

$$\Delta\psi_{dr}^S = \frac{\Delta M}{M} \frac{a^2}{1 + a^2} \psi_{dr}$$

$$\Delta\psi_{qr}^S = \frac{\Delta M}{M} \frac{a}{1 + a^2} \psi_{dr} \tag{9}$$

In equation (9), superscript ^{S} denotes steady state value, and ψ_{dr} is the d-component flux value that would exist if the mutual inductance M were constant and equal to the value set in the controller. In this case this flux component would be equal to the rotor flux amplitude.

The steady state rotor flux amplitude is:

$$\left|\psi_r^S\right| = \frac{\sqrt{1 + a^2}}{\sqrt{1 + \left(1 + \dfrac{\Delta M}{M}\right)^2 a^2}} \left|\psi_{r0}\right| \tag{10}$$

with ψ_{ro} being the amplitude of the rotor flux that would be built in a well tuned controller. The electrical torque is:

$$T_e^S = \left(1 + \frac{\Delta M}{M}\right) \frac{\left(1 + a^2\right)}{1 + \left(1 + \frac{\Delta M}{M}\right)^2 a^2} T_{e0} \qquad (11)$$

where T_{e0} is the electrical torque that would be achieved if the mutual inductance M were equal to the value set in the controller.

A simulation result of the torque response to the torque reference step from zero to the nominal value, with the flux producing current reference (I_{ds}^*) 1.2 and 1.5 times higher than nominal (requested rotor flux 20% and 50% above nominal) is shown in Fig. 4.
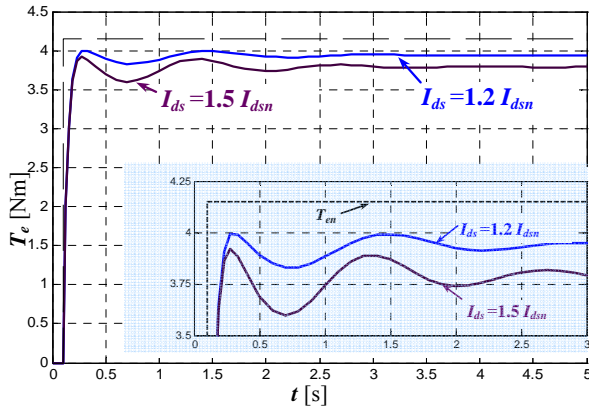
Fig. 4. Torque response to the reference step from zero to the nominal value with the requested rotor flux 20% and 50% above the nominal value.

The flux producing reference current (i_{ds}^*) has been kept constant at a value 20% and 50% higher than nominal. The reference torque step was made by a torque producing reference current (i_{qs}^*) step from zero to the value that provides the nominal torque at a given rotor flux. The command step takes place at $t = 0{,}1s$, when the flux has already been built. The simulation was made for experimental machine (chapter VI) using the expressions (3), (5) and (6).

The dashed line is a theoretical response for a well tuned controller. The embedded picture is an enlarged look at the step instant, shown to emphasize the delay and a shape of the response.

V.　Mathematical Model Modification Saturated

The previous chapters show that the influence of saturation must be taken into account. It is possible to decrease the influence by improving the mathematical model if the magnetizing curve is known. There are numerous papers with proposed method for magnetizing curve identification at first start [11] and for the two parameter curve approximation [9] or tabulating.

This chapter is based on the results presented in [6] and proposes a slight simplification used in the experimental drive.

The rotor flux d-component ψ_{dr} can be split into two parts. The major part is a magnetizing flux ψ_m which depends on the magnetizing current i_m. The other, much smaller part is a

leakage flux $(L_{\sigma r} i_{dr})$. The parameter $L_{\sigma r}$ can be treated as a constant (chapter II). With the assumption of the correct field orientation ($\psi_{qr} = 0$; $\psi_{dr} = \psi_r$), the d-component rotor voltage equilibrium (Fig. 5b) expression becomes:

$$0 = \frac{d\psi_{dr}}{dt} + R_r i_{dr} \Rightarrow \frac{d\psi_{dr}}{dt} = -R_r i_{dr} = R_r \left(i_{ds} - i_m\right) \qquad (12)$$
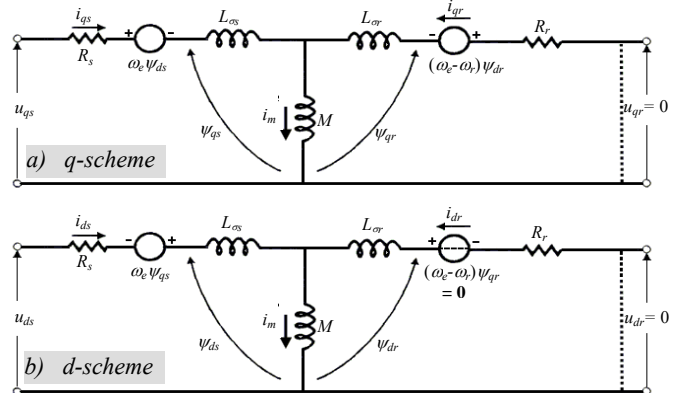
Fig. 5. Equivalent scheme of the machine in the d-q reference frame (a) q-component scheme, (b) d-component scheme. The schemes are independent of each other.

Magnetizing current i_m and magnetizing flux ψ_m are coupled by magnetizing curve (that mainly depends on motor construction and material) and i_m can be expressed as a function of ψ_m. This flux can be expressed as $\psi_m = \psi_{dr} - L_{\sigma r} i_{dr}$

$$i_m = f_1\left(\psi_m\right) = f_1\left(\psi_{dr} - L_{\sigma r} i_{dr}\right) \qquad (13)$$

or, from (12):

$$\frac{d\psi_{dr}}{dt} = R_r i_{ds} - R_r f_1\left(\psi_{dr} - L_{\sigma r} i_{dr}\right) \qquad (14)$$

From the expression (14), ψ_{dr} can be solved as a function of i_{ds}. Rotor current d-component i_{dr} is a function of i_{ds} and i_m.

Using (14) it is possible to modify the model given in Fig. 1. In the modified model (Fig. 6.), f_1 and f_2 are the tables in the controller.
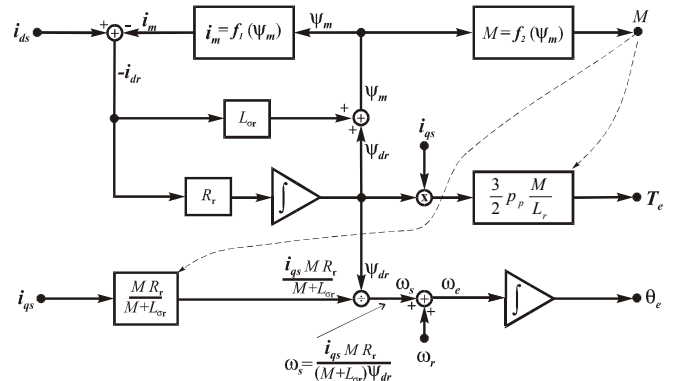
Fig. 6. Modified induction machine dynamics model in the d-q frame that respects the variation of M due to saturation.

Parameter M, used in some blocks, is now a dynamically adjusted variable read from table f_2. This table, denoted as $M = f_2(\psi_m)$ is derived from the known magnetizing curve $i_m = f_1(\psi_m)$ by calculating $M = \psi_m / i_m$ for certain ψ_m with i_m read from the first table. Input for both tables is ψ_m.

VI. EXPERIMENTAL VERIFICATION

To prove the conclusions, the experimental setup has been made using a standard induction machine coupled to a dynamic brake and fed from a three phase inverter controlled by a PC (Fig. 7.).
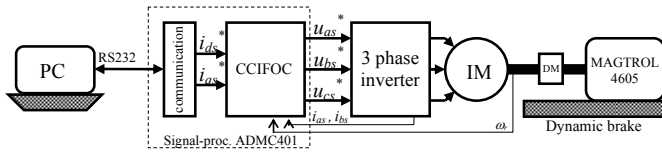

Fig. 7.   Experimental setup. PC provides the reference values for the torque that motor should produce and for the rotor flux level. The dynamometer DM measures the produced torque.

The experimental setup is based on a standard four-pole, 0.75kW induction motor. The motor is fed from a three phase inverter with an indirect vector controller and current controllers of i_{ds} i i_{qs} in a synchronous d-q frame tied to the rotor flux vector. CCIFOC is implemented on a signal-processor ADMC401 and it is connected to a PC using RS232. PC controls the torque using i_{qs}^*, while the rotor flux is controlled by means of i_{ds}^*. For the particular motor, all parameter values, including the magnetizing curve are measured according to standard IEEE112. The tables f_1 and f_2 (chapter V) are derived from the experimentally obtained magnetizing curve.

Nominal torque of the motor is 4.15 Nm and is produced at the nominal slip speed ω_{snom}= 8 rad/s (f_{snom}= 1.27 Hz). Other parameters are as follows: stator resistance R_s= 3.35Ω; rotor resistance R_r= 1.99Ω; stator and rotor inductances L_s=L_r=170.7mH and the linear part mutual inductance M_0= 163.7 mH. Rotor time constant is τ_r= 85.7ms.

The motor is mechanically coupled to the dynamic brake Magtrol 4605 [12] which is set to the maximum available torque (24 Nm). As the motor cannot produce 24 Nm, the brake practically blocks the shaft, making a standstill conditions (ω_r= 0) and in the experiment, only its dynamometer (Magtrol 4613 [12]) is used.

The experimental results for the torque reference step, identical to the step in the simulation (chapter 3), are shown in Fig. 8. and 9.
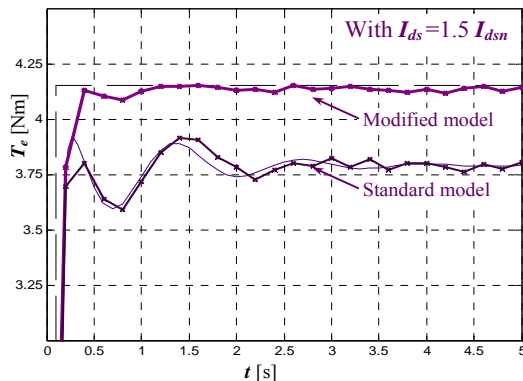

Fig. 8. The torque step response with the flux producing current 50% higher than nominal.
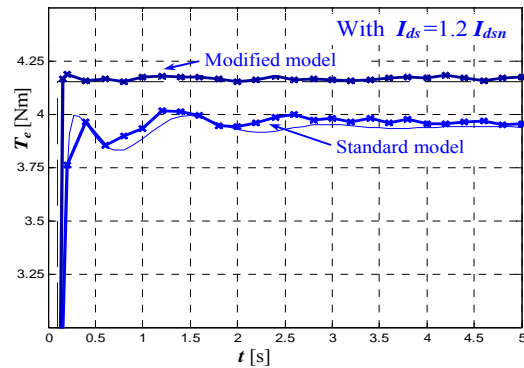

Fig. 9. The torque step response with the flux producing current 20% higher than nominal.

One curve is obtained using the standard model, while the other one is the result, using the modified model (shown in Fig. 6.). The thin line is repeated simulation result. The torque was sampled each 100ms. It should be stressed that the dynamometer input has an unavoidable second order low-pass filter with time constant of 10ms, so that measured values are slightly delayed from actual.

The modified scheme eliminates the influence of M variation only if the rotor resistance is tuned well, as it is in these experiments. Otherwise, the compensation is not full because the model uses i_{ds}^* and i_{qs}^* and not actual i_{ds} and i_{qs}.

VII. CONCLUSION

Induction motor drive with indirect vector control is sensitive to parameter variation. The critical parameter is rotor time constant, or mutual inductance and rotor resistance which dominantly define the rotor time constant. This paper concerns only the influence of the mutual inductance variation. The reason for this parameter variation is mainly (sometimes unavoidable) main flux path saturation.

Due to mutual inductance variation, produced electrical torque is different than expected, the response to command change is not instantaneous and have dumped oscillatory shape. It is possible to get partially solved the saturation problem by means of an improved model with a tabulated magnetizing curve.

The experiment showed close parallel with the simulation results.

REFERENCES

[1]   D. W. Novotny and R. D. Lorenz, ed., "Introduction to Field Orientation and High Performance AC drives," Tutorial Course. IEEE-IAS Conf. Recd, Denver, 1986.
[2]   R. Krishnan, "Electric Motor Drives", Prentice Hall, 2001.
[3]   D.W. Novotny and T.A. Lipo, "Vector Control and Dynamics of AC Drives", Oxford University Press, 1998.
[4]   Velez-Reyes, M.; Mijalkovic, M.; Stankovic, A.M. "Output selection for tuning of field oriented controllers: steady state analysis", Industry Applications Conference, 2003. 38th IAS Annual Meeting. Conference Record of the Vol. 3, Issue , 12-16 Oct. 2003 Page(s): 2012 - 2017, Vol.3
[5]   P. Vas, M. Alakula, E. Hallenius "Field-Oriented Control of Saturated AC Machines" Conf. Rec. of the IEE International Conf. on Power Elect. And Variable Speed Drives, London 1988, pp. 283-286.

[6] E. Levi, V. Vuckovic, "Field-oriented Control of Induction Machines in the Presence of Magnetic Saturation", Electric Machines and Power Systems, No 16, 1989, pp 133-147.

[7] M. Mijalković, A. Stanković, S. Obradović, "Detuned operation of indirect field oriented control of induction motor" UNITECH07 Conf. Rec. Gabrovo, Bulgaria 2007.

[8] L. Garces, "Parameter Adaption for the Speed-Controlled Static AC Drive with a Squirrel-Cage Induction Motor", IEEE Trans. on Industry Application, vol.16, No 2, 1980, pp. 173-178.

[9] F. Khater, R. Lorenz, D. Novotny, "The Selection of Flux Level in Field-Oriented Induction Controllers with Consideration of Magnetic

Saturation Effects", IEEE Trans. on Industry Application, vol. 23, No 2, 1987 pp. 276-282.

[10] E. Levi, S. Vukosavic, V. Vuckovic, "Study of main flux saturation in field oriented induction motor drives", Conf. Rec. IEEE Ind. Electron. Soc. Ann. Meet. IECON'89, pp 219-231.

[11] E. Levi, M. Sokola, S. N. Vukosavic, "A method for magnetizing curve identification in rotor flux oriented induction machines", IEEE Transactions on Energy Conversion, Jun 2000. Vol. 15, pp 157-162.

[12] Magtrol, inc. "4603/4605 dynamometer operating instruction and 4615 digital readout instruction and reference manual", Magtrol, Buffalo N.Y.

Self-Oscillating Fluxgate Current Sensor with Pulse Width Modulated Feedback

Tomislav B. Šekara and Miroslav R. Mataušek

Abstract—**Several methods, based on the relay and phase-locked loop (PLL) experiment for determining the ultimate frequency, ultimate gain, and Nyquist curve Gp(iω), given arg(Gp(iω)), are analyzed. To support the practical application of these algorithms in the presence of the higher harmonics, measurement noise, and load disturbances, an adaptive filter (AF) of the band-pass type has been applied. The methods are tested on a large class of typical industrial processes. The SIMULINK realizations of the algorithms are presented.**

Index Terms—**PID controller, Frequency domain, Conventional relay, PLL.**

I. INTRODUCTION

THE method of generating stable oscillations for estimating the ultimate frequency ω_u and ultimate gain k_u of a process $G_p(s)$ is initiated by Ziegler and Nichols [1] in 1942. They proposed to use ω_u and k_u for dynamic characterization of a process $G_p(s)$ and for the experimental PI/PID controller tuning. Better realization of the Ziegler-Nichols method, proposed by Åström and Hägglund [2] in 1984, is known as the Conventional Relay (CR) experiment. The factors influencing the accuracy of estimation of ω_u and k_u by applying the CR experiment are: insufficiently filtered out higher harmonics by the process, presence of the load disturbance d and measurement noise n. The first drawback of the CR is removed in [3] by application of the Modified Relay (MR).

Further development of methods for determination of ω_u and k_u applies the principle of the phase locked loop (PLL) [4,5]. The PLL method from [4] removed almost all shortcomings present with the conventional relay experiment. Modifications of the basic relay-based and PLL-based structures of the previously discussed methods are shown in the figures Figs. 1-3.

It will be shown that application of an adaptive filter AF of the band-pass type in Fig. 1. results into a setup denoted by CR-f and allows determination of ω_u and k_u of process $G_p(s)$ by the conventional relay in the presence of load disturbances and measurement noise.

It will also be shown that application of this filter to MR (Fig. 2.) results into a setup denoted by MR-f and allows, in addition to a reliable determination of ω_u and k_u of process $G_p(s)$, also a reliable estimation of Nyquist curve $G_p(i\omega)$, given $\theta_{ref}=\arg\{G_p(i\omega)\}$, in the presence of load disturbances and measurement noise,.

By applying AF, upgrading of the PLL method from [5] is presented in Fig. 3.
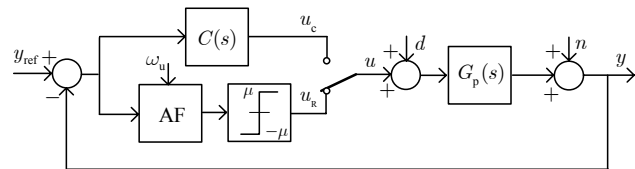
Fig. 1. Basic scheme of the conventional relay for determination of ω_u and k_u of process $G_p(s)$, denoted by CR for AF≡1. Modification CR-f is obtained for AF≠1.
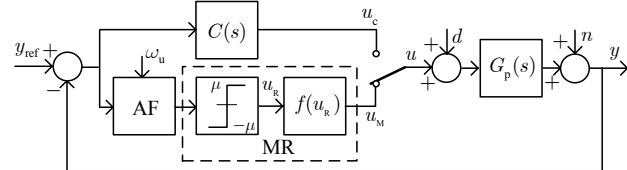

Fig. 2. Basic scheme of the modified relay for determination of ω_u and k_u of process $G_p(s)$, denoted by MR for AF≡1. Modification MR-f is obtained for AF≠1.
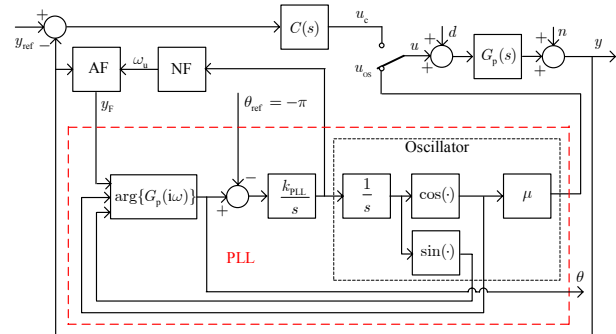

Fig. 3. Modified PLL-f scheme for determination of ω_u and k_u of process $G_p(s)$ involves an adaptive filter AF of the band-pass type and a low-pass filter NF. In original PLL scheme from [5] one cell of AF filter, shown in Fig. 7, is used, with NF≡1.

Finally, by applying AF, upgrading of the PLL method from [4] for determination of ω_u, k_u, and estimation of Nyquist curve $G_p(i\omega)$, given θ_{ref}, will be proposed, denoted by MPLL-f. Contrary to methods presented in Figs. 1-3, in the MPLL-f method breaking the loop of controller $C(s)$ in operation is avoided. Introduction of a low-pass filter NF makes the MPLL-f approach robust for determination of ω_u, k_u, and estimation of Nyquist curve $G_p(i\omega)$, given θ_{ref}.

T. B. Šekara and M. R. Mataušek are with the Faculty of Electrical Engineering, University of Belgrade, Belgrade, Serbia. (e-mail: tomi@etf.rs and matausek@etf.rs).

II. ANALYSIS

Modification of the basic schemes, involving conventional (CR) and modified (MR) relay, for determination of ω_u and k_u of process $G_p(s)$, includes an adaptive filter of the band-pass type. This means that in Fig. 1 and Fig. 2 block AF is realized by applying a cascade of filters defined by transfer function

$$F(s) = \prod_{m=1}^{4} \frac{\beta_m \omega_u s}{s^2 + \beta_m \omega_u s + \omega_u^2} , \quad \beta_m = 2\cos(\pi(2m-1)/16) \quad (1)$$

On the basis of harmonic analysis [6], characteristic equation of the conventional relay including filter (1) is

$$1 + \frac{4\mu}{\pi A_1} G_p(i\omega_u) F(i\omega_u) = 0 . \tag{2}$$

Since $F(i\omega_u)=1$, (2) reduces to

$$1 + \frac{4\mu}{\pi A_1} G_p(i\omega_u) = 0 . \tag{3}$$

From (2)-(3) it follows that estimates of the critical frequency and critical gain are equal to values ω_u and k_u of process $G_p(s)$. In (2)-(3)

$$k_u = \frac{4\mu}{\pi A_1} , \tag{4}$$

where A_1 is amplitude of the first harmonic of the Fourier expansion of the output signal of filter (1). Since a cascade of filters is a narrow band-pass filter, all harmonics except the fundamental $\omega=\omega_u$ are suppressed. The same applies for the high frequency measurement noise and load disturbances. This removes all shortcomings of the conventional relay experiment [2] mentioned earlier.

The necessary condition for stability of the limit cycle defined by relation (2) is given [7] by:

$$\left. \frac{\partial \operatorname{Im}(G_p(i\omega)F(i\omega))}{\partial \omega} \right|_{\omega=\omega_u} > 0 , \tag{5}$$

i.e. by

$$\left. \frac{\partial \operatorname{Im} G_p(i\omega)}{\partial \omega} \right|_{\omega=\omega_u} + \frac{2}{k_u \omega_u \beta_0} > 0 , \tag{6}$$

where $\beta_0 = 1 / \sum_{m=1}^{4} 1/\beta_m$ and k_u from (4) satisfies condition $k_u>0$.

Then, under condition that the solution defined by relation (3) satisfies the necessary condition for stability of the limit cycle, condition (6) is satisfied for the limit cycle defined by relation (2).

The structure shown in Fig. 3, in addition to the good properties as regards determination of ω_u and k_u and estimation of Nyquist curve $G_p(i\omega)$ for a given θ_{ref}, has the following shortcomings. Adjustment of parameter k_{PLL} in regulator k_{PLL}/s is dependent on the tested process $G_p(s)$. If the tested process is unstable, the structure of PLL of Fig. 3 is not applicable for any value of parameter k_{PLL}. Generalization of this concept involving PLL proposed in [4] is applicable also

to unstable processes. However, in both approaches [4,5], in the case of multiple solution of equation

$$\arg\{G_p(i\omega)\} = \theta_{ref} , \tag{7}$$

as well as for the solutions having $\arg\{G_p(i\omega)\}>2\pi$, the PLL concept requires a priori knowledge of the frequency of interest. This also means the following: if ω_u is being determined and one starts from an initial guess which is close to another solution of equation (7) for $\theta_{ref} = -\pi$, the ultimate frequency of the considered process $G_p(s)$ will not be determined. In this sense the concepts based on the relay principle have the advantage since they give unique solution, [8].

Figs. 4.-5. show the schemes involving PLL for determination of ω_u and k_u, and $G_p(i\omega)$ for given values $\theta_{ref}=\arg\{G_p(i\omega)\}$, of process $G_p(s)$ without breaking the loop of the controller in operation. Compared to the systems considered so far, in this approach regulator $C(s)$ is not disconnected, as done in Figs. 1.-3.

Improvement of the solution from [4], proposed in the present paper, consists of applying AF filter to avoid problems associated with measurement noise and load disturbances. This considerably simplifies the implementation and adequate application of the PLL concept to a closed-loop system with regulator $C(s)$ in operation with process $G_p(s)$. The solution proposed in [4] uses Kalman filter for eliminating influence of measurement noise and averaging technique for eliminating influence of load disturbances.

Application of the PLL concept to a closed-loop control system in Fig. 4, with inserted filter (1), follows directly from relations

$$\arg\left\{\frac{Y_F(i\omega)}{U_{OS}(i\omega)}\right\} - \arg\left\{\frac{U_{cF}(i\omega)}{U_{OS}(i\omega)}\right\} = \arg\{G_p(i\omega)\} \tag{8}$$

and

$$\left|\frac{Y_F(i\omega)}{U_{OS}(i\omega)}\right| \div \left|\frac{U_{cF}(i\omega)}{U_{OS}(i\omega)}\right| = |G_p(i\omega)| . \tag{9}$$
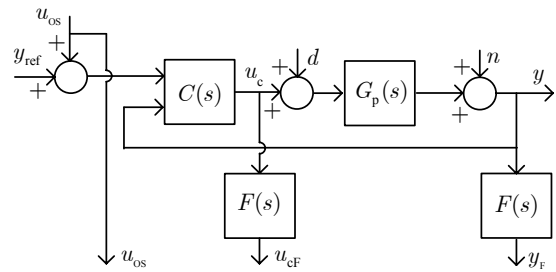

Fig. 4. Application of the PLL estimation of $G_p(i\omega)$ without braking the control loop in operation.

On the basis of (9), critical gain k_u is directly obtained from the ratio of fundamental harmonics of Fourier expansions of output signals u_{cF} and y_F from AF in Fig. 5,

$$k_u = A_{1cF} / A_{1F} . \tag{10}$$
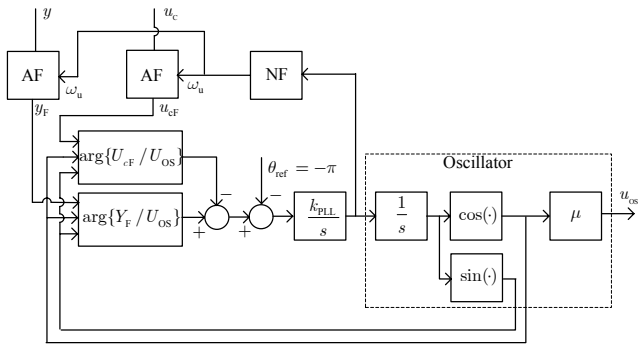
Fig. 5. Modified PLL estimator (MPLL-f), with adaptive band-pass filter AF and low-pass filter NF.


Fig. 8. Simulink scheme for determination of argument θ from interval $0 < θ < 2π$, where K1=1/β and AF/1 is single cell of AF filter for adopted β = √2.

III. SIMULATION RESULTS

A comparison of the previously analyzed methods is presented in Table 1 by taking fourteen representatives of the typical dynamic characteristics of industrial processes having transfer functions:

$$G_{p1}(s) = \frac{1}{(s+1)^4}, \ G_{p2}(s) = 1/\prod_{k=0}^{3}(0.7^k s+1), \ G_{p3}(s) = \frac{12.8e^{-s}}{16.8s+1},$$

$$G_{p4}(s) = \frac{e^{-5s}}{(s+1)^3}, \ G_{p5}(s) = \frac{10}{(s+1)(0.7s+1)(0.1s+1)}, \ G_{p6}(s) = e^{-\sqrt{s}},$$

$$G_{p7}(s) = \frac{1-2s}{(s+1)^3}, \ G_{p8}(s) = \frac{1}{\cosh\sqrt{2s}}, \ G_{p9}(s) = \frac{1}{s(s+1)^3},$$

$$G_{p10}(s) = \frac{9}{(s+1)(s^2+2s+9)}, \ G_{p11} = \frac{(s+0.2)e^{-0.5s}}{s^2+s+1},$$

$$G_{p12}(s) = \frac{4e^{-2s}}{4s-1}, \ G_{p13}(s) = \frac{e^{-s}}{s}, \ G_{p14}(s) = \frac{1.078e^{-10s}}{s^2+0.14s+0.49}.$$

The Simulink scheme shown in Fig. 6. is used, for determination of the frequency ω_u by the relay methods.
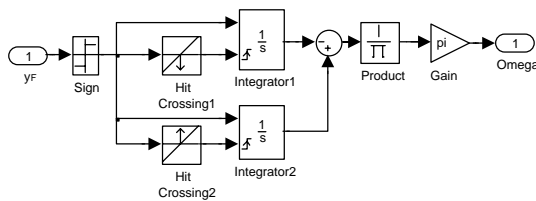
Fig. 6. Simulink scheme for determination of the frequency ω_u at the output of AF filter.
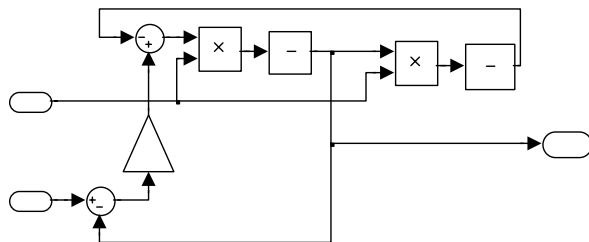
Fig. 7. Simulink scheme of AF/1 a single cell of AF filter.

TABLE 1
COMPARISON OF METHODS CR, MR, CR-F, MR-F, PLL-F AND MPLL-F FOR DETERMINATION OF ΩU AND KU OF THE REPRESENTATIVE TYPICAL INDUSTRIAL PROCESSES GPJ(S), J=1,...14.

$G_{pj}(s)$ ω_{uj}/k_{uj}	Exact	CR	MR	CR-f	MR-f	PLL-f	MPLL-f
ω_{u1}	1.000	0.993	1.000	1.000	1.000	1.000	1.000
k_{u1}	4.000	3.945	4.000	4.000	4.000	4.000	4.000
ω_{u2}	1.707	1.693	1.707	1.707	1.707	1.707	1.707
k_{u2}	4.659	4.581	4.659	4.659	4.659	4.659	4.659
ω_{u3}	1.608	1.616	-	1.606	1.608	1.608	1.608
k_{u3}	2.112	2.127	-	2.109	2.112	2.112	2.112
ω_{u4}	0.400	0.410	0.400	0.400	0.400	0.400	0.400
k_{u4}	1.249	1.262	1.249	1.249	1.249	1.249	1.249
ω_{u5}	3.684	3.613	3.684	3.685	3.684	3.684	3.684
k_{u5}	1.311	1.258	1.311	1.312	1.311	1.311	1.311
ω_{u6}	19.74	19.31	19.74	19.73	19.74	19.74	19.74
k_{u6}	23.14	22.43	23.14	23.13	23.14	23.14	23.14
ω_{u7}	0.845	0.788	0.845	0.845	0.845	0.845	0.845
k_{u7}	1.143	1.105	1.143	1.143	1.143	1.143	1.143
ω_{u8}	9.869	9.679	9.869	9.867	9.869	9.869	9.869
k_{u8}	11.59	11.26	11.59	11.59	11.59	11.59	11.59
ω_{u9}	0.577	0.567	-	0.577	0.577	0.577	0.577
k_{u9}	0.889	0.860	-	0.889	0.889	0.889	0.889
ω_{u10}	3.317	3.306	3.317	3.317	3.317	3.317	3.317
k_{u10}	2.667	2.643	2.667	2.667	2.667	2.667	2.667
ω_{u11}	3.613	3.700	3.613	3.610	3.613	3.613	3.613
k_{u11}	3.478	3.568	3.478	3.475	3.478	3.478	3.478
ω_{u12}	0.583	0.508	-	-	-	-	0.583
k_{u12}	0.634	0.566	-	-	-	-	0.634
ω_{u13}	1.571	1.571	-	1.571	1.571	1.571	1.571
k_{u13}	1.571	1.571	-	1.571	1.571	1.571	1.571
ω_{u14}	0.737	0.737	0.737	0.737	0.737	0.737	0.737
k_{u14}	0.108	0.108	0.108	0.108	0.108	0.108	0.108

As demonstrated in Table 1, all methods give good ω_u and k_u for the processes without the load disturbances and measurement noise. Efficiency of the MPLL-f for the unstable plant $G_{p12}(s)$ should be particularly emphasized.

Differences between these methods in the presence of the measurement noise and load disturbances, due to space limitation, will be illustrated using the process Gp1(s). When method MPLL-f was applied, PID regulator based on [9,10] was used.

a)

b)
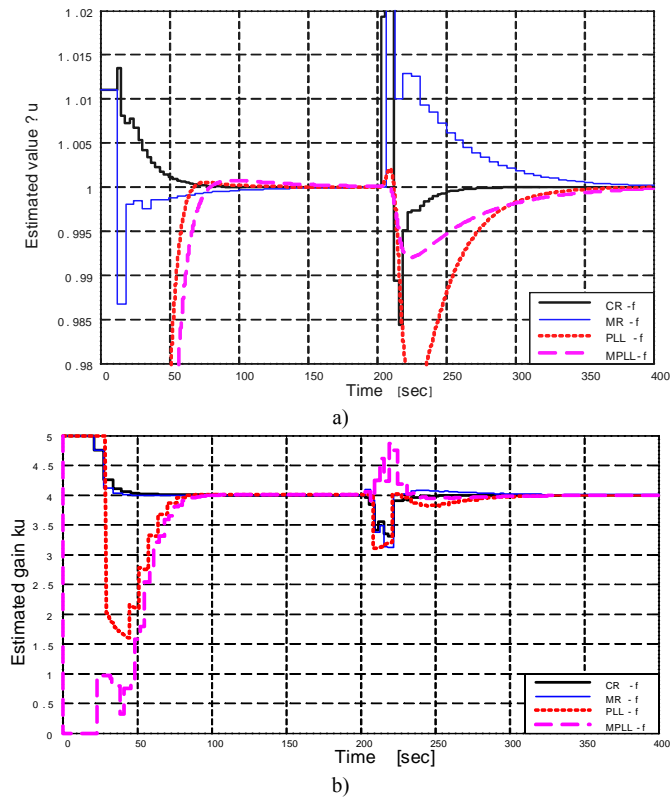
Fig. 9. Dynamic characteristics of estimated critical values for process $G_{P1}(s)$ in the presence of load disturbance d=2μ at instant t_0=200, applying methods CR-f, MR-f, PLL-f, and MPLL-f a) critical frequency ω_u and b) critical gain k_u. Time constant in the NF filter is T_{nf}=1.

However, it should be emphasized that the method MPLL-f is independent of the applied regulator. It is applicable to processes in the loop with the badly tuned PI or PID controller. In this case, on-line monitoring of parameters ω_u and k_u and a reliable estimate of Nyquist curve $G_p(i\omega)$, given values θ_{ref} =arg{$G_p(i\omega)$}, makes possible to perform fine tuning without interrupting the control loops in operation. In other words, an on-line adaptation is possible based on estimation offered by MPLL-f and by using PID optimization form [10] or tuning from [11].
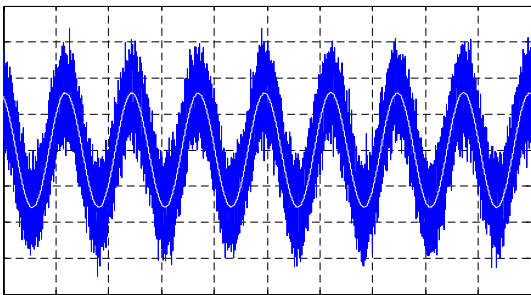
Fig. 10. Time diagram of the measured signal corrupted by noise of „random number" type of variance 0.01 and time diagram of the filtered signal y_f at the output of AF filter.

a)

b)
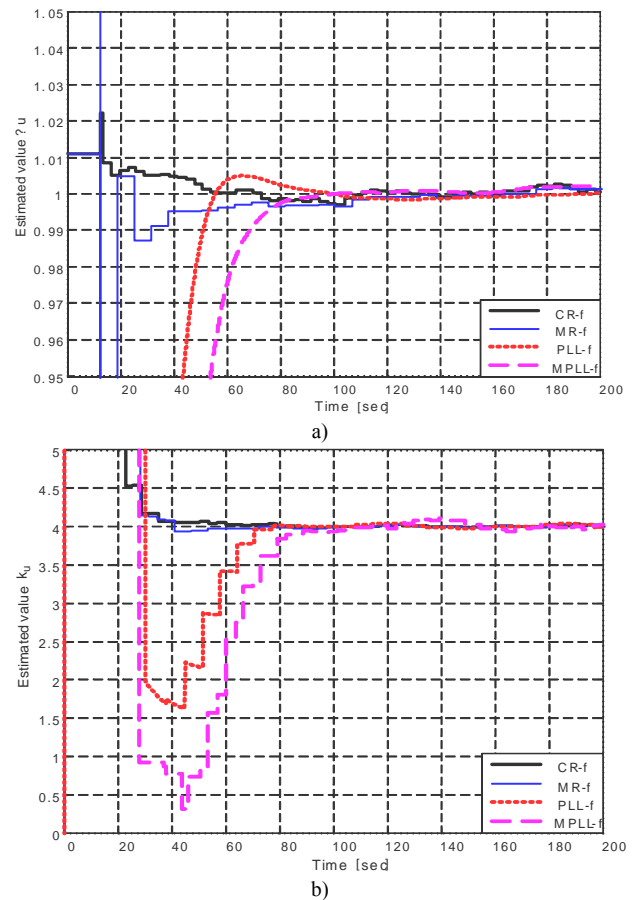
Fig. 11. Dynamic characteristics of the estimated critical values for process $G_{p1}(s)$ in the presence of measurement noise of "random number" type of variance 0.01, applying methods CR-f, MR-f, PLL-f, and MPLL-f a) critical frequency ω_u and b) critical gain k_u. In the NF filter T_{nf}=1.
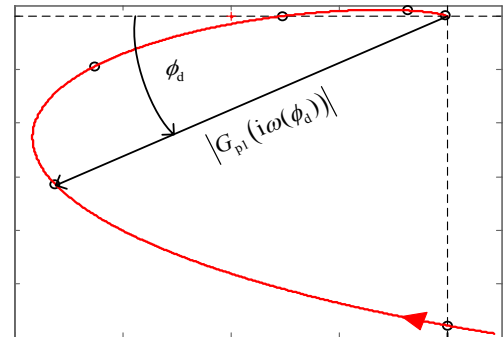
Fig. 12. Estimates of Nyquist curve $G_{p5}(i\omega)$, given values θ_{ref}=arg{$G_p(i\omega)$}= $-\pi + \phi_d$, ϕ_d=π/2, π/3, π/6, 0, -π/6, -π/3, by applying MR-f, PLL-f, and MPLL-f.

IV. CONCLUSION

The proposed modifications of the relay-based and PLL-based estimators, denoted by CR-f, MF-f, PLL-f and MPLL-f, showed adequate for a wide class of typical industrial processes. Highly accurate estimates of ω_u and k_u, and estimate of Nyquist curve $G_p(i\omega)$, given values θ_{ref}=arg{$G_p(i\omega)$}, are obtained in the presence of measurement noise and load disturbances.

In addition, this comparative analysis confirmed that by applying AF filter makes the relay-based estimators (CR-f, MR-f) effective in the presence of the load disturbances and measurement noise.

Finally, the proposed MPLL-f modification of the PLL method from [4], significantly simplifies determination of ω_u and k_u, and estimation of Nyquist curve $G_p(i\omega)$ for given values $\theta_{ref}=\arg\{G_p(i\omega)\}$, without breaking the control loops in operation. This makes possible fine tuning [11] of a controller while in operation.

REFERENCES

[1] J.G. Ziegler, N.B. Nichols, Optimum settings for automatic controllers, *Trans. ASME*, Vol. 64, pp. 759-765, 1942.

[2] K.J. Aström, T. Hägglund, Automatic tuning of simple regulators with specifications on phase and amplitude margins, *Automatica*, Vol. 20, pp. 645-651, 1984.

[3] T.H. Lee, Q.G. Wang, K.K. Tan, A modified relay-based technique for improved critical point estimation in process control, *IEEE Trans. Control Syst. Technology*, Vol. 3, pp. 330-337, 1995.

[4] J. Crowe, M.A. Johnson, Process identifier and its application to industrial control, *IEE Proc. Control Theory Appl.*, Vol. 147, pp.196-204, 2000.

[5] D.W. Clarke, J.W. Park, Phase-locked loops for plant tuning and monitoring. *IEE Proc. Control Theory Appl.*, Vol. 150, pp. 155-169, 2003.

[6] E. P. Popov, I.P. Pal'tov, *Approximate Methods of Investigation of Nonlinear Automatic Systems* M.: Fizmatgiz, 1960. (in Russian)

[7] J.M. Loeb, *Recent advances in nonlinear servo theory*, New York: Macmillan, 1965.

[8] T.B. Šekara, M.R. Mataušek, Relay-based critical point estimation of a process with the PID controller in the loop, Submitted for publication to Automatica (2010)

[9] T.B. Šekara and M.R. Mataušek, "Optimization of PID controller based on maximization of the proportional gain under constraints on robustness and sensitivity to measurement noise", *IEEE Trans. Automatic Control*, Vol. 54, pp.184-189, 2009.

[10] T.B. Šekara and M.R. Mataušek, "Revisiting the Ziegler-Nichols process dynamics characterization", *J. Process Control,* Vol. 20, pp. 360-363, 2010.

[11] M.R. Mataušek, T.B.Šekara, PID controller frequency-domain tuning for stable, integrating and unstable processes, including dead-time, *J. Process Control* (2010), doi:10.1016/j.jprocont.2010.09.00

Infrared Transceiver for Home Automation

Ivana Šenk, Laslo Tarjan, Gordana Ostojić, and Stevan Stankovski

Abstract—**In home automation there is often a need for control of devices that have a built-in receiver for infrared communication with a remote controller. When trying to integrate such devices in a single control system, it is possible to substitute the remote controller with another infrared transmitter which automatically controls the device. This paper suggests a solution with an infrared transceiver which is connected to a computer via the USB interface. The receiving part records commands from the remote controller, while the transmitting part takes the role of the remote controller, and provides direct device control from the computer, or indirect control through the computer network. This system provides efficient and simple control of the home devices in the absence of the user.**

Index Terms—**About Infrared communication, remote control, home automation.**

I. INTRODUCTION

HOME automation (the following terms are also used: house control, domotics, smart home, intelligent home) is a set of devices, systems or subsystems in a residential environment that are linked in a unique system, which enables automatic control of individual devices or systems [1].

The reasons for implementing home automation are various, it can increase security of a house, provide energy savings, provide centralized device control, provide device control in the absence of the user, etc. Development of home automation was mainly initiated by the need for security, so various alarm systems were developed, which ensure house supervision, and in case of any security risk, they activate the alarms, call telephone numbers, etc. For security purposes various other systems were developed, such as systems that simulate the presence of users. In such systems, in the user absence, the blinds are raised or lowered, and lights, audio and video equipment are turned on or off at specified time.

Today, home automation includes various systems [2], such as control of lighting, air conditioning or blinds, security systems, control of audio or video devices, automated flower watering or pet feeding, etc. Also, various access control systems are included in home automation, such as automated control of a garage door or unlocking the entrance door automatically, e.g. with the use of RFID technology [3]. All of these systems can be connected either by wires or wirelessly.

I. Šenk, L. Tarjan, G. Ostojić (e-mail: goca@uns.ac.rs) and S. Stankovski (e-mail: stevan@uns.ns.ac.rs) are with the Faculty of Technical Science, Novi Sad, Serbia.

As a large number of home devices have a built-in possibility of remote control, it is convenient to use this possibility when introducing an automated control system.

Most devices have a built-in infrared receiver for remote control, which enables easy integration of such devices in a home automation system, without the need for additional network installation. In this paper a solution is proposed, which substitutes a remote controller with an infrared transmitter that connects to the USB port of the computer and enables automated device control from the computer, or indirect control through the computer network.

II. INFRARED COMMUNICATION FOR REMOTE CONTROL OF DEVICES

Infrared communication [4] is a wireless communication which requires optical visibility, i.e. the transmitter and the receiver must be in direct line of sight, and no objects can stand between them. This type of communication is used for connecting devices in short range, usually in a same room.

Producers of home devices have developed and use different protocols for infrared communication and remote control [5]. All of these protocols for remote control use digitally modulated signal. The carrier frequency of the signal can vary, but in 90% of the cases the frequency of 38 kHz is being used [6].

For control of audio and video devices, most widely used are the Philips RC-5 (in Europe and USA) and NEC protocol (in Japan).

Philips RC-5 protocol [5] defines the carrier frequency of 36 kHz, constant bit length of 1.778 ms and message length of 14 bits. For signal encoding, bi-phase modulation (Manchester code) is being used (Figure 1), where each bit is represented by a certain state switch. Logical „one" is represented by a switch from low to high signal state, and a logical „zero" is represented by a switch from high to low signal state. High signal state is represented by the existence of the carrier frequency signal, while the low signal state is represented by its absence.
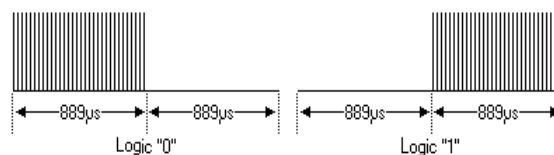

Fig. 1. Bi-phase modulation (Manchester code) – a logical „zero", and logical „one".

According to this protocol, a message (Figure 2) starts with two start bits with logical „one" value. The third bit is a

„toggle" bit, which is inverted every time when a key of the remote controller is released and pressed again. The following five bits represent the device address, and the last six bits represent the command itself.


Fig. 2. Philips RC-5 protocol – message.

If the key of the remote controller is still pressed, the whole message is sent again after 114 ms. In this case, the „toggle" bit stays at the same logical level, so the receiver can understand that it is the same message, and not double activation of the same key.

NEC protocol [5] defines the carrier frequency of 38 kHz, bit length of 1.125 ms (logical „zero") or 2.25 ms (logical „one"). For signal encoding, pulse distance encoding is used (Figure 3), where each bit is represented with high signal state for 562.5 µs, followed by low signal state for 562.5 µs for a logical „zero" or 1.6875 ms for a logical „one".
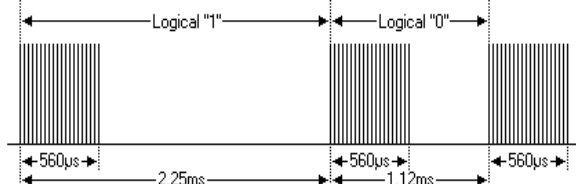
Fig. 3. Pulse distance encoding – a logical „zero", and logical „one".

According to this protocol, a message (Figure 4) starts with a pulse that lasts 9 ms, followed by a pause of 4.5 ms. The following 8 bits represent the device address, and they are followed by 8 bits representing the inverted device address, that can be used for verification of data. After that, the following 8 bits represent the command itself, again followed by 8 bits representing the inverted command, for verification of data. At the end of the message is a pulse 562.5 µs long. The time for sending one message is constant, as every bit is sent twice – noninverted and inverted.

Fig. 4. NEC protocol – message.

The message is sent only once, even if the key of the remote controller is kept pressed. In that case (Figure 5) the message is followed by a code that consists of a pulse of 9 ms, pause of 2.25 ms and a pulse of 562.5 µs, which is repeated every 110 ms.
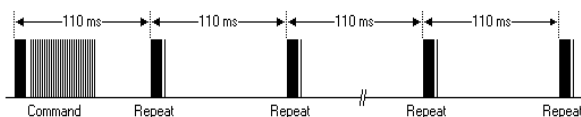

Fig. 5. A message followed by a code that is repeated every 110 ms.

III. REALIZATION OF AN INFRARED TRANSCEIVER FOR HOME AUTOMATION

In this paper, a solution for an infrared transceiver is presented, which connects to the computer through the USB interface, and enables integration of various devices that can be controlled by infrared signals in a complete system of home automation. A transceiver has been realized, and its final layout can be seen in Figure 6. The transceiver consists of two functional units – a transmitter and a receiver of infrared signals.
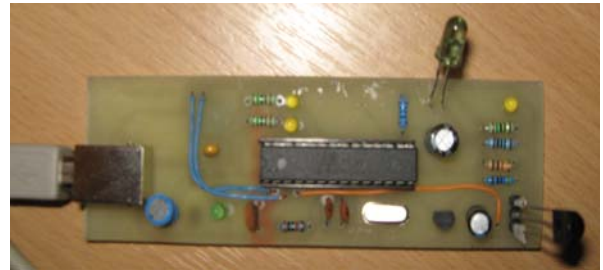
Fig. 6. Infrared transceiver.

The receiving unit detects infrared signals from the remote controller, and enables control of the computer with the remote controller or recording commands from the remote controller for further control of the devices. For registering infrared signals an integrated chip SFH 5110-38 is used. This integrated chip consists of a photodiode, preamplifier, automatic gain control, bandpass and demodulator, and is in a housing designed as daylight-cutoff filter. The integrated chip SFH 5110 exists in several versions, depending on the signal carrier frequency, and can detect signals of carrier frequency between 30 and 40 kHz. For realization of the receiving unit the chip that detects signals of carrier frequency of 38 kHz is chosen, as it is the most frequently used carrier frequency in remote controllers. Output from this chip is the signal itself, without the carrier frequency, and this signal is led to the microcontroller pin.

The transmitting unit is used for sending infrared signals and automatic control of devices instead of the remote controller. The signal is generated from the microcontroller, and sent via an infrared LED.

Central part of the infrared transceiver is the microcontroller Atmel AVR ATmega8, which integrates the receiving and transmitting unit, and connects them with the computer through the USB interface. Connection with the computer is established through the integrated chip FT232RL, which converts USB communication to RS232 serial communication, which is supported by the microcontroller. This chip enables the computer to see the device as a virtual COM port, through which communication can be established in the same way as through a hardware COM port.

Microcontroller program consists of receiving and storing data from the receiving unit, sending the signal to the transmitting unit, and RS232 serial communication with the computer.

Signal receiving is performed in the interrupt routine of the external interrupt, which is invoked each time when the state

on the external interrupt pin changes. The signal is stored through the time interval of a certain state on the external interrupt pin, as in the interrupt routine the time interval from the previous state change is written in the array each time the interrupt, i.e. the state change on the pin, occurs. As various remote controllers function based on different protocols and send messages of different length, the array should allocate enough memory to ensure that the complete message is stored. When the message is stored, the data from the array are sent to the computer via the serial communication, to enable storing of the message in a database on the computer.

Sending of the signal through the transmitting unit is performed through the opposite process. First the message to be sent is received from the computer, and is stored in a variable array. This message is identical to the one that the microcontroller sent to the computer when recording the message from the remote controller. The carrier frequency of the output signal is adjusted by the function generator of the microcontroller timer, and the signal itself is generated by turning on or off the output pin of the timer in the time intervals stored in the array that represents the message. As the frequencies of the signal changes are high, the microcontroller cannot simultaneously send and receive data, but can be in either receiving or sending mode. When the power is switched on, the microcontroller is in receiving mode, and stays that way until it receives a command from the computer to switch to the sending mode.

Microcontroller ATmega8 has an integrated support for RS232 serial communication, which is used in this case. It is necessary to set the communication speed, number of data bits, stop bits and the parity bit. The highest communication speed of 115200 bps has been chosen, which is possible as the external oscillator of 7.3728 MHz is used, furthermore, 8 data bits, one stop bit and no parity bit have been chosen.

IV. APPLICATION FOR COMMUNICATION WITH THE INFRARED TRANSCEIVER

In order to connect the devices controlled by the infrared transceiver in one control system, an application in Visual Basic .NET has been developed for Windows operating system, which enables communication between the computer and the transceiver.

This application communicates with the transceiver through serial RS232 communication via the virtual COM port. The settings of the serial communication are: baud rate of 115200 bps, 8 data bits, 1 stop bit, no parity bit. Through serial communication, by sending a certain command, the user can set the desired working mode of the microcontroller (receiving or sending of infrared signal). If the microcontroller is in the receiving mode, it is possible to send a command from the application that enables reading of the message currently stored in the microcontroller. Then the message is stored in a data array on the computer, and can be drawn on the graph. Figure 7 shows part of the application which receives the message from the microcontroller, where one message record

can be seen. The upper graph shows the recorded array itself, where each array element represents the length of the time interval between two state changes. The lower graph shows the data array transformed to the real signal. In the figure it can be noticed that for this remote control protocol it is possible to record five times the repeated message, while for some other protocols, in the same array it is possible to record the message only once. The recorded array can be saved in the database with adequate connection with the device name and the function to which this message applies.
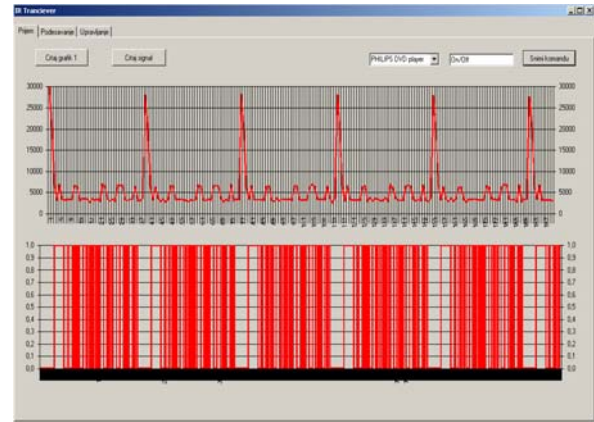
Fig. 7. Application for communication with the infrared transceiver (receiving part).

When the database has saved commands for a certain device, the application can be used to set the command to the microcontroller to change the mode to the sending mode, and to send the message to be sent from the transceiver and

perform a function on the end device (Figure 8). When transiting to the part of the application for device control, the command for switching to the sending mode is sent to the microcontroller. In this part of the application it is possible to choose the desired device from the database of available devices, and the function which should be performed from the list of saved messages. Then the message is stored in the temporary array, which is then sent to the microcontroller in the appropriate format, via the virtual COM port.


Fig. 8. Part of the application for sending commands.

In this application it is still required to provide the possibility to control the devices through the computer network, which would enable full automated control that could be realized even in the absence of the user. Furthermore, it is possible to add an application part for programming

control in certain time, for example for setting the start and end of recording a certain program on the DVD recorder, turning on or off the TV or the audio device at a certain time, etc.

V. CONCLUSION

In home automation it is often required to integrate devices that have a built-in infrared receiver intended for remote control to an automated control system. In order to integrate such devices as easy as possible in a complete control system, it is possible to substitute the remote controller with another infrared transmitter which would automatically control the device.

In this paper an infrared transceiver is suggested, which connects with the computer via the USB interface. This transceiver can store commands from the existing remote controller, send them to the computer where they are stored in an adequate database, and on request it can also send commands to the transmitting unit. As most of the devices widely used, use infrared signals with a carrier frequency of 38 kHz, the solution in this paper can be implemented for control of common TV, video and audio devices in a home. Such a transceiver can completely substitute the existing remote controller and provide simple control of devices, even in the user absence.

The advantage of using such a transceiver is that it does not depend on the protocol used by the device for communication with the remote controller, but only on the carrier frequency, as the command is stored in the form as it is being sent from the original remote controller, and in that form it sends the command when requested.

The disadvantage of using such a transceiver in home automation is the request for optical visibility between the transmitter and the receiver on the device, so in the case of controlling multiple devices, more transmitting diodes must be implemented, where each would point the adequate direction.

REFERENCES

[1] J. Gerhart, "Home automation and wiring", McGraw-Hill 1999.
[2] A. Varma, Domotics: Smart technology, smarter homes, ICFAI University Press 2008.
[3] Ostojić G., Stankovski S., Rakić-Skoković M., Lazarević M., Jovanović V: "Building automation with the usage of RFID tech. for the user identification", 14. International Scientific Conference on Industrial Systems - IS, Novi Sad: Faculty of Technical Sciences, 2008.
[4] T. B. Zahariadis, "Home networking technologies and standards", Artech house, Inc. 2003.
[5] http://www.sbprojects.com/knowledge/ir/ir.htm, accessed 20. 11. 2010.
[6] http://www.lirc.org/, accessed 20. 11. 2010.

An Analytical Model of Inversion Layer Quantization and Gate Oxide Quantum Mechanical Tunneling in Nano-p-MOSFETs

Amit Chaudhry and Jatinder N. Roy

Abstract—In this paper, an analytical model has been developed to study energy quantization in p type Metal Oxide Semiconductor Field Effect Oxide (MOSFETs). Inversion-layer quantization has been modeled using variation and triangular well approach for n-MOSFETs and p-MOSFETs respectively. The inversion charge density for holes has been found to be much lesser than the electron inversion charge density. The gate capacitance has also been evaluated for p-MOSFETs. It has been found that the inversion layer capacitance of holes in p-MOSFET is lesser than the inversion layer electrons in n-MOSFETs and hence the gate capacitance is much lesser in p-MOSFETs. The hole tunneling across the gate oxide has also been computed. It has been found to be much lesser than the electron tunneling in n-MOSFETs. All the results have been compared with the reported numerical results in the literature.

Index Terms—CMOS, Inversion quantization, BSIM, Holes, Capacitance.

I. INTRODUCTION

MOSFETS modeling is facing difficulties to achieve accurate description of extremely scaled down devices. The reason is that many complicated new phenomena are arising which are not easy to describe. One such phenomenon arising out of down scaling the MOSFET is the failure of classical physics at nanoscale. n-MOSFETs have been studied a lot and at length at nanoscale since their evolution in early 1950s [1]-[5]. Since then scaling down of both p-MOSFETs and n-MOSFETs has been taking place for their use in Complementary Metal Oxide Semiconductor (CMOS) technology. Very less attention has been given to the modeling process of p-MOSFET in lower geometries mainly because of the complex band structure of the valence band. At nanoscale geometries, the electrical fields at the oxide/substrate interface become very high. This is due to extremely thin oxide and high doping concentration in the substrate. This results in the charge carriers occupying quantized two-dimensional sub-bands which behave differently from the classical three-dimensional case. So, the

complexity of the valence band further increases. The valence bands under very high electrical fields at the oxide/silicon interface tend to mix up or intermingle and hence simple approach to study hole inversion layers has not been dealt with. Due to this reason, the hole inversion layers have not been studied analytically but mainly experimental work has been done and whatever, theoretical work done already has yielded complex solutions not suitable for device simulation [6]-[13]. This makes simple formulations of hole quantization much more difficult to calculate accurately. Moreover, step wise step analytical formulation is missing in most of the literature yielding very less information about the hole quantization modeling process.

An attempt has been made in this paper to give a simple and yet accurate description of the energy quantization process for both n-MOSFET and in a p-MOSFET. Further, effects on the gate capacitance and gate oxide hole tunneling have also been considered.

II. ENERGY QUANTIZATION

A. n-MOSFET

The research in the area of energy quantization started in the early 1950s. The research [1-5] mainly focused on only calculating the inversion charge density in the presence of energy quantization effects using variation approach and triangular well approach in the MOSFET. The use of such techniques required the calculation of surface potentials at the interface of silicon and its oxide. The lack of availability or slow development of surface potential models six decades ago, never allowed the growth of research in the area of modeling inversion layer quantization in MOSFETs. But as the MOSFETs are being scaled down to the nm scale, the need of research has risen, to analytically model the MOSFETs under inversion layer quantization conditions.

Solving the Poisson equation in the electron inverted channel for n-MOSFET, we get the total charge density Q_s.

$$Q_s = -\left(2qN_a\varepsilon_{Si}\varepsilon_0\right)^{1/2}\left[\varphi_s + V_t e^{-2\varphi_f/V_t}\left(e^{\varphi_s/V_t} - 1\right)\right]^{1/2} \tag{1}$$

Similarly, the depletion charge Q_b is approximated as

$$Q_b = -\left(2\varepsilon_{Si}\varepsilon_0 qN_a\varphi_s\right)^{1/2}. \tag{2}$$

A. Chaudhry is with University Institute of Engineering and Technology, Panjab University, Chandigarh, India (e-mail: amit_chaudhry01@yahoo.com).
J. N. Roy is with Solar Semiconductor Private Limited, Hyderabad, India (e-mail: jatin.roy@solarsemiconductor.com).

Therefore the inversion charge density Q_{inv} is given by (1)–(2):

$$Q_{inv} = -\gamma C_{ox}\left[\left\{\varphi_s + \frac{kT}{q}\exp\left(\frac{q\left(\varphi_s - 2\varphi_f\right)}{kT}\right)\right\}^{1/2} - \varphi_s^{1/2}\right] \quad (3)$$

γ – body effect parameter, C_{ox} – oxide capacitance, φ_s – surface potential, φ_f – Fermi potential, N_a – substrate concentration, $V_t = kT/q$ – thermal voltage.

The main problem with equation (3) is that the surface-potential has to be evaluated explicitly in all the regions of inversion and then only, the equation (3) can be solved. An explicit solution has been evaluated in the [14].

The wave function solution of the Schrödinger's equation is given using variation approach is [1] to study electron inversion layers as:

$$\Psi(x) = \frac{b^{3/2}x}{\sqrt{2}}\exp\left(-\frac{bx}{2}\right) \quad (4)$$

where b is a constant and given by

$$b = \frac{\left[48\pi^2 m^* q^2\left\{\frac{11}{32}n_{inv} + n_{dep}\right\}\right]^{1/3}}{\varepsilon_{Si}\varepsilon_0 h^2}$$

where: m^* – effective longitudinal mass of electron in $<100>=0.98m_0$, $n_{inv}=Q_{inv}/q$ – inversion electron concentration, $n_{dep}=Q_b/q$ – depletion charge concentration.

The corresponding shift in the energy [1] is given by

$$E_{oe} = \frac{3h^2 b^2}{8m^*} \quad (5)$$

The shift in the surface potential is

$$\delta\varphi_{se} = \frac{E_{oe}}{q} \quad (6)$$

The equation (6) is then included in the explicit surface potential expression given by [14] and the total surface potential is obtained. Then a model of quantum inversion charge density is obtained from equation (3) by including surface potential from [14].

$$Q_{invqm} = -\gamma C_{ox}\left[\left\{\varphi_{sqm} + \frac{kT}{q}\exp\left(\frac{q\left(\varphi_{sqm} - 2\varphi_f\right)}{kT}\right)\right\}^{1/2} - \varphi_{sqm}^{1/2}\right] \quad (7)$$

where φ_{sqm} is the quantum surface potential [14].

B. p-MOSFET

The hole inversion layers are studied using the triangular well approximation for solving the Schrödinger's equation [15].

$$E_i = \left(\frac{h^2}{8m_1\pi^2}\right)^{1/3}\left[1.5\pi qE_s\left(i + \frac{3}{4}\right)\right]^{2/3} \quad (8)$$

E_i – airy function, $E_s=(\eta Q_{inv}+Q_{depl})/\varepsilon_{Si}\varepsilon_0$ – surface electrical field, $\eta=0.8$ – for holes [15], $m_1=0.16m_0$ [16] for (100) surface.

The equation (8) gives the energies of the holes in the quantized potential well at the Si/SiO$_2$ interface. The hole energy in the first energy state can be found by putting $i=0$ in equation (8)

$$E_{oh} = \left(\frac{h^2}{8\pi^2 m_1}\right)^{1/3}\left(1.1\pi qE_s\right)^{2/3}. \quad (9)$$

The shift in the surface potential is obtained using equation (6) as:

$$\delta\varphi_{sh} = \frac{E_0}{q} \quad (10)$$

The equation (10) is then included in the explicit surface potential expression given by [14] and the total quantum surface potential is obtained and the quantum inversion charge density is obtained given by equation (7).

Energy quantization effects on carrier distribution in n-MOSFET and p-MOSFET are studied and analytically modeled. The results in Fig. 1 show that the hole density is much lower than the electron density showing that the energy quantization effect is more severe in p-MOSFETs than the n-MOSFETS. This is due to the smaller effective mass perpendicular to Si/SiO$_2$ interface for inversion-layer holes on a (100) surface as compared to the electron effective mass. The electron inversion layers are matched with the BSIM 5 results [16].

III. C-V MODELING

Approximating the inversion charge density for the weak inversion region and strong inversion regions separately, we get after differentiating the equation (7) with respect to surface potential, the weak inversion and strong inversion capacitances as:

The inversion capacitance in the presence of energy quantization is

$$C_{invqm} = \frac{C_{wi}C_{si}}{C_{si} + C_{wi}} \quad (11)$$

where: $C_{wi}=(q/kT)Q_{invqm}$ is the weak inversion capacitance, $C_{si}=(q/2kT)Q_{invqm}$ is the strong inversion capacitance, and
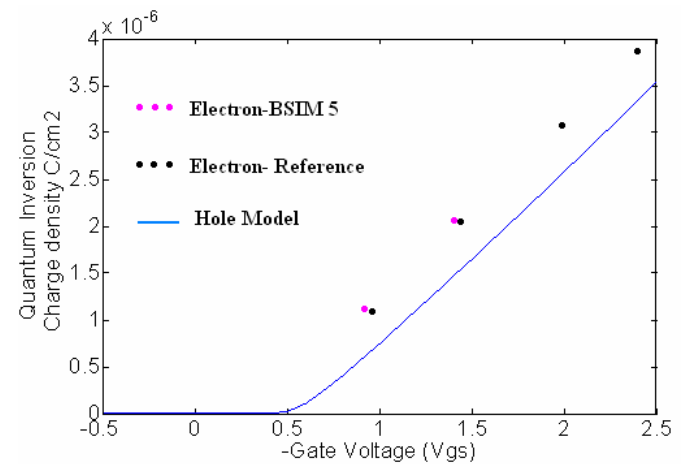

Fig. 1. Simulated results of quantum mechanical electron inversion charge density using variation approach and hole inversion charge density using triangular well approach.

Q_{invqm} – quantum inversion charge density from the equation (7).

Total quantum gate capacitance is equal to

$$\frac{C_{ox}\left(C_d + C_{invqm}\right)}{C_{ox} + C_d + C_{invqm}} \tag{12}$$

where C_{ox} – oxide capacitance, C_d – depletion capacitance obtained by differentiating (2) with respect to surface potential.

Energy quantization effects on gate capacitance in n-MOSFET and p-MOSFET are studied and analytically modeled. The results in Fig. 2 show that the hole gate capacitance is much lower than the electron density showing that the energy quantization effect is more severe in p-MOSFETs than the n-MOSFETS. The hole gate capacitance matches closely with the numerical results [7].

IV.   GATE OXIDE HOLE TUNNELING

In extremely scaled oxides, the charge carriers in the inverted channel directly tunnel into the gate oxide. A model has been developed which describes the gate oxide tunneling using the Wentzel-Krammers-Brillouin (WKB) approach [17,18]. Energy quantization effect has been included in the gate tunneling model to accurately measure the direct gate tunneling density. The developed model considers both electron and hole tunneling in the gate insulators for n-MOSFETs and p-MOSFETs respectively.

A.   n-MOSFET

The main issue in the current density calculation is transmission probability $T(E)$. The general expression for the transmission probability is given by [17, 18]:

$$T(E) = \exp\left[-2\int_{x_1}^{x_2} |k(x)|\, dx \right] \tag{13}$$

where $k(x)$, wave factor is given by
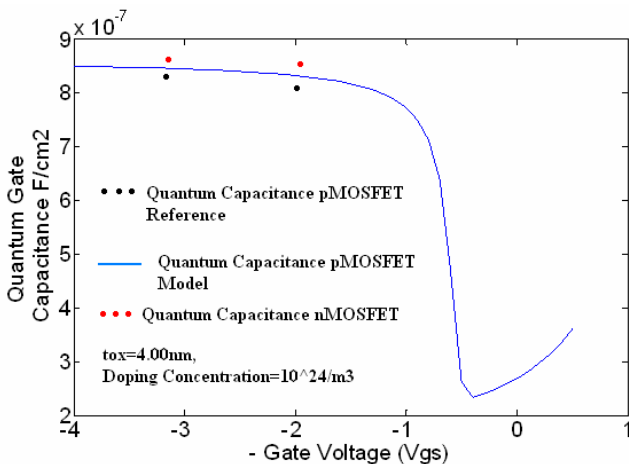
Fig. 2. Simulated results of the gate capacitance (F/cm^2) including energy quantization in the substrate. The reference is reported in [7]. The parameters are oxide thickness=4nm and substrate doping =1x10^{18}/cm^3.

$$\left[\frac{2m_{ox}\left(V(x) - E\right)}{\hbar^2} \right]^{1/2}$$

where $m_{ox}=0.32m_0$ is the effective electron mass in the silicon oxide [19], $\hbar$ – effective Planck's constant.

The direct tunneling current density in the gate oxide is given as [18]

$$J_T = \frac{4\pi m_t q}{h^3} \int_0^V \left\{ \int_0^\infty \left[f_S(E) - f_D(E) \right] dE_t \right\} T(E_x)\, dE_x \tag{14}$$

where: $f_S(E)=1/\{1+exp(E-E_{fs})/kT\}$ – electron distribution at the source/substrate interface, $f_D(E)=1/\{1+exp(E-E_{fd})/kT\}$ – electron distribution at the drain/substrate interface, E_{fs} – Fermi energy at the source, E_{fd} – Fermi energy at the drain, E – total energy of the electrons, E_x – energy in the direction of tunneling, i.e. from source to drain, E_t – energy in transverse direction, and $m_t=0.19m_0$ – electron transverse mass.

Using (13) and (14), the tunneling current density in the gate oxide can be calculated.

B.   p-MOSFET

The hole tunneling into the gate oxides becomes important when the p-MOSFET are operated in the circuits such as CMOS inverters. The process of the hole tunneling process in the valence band is the same as that for electrons in the conduction band. The most significant difference between electron tunneling and hole tunneling lies in the average barrier height. Holes face a barrier from the valence band edge of silicon to the valence band edge of gate oxide. This barrier is more in case of valence band tunneling.

The parameters used for the calculation for the hole tunneling are transverse mass of hole in silicon $m_h*=0.45m_0$ [20], hole mass in oxide $m_{hox}= 0.30m_0$ [20], oxide barrier height for holes $E_b=4.5eV-qVox/2$, where V_{ox} – oxide potential.

In Fig. 3, the hole tunneling current density in a p-MOSFET is smaller than the electron tunneling current density in an n-MOSFET because of the high barrier height and large effective transverse mass for holes. The results match quite closely with the reported results from the reference [20].

V.   CONCLUSION

A detailed study has been done to evaluate the electrical parameters like C-V and inversion charge density in the p-MOSFETs. Based on the variation approach and triangular well approach, all these parameters have been derived. In the presence of energy quantization, the inversion charge capacitance has been obtained. The total gate capacitance with quantum mechanical effects in p-MOSFETS reduces as compared to the n-MOSFETs. This is due to reduced charge density at interface of the substrate and the oxide. The tunneling of holes into the oxide cannot be ignored which increases as the oxide thickness falls but it is lesser than the electron gate oxide tunneling.
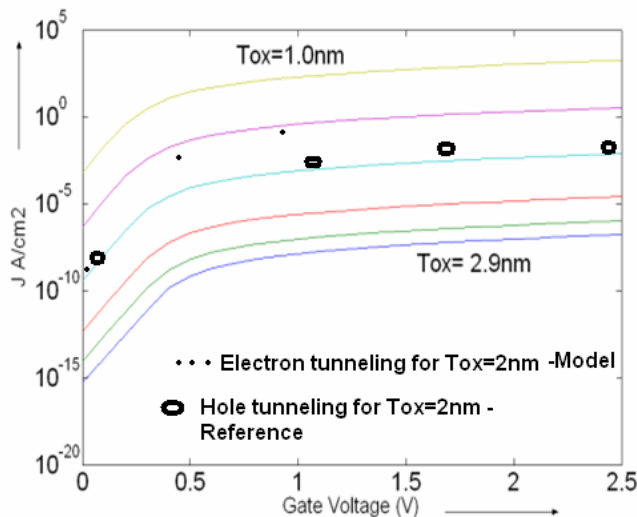
Fig. 3. Gate hole tunneling current density at various gate to source voltages $|V_{gs}| = (0\text{-}2.5\text{V})$ at substrate donor concentration (N_d=4x10^{17}/cm^3) and oxide thickness varying as 2.9nm, 2.75 nm, 2.48nm, 2.0 nm, 1.5nm to 1.0 nm.

REFERENCES

[1] Stern F., "Self-consistent results for n-Type Si inversion layers", Physics Review B, Vol. 5, No. 12, pp. 4891–4899, June 1972.
[2] Fang F. F. and Howard W. E., "Negative field-effect mobility on (100) Si surfaces", Physics Review letters, Vol. 16, No. 18, pp. 797–799, 1966.
[3] Stern F. and Howard W. E.," Properties of Semiconductor Surface Inversion Layers in the Electric Quantum Limit", Physical Review, Vol. 163, No. 3, pp. 816–815, Nov. 1967.
[4] Stern F.,"Surface quantization and surface transport in semiconductor inversion and accumulation layers,' Vacuum Science and Technology, Journal of, Vol. 9, No. 2, pp. 752–753.
[5] Ando T., Fowler A. B., Stern F.," Electronic properties of two-dimensional Systems", Review of Modern Physics, Vol. 54, No. 2, pp. 437–672, April, 1982.
[6] Takagi S. et al, "Characterization of Inversion-Layer Capacitance of Holes in Si MOSFET's", Electron devices,IEEE transactions on, Vol. 46, No. 7, pp. 1446–1450, July 1999.
[7] Jlallepalli S. et al, " Effects of quantization on the electrical characteristics of deep submicron p- and n- MOSFETs", VLSI technology, Symposium on, pp. 138–139, 1996.
[8] Chindalore G. et al, "Experimental Determination of Threshold Voltage Shifts Due to Quantum Mechanical Effects in MOS Electron and Hole Inversion Layers" Electron Device Letters , IEEE journal of , Vol. 18, No. 5, pp. 206–208, May 1997.
[9] Hareland S. et al, "A Physically-Based Model for Quantization Effects in Hole Inversion Layers", Electron Devices, IEEE Transactions on, Vol. 45, No. 1, pp. 179–186, Jan. 1998.
[10] Hou T. et al, "A Simple and Efficient Model for Quantization Effects of Hole Inversion Layers in MOS Devices", Electron Devices, IEEE Transactions on, Vol. 48, No. 12, pp. 2893–2898, Dec. 2001.
[11] Hou T. and Li M., "Hole Quantization and Hole Direct Tunneling in Deep sub micron p-MOSFETs", IEEE, pp. 895–900, 2001.
[12] Hou T. and Li M., "Hole Quantization effects and Threshold Voltage Shift in pMOSFET—Assessed by Improved One-Band Effective Mass Approximation", Electron Devices, IEEE Transactions on, Vol. 48, No. 6, pp. 1188–1193, June 2001.
[13] Hu C. et al, "Quantization Effects in Inversion Layers of PMOSFET's on Si (100) Substrates", Electron device letters, IEEE, Vol. 17, No. 6, pp. 276–278, June 1996.
[14] Van Langevelde R., Klaassen F. M., "An explicit surface-potential-based MOSFET model for circuit simulation", Solid-State Electronics, Journal of, Vol. 44, No. 3, pp. 409–418, 2000.
[15] Ma Y. et al ,"Validity and applicability of triangular potential well approximation in modeling of MOS structure inversion and accumulation layer",Electron Devices, IEEE Transactions on, Vol. 47, No. 9, pp. 1764–1767, 2000.
[16] He J. et al, "BSIM 5: An advanced charge based MOSFET model for nanoscale VLSI circuit simulation", Solid-State Electronics, Journal of, Vol. 51, pp. 433–444, 2007.
[17] Holm R., "The electric tunnel effect across thin insulator films in contacts,' Appl. Physics , Journal of, pp. 569–574, May 1951.
[18] S. M. Sze, Physics of Semiconductor Devices, 2nd ed. New York: Wiley, 1981, pp. 520–521.
[19] Vogel E., "Modeled Tunnel Currents for High Dielectric Constant Dielectrics", Electron Devices, IEEE Transactions on, Vol. 45, No. 6, pp. 1350–1355, June, 1998.
[20] Lee W. C. and Hu C. M., "Modeling CMOS tunneling currents through ultrathin Gate oxide due to conduction- and valence-band electron and hole tunneling",Electron Devices, IEEE Transactions on, Vol. 48, No. 7, pp. 1366–1373, July 2001.

Instruction for Authors

Editorial objectives

In the review "Electronics", the scientific and professional works from different fields of electronics in the broadest sense are published. Main topics are electronics, automatics, telecommunications, computer techniques, power engineering, nuclear and medical electronics, analysis and synthesis of electronic circuits and systems, new technologies and materials in electronics etc. In addition to the scientific and professional works, we present new products, new books, B. Sc., M. Sc. and Ph.D. theses.

The main emphasis of papers should be on methods and new techniques, or the application of existing techniques in a novel way. Whilst papers with immediate application to particular engineering problems are welcome, so too are papers that form a basis for further development in the area of study.

The reviewing process

Each manuscript submitted is subjected to the following review procedures:

- It is reviewed by the editor for general suitability for this publication;

- If it is judged suitable two reviewers are selected and a double review process takes place;

- Based on the recommendations of the reviewers, the editor then decides whether the particular article should be accepted as it is, revised or rejected.

Submissions Process

The manuscripts are to be delivered to the editor of the review by the e-mail: electronics@etfbl.net.
Upon the manuscript is accepted for publication, the author receives detailed instructions for preparing the work for printing.
Authors should note that proofs are not supplied prior to publication and ensure that the paper submitted is complete and in its final form.

Copyright

Articles submitted to the journal should be original contributions and should not be under consideration for any other publication at the same time. Authors submitting articles for publication warrant that the work is not an infringement of any existing copyright and will indemnify the publisher against any breach of such warranty. For ease of dissemination and to ensure proper policing of use, papers and contributions become the legal copyright of the publisher unless otherwise agreed.

ELECTRONICS, VOL. 14, NO. 2, DECEMBER 2010